Surface Passivation for Silicon Solar Cells using Stable Extrinsic Field Effect Passivation

by

Katherine Collett

Thesis submitted for

Degree of Doctor of Philosophy

June 2018

Supervised by Professor Peter R Wilshaw, Dr Ruy Sebastian Bonilla and Professor Chris Grovenor

University of Oxford

Department of Materials

In the hope of mitigating Climate Change

ACKNOWLEDGMENTS

I wish to acknowledge, more formally, the support of the EPSRC who funded my doctorate, and Trinity College who have always been most generous; Ruy Sebastian Bonilla for his simulations, Matlab scripts and LabVIEW programmes; and Tasmiat Rahman at Southampton for his generous assistance with the e-beam evaporator.

Throughout this doctorate, I have been supported, encouraged and educated by so many. To all of you - thank you.

Firstly, I want to thank my supervisor, Peter Wilshaw – your enthusiasm, love of lively scientific discussions and imaginative thinking has been inspiring. Thank you for investing so much in your students; because of this I have learnt and developed a great deal over the course of my doctorate. I feel extremely fortunate to have had you as my supervisor. Secondly, Sebastian – what would I do without you? You have been the most incredible mentor and friend. I am grateful for you answering too many of my questions to begin with, and I am grateful for when you stopped and made me stand on my own two feet. Your intellect and kind spirit are things I will always aspire to. And thirdly Phillip, I doubt I will ever again share an office with two people who are the highlight of my week. Thank you for somehow always finding the time to discuss scientific dilemmas, for helping me get less overwhelmed and for bringing laughter into the lab, every day, through your humour and sardonic wit. And of course, thank you to Professor Chris Grovenor for keeping a watchful eye on me and for your presentation advice that resulted in me rather unexpectedly winning the Hetherington Prize.

Thank you to Gaby for always being there, even going over my slides at a house party, to Eli for your reliable company in the lab and delicious baking, and to David for your enthusiasm about science and supply of funny stories. Thank you to the parts IIs I have worked with: Lucy, Richard, Matt, Nick, Marcus, Shawn, Angela, Louis and Hantao; for your hard work and good company. I wish to say a special thank you to Radka, who constantly goes above and beyond.

Outside of the Department, I want to thank Marion Frostick, who has taught me the art of short sentences. My writing has been transformed thanks to your guidance and patience.

And of course, my family. Peter, Jill and Clemi; your constant love, belief and support has empowered me, not just over the last four years, but for my entire life. I would not have got to where I am without you.

There are many friends who deserve to be mentioned here. I am so fortunate to know you all, you have encouraged me throughout, and tolerated my absences due to work. However, the list would be too long to include here, and so instead I shall thank you all in person. With the exception of Asbjørn - thank you for waiting for me!

ABSTRACT

SURFACE PASSIVATION FOR SILICON SOLAR CELLS USING STABLE EXTRINSIC FIELD EFFECT PASSIVATION

Katherine A. Collett
Trinity College
Thesis submitted for Degree of Doctor of Philosophy
Trinity Term, 2018

One of the largest challenges for high efficiency solar panels is the recombination of photo-generated carriers at the silicon surface. This recombination can be reduced by both chemical passivation and Field Effect Passivation (FEP). Conventionally, this is achieved by the SiN_x antireflection coating. However, this is sub-optimal and insufficient for high efficiency devices. This thesis focuses on introducing FEP, independent of the antireflection coating, to allow superior surface passivation to be achieved.

The alneal, a process of annealing aluminium covered oxide layers, is known to provide excellent surface passivation, was investigated. This already superior surface passivation method could be improved with the addition of sodium and potassium ions at the SiO_2-Si interface, termed ionic-FEP. This produced record-breaking surface passivation with a surface recombination velocity (SRV) of 0.15 cm/s and a surface saturation current denisty (J_{0s}) of 0.1 fA/cm^2 on 1 Ωcm n-type float zone (FZ) Si. A mechanism is described that explains ion introduction during this process. It offers an explanation as to why the passivation is achieved so rapidly, requiring an anneal of under 15 seconds at 450 °C, and places emphasis on the importance of an electric field between the oxide surface and silicon substrate during ion introduction. The requirement for an electric field for fast ionic migration is utilised in developing an industrially scalable technique for introducing ionic-FEP.

Ionic precursors are deposited onto the SiO_2 surface by spin or spray coating. The migration process comprises two stages: corona charge deposition to provide the electric field for migration and an anneal at 450 °C. Using potassium, there was found to be a linear, almost one-to-one, relationship between corona surface charge and resulting interface charge after annealing. The anneal time required for potassium ion introduction at 450 °C was found to be under two seconds. This process achieved a SRV of 3.3 cm/s, equivalent to a J_{0s} of 8.4 fA/cm^2 on 1 Ωcm n-type FZ Si.

The addition of hydrogen to an ionically-passivated SiO_2-Si interface was tested. It was found that hydrogen was able to increase the effective lifetime of 200 μm thick 1 Ωcm n-type FZ Si from 1800 μs to 3000 μs. As the interface charge concentration for this experiment was not optimal, it is likely that with the right charge concentration this process could provide surface passivation of a similar quality as the ion-enhanced alneal.

Alternative ionic species for FEP were trialled. Larger ions were tested following the hypothesis that they may be more strongly bound to the SiO_2-Si interface. Rubidium was successfully introduced, although the process required minutes rather than seconds. An effective lifetime of 1800 μs was achieved, which is comparable to that realised using potassium at the same concentration. Calcium showed promise, but the successful introduction of the species could not be concluded. Magnesium and Strontium seem unable to be introduced into the SiO_2-Si system as charged species.

TABLE OF CONTENTS

Table of Contents iv
Preface vii
List of Figures viii
List of Tables xiii
1 Introduction 1
1.1 Climate Change and Renewable Energy 1
1.2 Silicon Photovoltaics 6
1.2.1 Fundamental Principles 6
1.2.2 Types of Recombination 8
1.3 Cell Geometries 9
1.4 Silicon Surface Passivation 13
1.4.1 Chemical Passivation 14
1.4.2 Field Effect Passivation 19
1.5 Methods of Extrinsic Field Effect Passivation 23
1.5.1 Corona Discharge 23
1.5.2 Ionic Charge 24
1.6 Alneal 25
1.7 Best Surface Passivation At time of Writing 25
1.8 Aim of this work 27
1.9 Structure of this thesis 27
2 Background Literature on Recombination and Surface Passivation 29
2.1 Recombination Theory 29
2.2 Bulk Recombination 31
2.2.1 Radiative Recombination 32
2.2.2 Auger Recombination 33
2.2.3 Defect Mediated Recombination 34
2.2.4 Limiting Recombination Mechanism 35
2.3 Surface Recombination 37
2.3.1 Space Charge Region 38
2.3.2 Effective Surface Recombination Velocity 39
2.4 Calculation of Effective SRV 39
2.5 Surface Saturation Current Density 41
2.6 Interface Trap Theory 41
2.7 Field Effect Passivation Theory 44
3 Experimental Methods 46
3.1 Base Silicon 46
3.1.1 Substrates 46
3.1.2 Surface Finish 47
3.2 Dielectrics 47
3.2.1 Thermal Oxides Growth 47
3.2.2 Optical Characterisation 48
3.3 Metal Deposition 48
3.3.1 Thermal Evaporation of metal 49
3.3.2 E-beam Evaporation of metal 49
3.4 The Alneal 50
3.5 Corona Discharge 51
3.6 Ion Deposition 52
3.6.1 Thermal Evaporation of Salts 52
3.6.2 Spin Coating 53
3.6.3 Spray Pyrolysis 54
3.7 Ion Migration Processes 54
3.7.1 Annealing 54

3.7.2 Thermally Stimulated Ionic Conduction ... 55
3.7.3 Field-Assisted Ionic Migration ... 57
3.8 Characterisation Techniques ... 58
3.8.1 Photoconductance Decay Lifetime ... 58
3.8.2 Capacitance-Voltage ... 58
3.8.3 Kelvin Probe ... 64
3.8.4 SIMS ... 67
3.8.5 Density of Interface Traps ... 68
4 Enhancing Alneal Passivation ... 73
4.1 Lifetimes Achieved Using the Alneal ... 73
4.2 The Alneal Process – Background ... 76
4.3 Comparison Between Experimental and Modelled Lifetimes ... 79
4.4 Field Effect Passivation and the Alneal Process ... 81
4.4.1 Dielectric Charge in Enhanced and Standard Alneal ... 81
4.4.2 Additional Charge from Corona Discharge ... 84
4.5 Details of Charge in the Enhanced Alneal ... 88
4.5.1 Identifying Charged Species ... 89
4.6 Source of Charge ... 94
4.7 Conclusions ... 95
5 Ion Introduction During Enhanced Alneal ... 96
5.1 Ion Introduction ... 96
5.2 The Effect of Different Sample Structures ... 100
5.2.1 Use of Mask During Al Deposition ... 102
5.2.2 Al Etchant or Type of Probe ... 103
5.2.3 The Impact of Differing Aluminium Coverage of the Oxide During the Anneal ... 105
5.3 Model for Ionic Migration ... 107
5.3.1 No Electrical Connection Between the Aluminium and Silicon ... 107
5.3.2 With an Electrical Connection Between the Aluminium and Silicon ... 109
5.4 Using Gold Instead of Aluminium ... 111
5.4.1 Anneal using Gold and Aluminium ... 111
5.4.2 TSIC using Gold and Aluminium ... 113
5.5 TSIC with varied Temperature and Bias ... 114
5.6 Conclusions ... 116
6 Towards Industrial Ion Introduction ... 117
6.1 Literature Review of Introduction of Ions to Silicon Dioxide ... 118
6.2 Development of an Industrially Compatible Technique ... 121
6.2.1 Ionic Precursor Deposition ... 122
6.3 Field-Assisted Migration ... 130
6.3.1 Dependence of Interface Charge on Initial Surface Corona Charge ... 130
6.3.2 Anneal Temperature and Time ... 133
6.4 SIMS Evidence for Potassium Introduction ... 137
6.5 Conclusions ... 139
7 Optimising Ion-Induced FEP ... 141
7.1 Supplementing Ionic FEP with Hydrogen ... 141
7.2 Preliminary Investigation of Different Ionic Species ... 146
7.2.1 Rubidium ... 150
7.2.2 Magnesium ... 154
7.2.3 Calcium ... 159
7.2.4 Strontium ... 161
7.2.5 Surface Corona Charge Decay Time at Elevated Temperatures ... 162
7.3 Conclusions ... 163
8 Summary and Further Work ... 165
8.1 Alneal Passivation: Standard and Enhanced ... 166
8.2 Migration Mechanism of Ions for FEP During the Enhanced Alneal ... 168
8.3 Developing an Industrial Ion Migration Process ... 169

8.4 Improving Ionic FEP with Hydrogen 170
8.5 Ionic FEP with Different Ions to Improve Stability 171
8.6 Further Work & Towards Industrialisation........ 172
References 175
Appendix 186
Oxide surface 186
RCA Clean of Oxide Surface........ 186
E-Beam Evaporation of Aluminium........ 187
Furnace 188
Thermal Evaporator........ 189
High Vacuum vs Low Vacuum........ 189
Bare Tungsten Coil........ 190
High purity Al 192
Clean Thermal Evaporator Components........ 192

PREFACE

This thesis is an account of the work I have carried out as a postgraduate student at the Department of Materials, University of Oxford. I have not submitted any part of this thesis for a degree at this University or elsewhere. The work of other authors is duly acknowledged in the text and appropriate references are given.

Katherine A. Collett

Below is a list of publications that I have contributed towards during my time studying for this degree:

Collett, K. A., Du, S., Bourret-Sicotte, G., Hamer, P., Hallam, B., Bonilla, R.S., and Wilshaw, P.R. 2018. Scalable Techniques for Tailoring Field Effect Passivation in High Efficiency Silicon Solar Cells, *IEEE Journal of Photovoltaics* 2156-3381, p. 1-8

Hamer, P., Chan, C., Bonilla, R.S., Hallam, B., Bourret-Sicotte, B., **Collett, K.A**., Wenham, S. and Wilshaw, P.R. 2018. Hydrogen Induced Contact Resistance in PERC Solar Cells. *Solar Energy Materials and Solar Cells,* 184, p. 91-97

Collett, K. A., Bonilla, R.S., Hamer, P., Bourret-Sicotte, G., Lobo, R., Kho, T., and Wilshaw, P.R. 2017. An enhanced alneal process to produce SRV <1cm/s in 1Ωcm n-type Si, *Solar Energy Materials and Solar Cells*, 173, p.50-58

Bourret-Sicotte, G., Hamer, P., Bonilla, R.S., **Collett, K. A**., Wilshaw, P.R. 2017. Shielded Hydrogen Passivation – a novel method for introducing hydrogen into silicon. *Energy Procedia*, 124, p. 267-274

Bourret-Sicotte, G., Hamer, P., Bonilla, R.S., **Collett, K**., Ciesla, A., Colwell, J., and Wilshaw, P.R. 2017. Shielded hydrogen passivation – a potential in-line passivation process. *Physica Status Solidi (a)*, 214 (7)

Shaw, E.C., Hamer, P, **Collett, K. A**., Bourret-Sicotte, G., Bonilla, R.S., and Wilshaw, P.R., 2017. Saw Damage Gettering for Industrially Relevant mc-Si Feedstock. *Physica Status Solidi (a),* 214 (7)

Collett, K. A., Cyrson, M., Bonilla, R. S., and Wilshaw, P.R., 2016, Surface Passivation Provided by an Alneal through SiO2/TiO2 Bilayer, *Proceedings of the 32nd European Photovoltaic Solar Energy Conference and Exhibition*, available online: http://www.eupvsec-proceedings.com/

Bonilla, R. S., Jennison, N., Clayton-Warwick, D., **Collett, K. A**., Rands, L., and Wilshaw, P.R., 2016. Corona charge in SiO2: kinetics and surface passivation for high efficiency silicon solar cells. *Energy Proceedia*, 92, p 326 - 335

Bonilla, R. S., **Collett, K**., Rands, L., Martins, G., Lobo, R., & Wilshaw, P. R., 2016, Stable, extrinsic, field effect passivation for back contact silicon solar cells. *Solid State Phenomena*, 242, p.67-72

LIST OF FIGURES

Figure 1. Global levelised cost of electricity from utility-scale renewable power generation technologies, 2010-2017. After [5] © IRENA 2018 2

Figure 2. Global Cumulative Installed PV Capacity. After Fraunhofer ISE [6]. ©Fraunhofer ISE: Photovoltaics Report, updated: 12 July 2017 3

Figure 3. Global cumulative installed capacity by energy source in 2016 and predicted for 2040. Printed with permissions from Bloomberg New Energy Finance [10] 4

Figure 4. (a) breakdown of balance of system costs by country in 2015 in USD/kW and (b) global PV module prices in USD/W. Note the difference in cost scales. © IRENA 2016 [11]. 5

Figure 5. Schematic of energy against depth to show the p-n junction band structure and photoelectric effect. EC is the conduction band. EF is the fermi level. EV is the valence band. Filled circles are electrons and hollow circles are holes. The zig-zag black arrow represents an incoming photon. 7

Figure 6. Types of recombination Radiative, Auger and Defect-assisted via a trap level at energy E_t. Hollow circles represent holes. Filled circles represent electrons. Arrows indicate direction of electron transition. After [14] 8

Figure 7. Schematic of a conventional p-type Al-BSF silicon solar cell. Hollow circles represent holes. Filled circles represent electrons. 10

Figure 8. Schematic of an interdigitated back contact (IBC) silicon solar cell. Hollow circles are holes. Filled circles are electrons. 11

Figure 9. Schematic showing the effect on bandgap states (red lines) and silicon energy bands of a) a bare silicon surface, b) a chemically passivating dielectric layer and c) a chemically passivating dielectric layer with the addition of field effect passivation. 14

Figure 10. Energy band diagram for silicon showing the offset between the conduction and valence band in momentum-space that results in the requirement for a change in momentum. After [69]. . 32

Figure 11. Energy dependent density of interface traps, typical of a thermally grown SiO_2-Si interface of 100 orientation. After [46] 42

Figure 12. Energy dependent electron and hole capture cross-sections at the Si-SiO_2 interface. The solid lines represent guides to the eye. After [46]. 43

Figure 13 Surface recombination velocity for n-type silicon as a function of positive and negative dielectric fixed charge concentration in q/cm^2, for an excess minority carrier concentration of 10^{15} cm^{-3}, and a variation in the surface recombination of holes and electrons given by the curvatures $\boldsymbol{an}$ and $\boldsymbol{ap}$. Four combinations of $\boldsymbol{an}$, $\boldsymbol{ap}$ have been chosen as illustrated by the legend in the figure. Inset: Holes (green) and electrons (black) surface recombination functions used to calculate surface recombination velocity. Red horizontal lines represent the value the functions take when the dependence is eliminated ($\boldsymbol{an/p}$= 0). After [98]. 45

Figure 14. Corona Discharge apparatus. After [98]. 51

Figure 15 Thermally Stimulated Ionic Conduction (TSIC) (a) schematic and (b) typically measured parameters during processing. After [108]. 56

Figure 16 Schematic of Hg-CV probe. After [98]. 59

Figure 17 Schematic to demonstrate (a) equivalent circuit used in CV measurement analysis and (b) a representation of a CV curve showing ideal conditions (red), deep depletion (orange), including interface charge (green) and with interface states (blue). After [98]. 59

Figure 18. (a) Schematic of the CV set up, (b) band diagram for flatband conditions assuming all charge located at the SiO_2-Si interface. 61

Figure 19. (a) Schematic of the Kelvin probe set up and (b) typical band diagram, with all charge located at the SiO_2 surface 64

Figure 20. Equivalent circuit for conductance measurements (a) MOS structure, (b) simplified version of (a), (c) measured circuit and (d) including series resistance and tunnel conductance. After [112]. 70

Figure 21. G_P/ω against ω for a single level, a continuum and experiments data. For all curves D_{it} = 1.9×10^9 $eV^{-1}cm^{-2}$, $\tau_{it} = 7 \times 10^{-5}$ s. After [112]. 71

Figure 22. Injection level dependent lifetimes of enhanced alneal, standard alneal and as-oxidised samples. The numbers associated with the standard and enhanced alneal samples are for sample identification. 75

Figure 23. Simulated injection level dependent effective lifetimes showing D_{it} mid-gap values for an alnealed interface (typical, 10^{10} to 10^{11} $eV^{-1}cm^{-2}$, and extreme, 10^9 $eV^{-1}cm^{-2}$) [5], [10], [14], [36] and dielectric film charge $\boldsymbol{Qf}$ for an as-grown thermal silicon dioxide (typical, 10^9 to 10^{10} q/cm^2, and extreme, 10^{11} q/cm^2) [17]. Experimental data from enhanced and standard alneal samples superimposed. 80

Figure 24. Injection dependent effective lifetimes for (a) standard alneal 1 and (b) enhanced alneal 1 both with the addition of positive corona charge to the oxide surface, with the total surface charge reported as $Q_{surface}$. 86

Figure 25. Injection dependent effective lifetimes for enhanced alneal 1 with the addition of positive corona charge to the oxide surface and Richter intrinsic lifetime limit. 88

Figure 26. TSIC data for an Al front contact deposited in the same thermal evaporator and the Al for the enhanced alneal with sub plots of current and charge, voltage, and temperature, all against time. The maximum temperature is held for a given time to ensure all the available ions have the opportunity to migrate. 90

Figure 27. SIMS results of (a) a sample with an Al front contact deposited in the same thermal evaporator as Al for the enhanced alneal, which has undergone TSIC with the temperature ramping to 300 ˚C with a 5 V bias applied and (b) Enhanced Alneal 1. SiO_2 on the left and Si on the right of the marked interface. 92

Figure 28. Interface charge concentration after an aluminium anneal at 400 ˚C. Al deposition in contaminated thermal evaporator. 97

Figure 29. Schematic energy diagram of energy against distance into the sample (from the aluminium top contact, left, to the silicon, right) for a positive ion in an electrically isolated Al-SiO_2-Si structure. 98

Figure 30. Interface charge after annealing with either the oxide fully covered in Al or an Al dot in the centre of the oxide. Al depositions made in the contaminated thermal evaporator. 101

Figure 31. Interface charge measurement before and after the following processing: Full Al evaporation in contaminated thermal evaporator. MOS structure formed using Al etchant and lacomit to protect an area of the Al. This structure was then annealed at 400 °C for 5 minutes. After the anneal, the back oxide was removed with HF and a back contact was formed using InGa and silver dag. CV measurement was taken using the probe station and Al dot on the top surface. 102

Figure 32. Interface charge before and after the following processing: Full Al deposition using contaminated thermal evaporator. Annealed at 400 °C for 5 minutes. After annealing, an MOS structure was fabricated using a diamond scribe to form an isolated dot in the top metal. Back oxide was removed with HF and contacted using InGa and silver dag. CV measurement was taken using the probe station and Al dot on the top surface. 104

Figure 33. Interface charge against anneal time at 400 ˚C on hotplate. The anneals were conducted with the oxide surface either fully covered in aluminium (blue), or a 2 mm diameter aluminium dot in the centre of the oxide (orange). Error bars are shown as calculated in [113]. For comparison, a

sample with an Al dot that underwent TSIC with a 0V bias at 400 ˚C is included. Al deposited in contaminated thermal evaporator. 106

Figure 34. (a) Energy band diagram for a positive ion in a system of electrically isolated Al on top of SiO_2 and (b) schematic of charge location within an electrically isolated Al SiO_2-Si structure. 108

Figure 35. (a) Energy band diagram for a positive ion in this system of Al electrically connected to n-type 1 Ωcm Si and (b) schematic of electrically contacted Al-SiO_2-Si structure. 110

Figure 36. Interface charge concentration for anneals of 30 seconds and 5 minutes at 400 °C on samples with KCl deposited on the oxide surface using either aluminium (blue) or gold (orange) during the anneal. Aluminium deposited to cover the full surface, and edge of the silicon sample. 112

Figure 37. Concentration of migrated charge, calculated by integration of TSIC current, against voltage applied to top contact during TSIC for samples deposited with KCl salts, using aluminium or gold contacts. The error in the measurement of charge is of the order of 10^{12} q/cm^2 [109]. Lines are a guide to the eye. 113

Figure 38. Interface charge from CV measurements after TSIC under various gate biases with the temperature ramping to 200 °C or 400 °C. Samples were held at this temperature for 25 minutes before they were cooled with the voltage still applied. Al dot deposited in contaminated thermal evaporator, all samples were deposited with Al in one batch. The average initial interface charge concentration is given by the grey horizontal line. Material used was 1 Ωcm n-type FZ Si with a 100 nm thermal oxide. 115

Figure 39. Concentration of (a) sodium and (b) potassium ions migrated to the oxide-silicon interface as a function of anneal time for a range of temperatures. After [61]. 119

Figure 40. Experimental process flow chart 121

Figure 41. Effective lifetimes before and after field-assisted ionic migration with thermally deposited KCl as a function of interface charge concentration. Effective lifetime after field-assisted ion migration, with the addition of surface corona charge for maximum FEP. The horizontal line represents the effective lifetime of an as-received sample with surface corona charge for maximum FEP. FZ n-type Si, 1 Ωcm, 200 µm, 100 nm thermal oxide. The migration anneal was performed at 450 ˚C for 1 minute. 124

Figure 42. Effective lifetimes before and after field-assisted ionic migration with spin coated KCl as a function of interface charge concentration. Effective lifetime after field-assisted ion migration, with the addition of surface corona charge for maximum FEP. The horizontal line represents the effective lifetime of an as-received sample with surface corona charge for maximum FEP. FZ n-type Si, 1 Ωcm, 200 µm, 100 nm thermal oxide. The migration anneal was performed at 450 ˚C for 1 minute. 125

Figure 43. Effective lifetimes before and after field-assisted ionic migration with spray coated KCl. Effective lifetime after field-assisted ion migration, with the addition of surface corona charge for maximum FEP. The horizontal line represents the effective lifetime of an as-received sample with surface corona charge for maximum FEP. FZ n-type Si, 1 Ωcm, 200 µm, 100 nm thermal oxide. The migration anneal was performed at 450 ˚C for 1 minute. 127

Figure 44. Box plots to show statistical data for interface charge concentration. All three deposition techniques shown. Five different average interface charge concentrations are displayed for thermal evaporation and spin coating to show the statistical distribution using different field-assisted ionic migration parameters, resulting in differing average interface charge concentrations. The interface charge concentrations are measured across both surfaces of 3 x 3 cm^2 samples. Lines of the box represent the median, lower and upper quartile values, indicates the mean and x marks the minimum and maximum values. 129

Figure 45. Schematic of sample structure and energy diagram for a positive ion (a) after ionic precursor deposition, (b) after corona charge deposition and (c) after ion migration. 131

Figure 46. Interface charge concentration dependence on surface corona charge concentration before migration anneal. Shown for various precursor depositions using both thermal evaporation and spin coating techniques.. 132

Figure 47. (a) Effective lifetimes and (b) interface charge after corona-induced field-assisted ionic migration of thermally evaporated potassium precursor using a surface charge of 1.9 x 10^{12} q/cm^2 with varying anneal temperature for various anneal times. Effective lifetimes shown are with no residual surface corona charge. Error bars show ±3σ of interface charge uniformity, taken from results shown in Figure 44... 135

Figure 48. SIMS results showing concentration of potassium and sodium against distance into SiO_2 dielectric after field assisted ionic migration using a surface corona charge concentration of 1.8 x 10^{12} q/cm^2 at 450 °C for anneal lengths of (a) 2 seconds and (b) 60 seconds.............................. 138

Figure 49. Shielded hydrogen passivation followed by ionic FEP showing (a) the effective lifetimes at an injection level of 10^{15} cm^{-3} after each processing step along with the final interface charge concentration and (b) the injection dependent effective lifetime curves after each step. 143

Figure 50. Ionic FEP introduction followed by shielded hydrogen passivation showing (a) the effective lifetimes at an injection level of 10^{15} cm^{-3} after each processing step along with the final interface charge concentration and (b) the injection dependent effective lifetime curves after each step. 145

Figure 51. Interface charge concentration of (a) Na and (b) K introduced by TSIC followed by exposure to a reverse bias of -10 V at a temperature of 100 °C for various lengths of time. 147

Figure 52. Interface charge concnetration after spin coating with RbCl and field-assisted migartion at 450 °C for 4 minutes, using different concnetrations of surface corona charge before migration anneal. 151

Figure 53. Injection dependent effective lifetime curves for samples deposited with (a) Rb and (b) K precursor and treated with field-assisted ionic migration to result in an interface charge concentration of 1.5 x 10^{12} q/cm^2. 152

Figure 54. Resulting interface charge concnetration (left) and remaining surface charge concentration (right) for samples spin coated with RbCl and treated with field-assisted ionic migration at 500 °C, for different lengths of time, using an initial surface charge of 2 x 10^{12} q/cm^2. 153

Figure 55. Injection dependent effective lifetime curves for (a) an as-received sample and with the addition of corona charge, (b) an Al alneal sample before and after processing and with the addition of corona charge for maximum FEP and (c) an AlMg alneal sample before and after processing and with the addition of corona charge for maximum FEP. Surface charge concentrations Q_{KP} and interface charge concentrations Q_{CV} given. Sample size: 3 x 3 cm^2. 155

Figure 56. Interface charge concentrations for field-assisted ionic migration of MgCl spin coated samples deposited with varying concentrations of surface corona charge before annealing at a temperature of (a) 450 °C for 1 minute or (b) 500 °C for 4 minutes.. 157

Figure 57. Capacitance-voltage curves for samples spin-coated with MgCl and treated with field-assisted ionic migration at 450 °C or 500 °C using several surface charge concentrations and an anneal of 1 or 4 minutes. 158

Figure 58. Interface charge concnetration for field-assisted ionic migration of CaCl spin coated samples deposited with varying concentrations of surface corona charge before annealing for 6 minutes at a temperature of (a) 450 °C or (b) 500 °C. 160

Figure 59. Interface charge concnetration after field-assisted ionic migration of SrCl spin coated samples deposited with varying concentrations of surface corona charge before annealing for 7 minutes at a temperature of (a) 450 °C or (b) 500 °C. 162

Figure 60 Injection dependent effective lifetimes for alnealed samples with and without RCA oxide surface clean before aluminium deposition. 186

Figure 61 Interface charge before and after TSIC processing for e-beam and thermally evaporated aluminium front and back contact. Log y-axis. 187

Figure 62 Injection dependent effective lifetime curves before and after anneal in tube furnace for one hour at 400 °C with no aluminium present. 189

Figure 63 Interface charge concentrations of alnealed samples with aluminium thermally evaporated under different vacuum pressures. 190

Figure 64 Interface charge from CV data before and after TSIC processing for sample exposed to bare tungsten coil under high current with no Al. Thermally evaporated Au for front contact..... 191

Figure 65 Interface charge concentration after alnealing using 5n Al and 6n Al both thermally evaporated from a tungsten coil. 192

Figure 66 Interface charge concentration after TSIC processing of 5n Al thermally evaporated from a tungsten coil using new copper arms, cleaned chamber walls and new pyrex sample holder. ... 193

LIST OF TABLES

Table I. Summary of the best passivation achieved by several high-quality passivation dielectrics [66] 26

Table II Summary of silicon substrates used in this thesis 46

Table III Summary of silicon oxidation processing of samples used in this project 48

Table IV Details of various alneal processing 50

Table V. Alneal samples τ_{eff}, SRV, J_{0s}, D_{it} and $Q_{interface}$ 82

Table VI Species concentration from integrated TSIC current-time data and from integrated SIMS concentration data 93

Table VII Interface charge from CV and K and Na concentrations from SIMS for samples spin coated with K followed by field-assisted ionic migration for different anneal times 139

Table VIII Solubility of various salts in water at 20 °C and 1 atmosphere pressure [168] 149

Table IX Salt supplier and chemical specification, for details on contamination 149

CHAPTER 1
INTRODUCTION

1.1 CLIMATE CHANGE AND RENEWABLE ENERGY

In order to mitigate climate change, it is evident from the correlation of CO_2 emissions and the temperature of the planet that we must transform the way in which we harvest energy [1]. In 2015, over 81% of the world's energy was produced by fossil fuels [2]. Unless this changes, the global temperature is likely to overshoot the target maximum rise of 2 ˚C [3], which, according to the IPCC report [1], is likely to cause detrimental effects both environmentally and socially. To prevent this, renewable energy sources must supply double their share of the global power usage by 2030, increasing to meet at least 36% of global energy demand [4].

To achieve this goal, the cost of renewables must be at grid parity. Figure 1, from the International Renewable Energy Agency (IRENA) [5], shows the change in installation cost per kWh between 2010 and 2017 for renewable energies. It is evident from this that the majority of renewable energies are already financially competitive with fossil fuels and it is the solar industry that has made the most significant rate of progress in cost reduction.

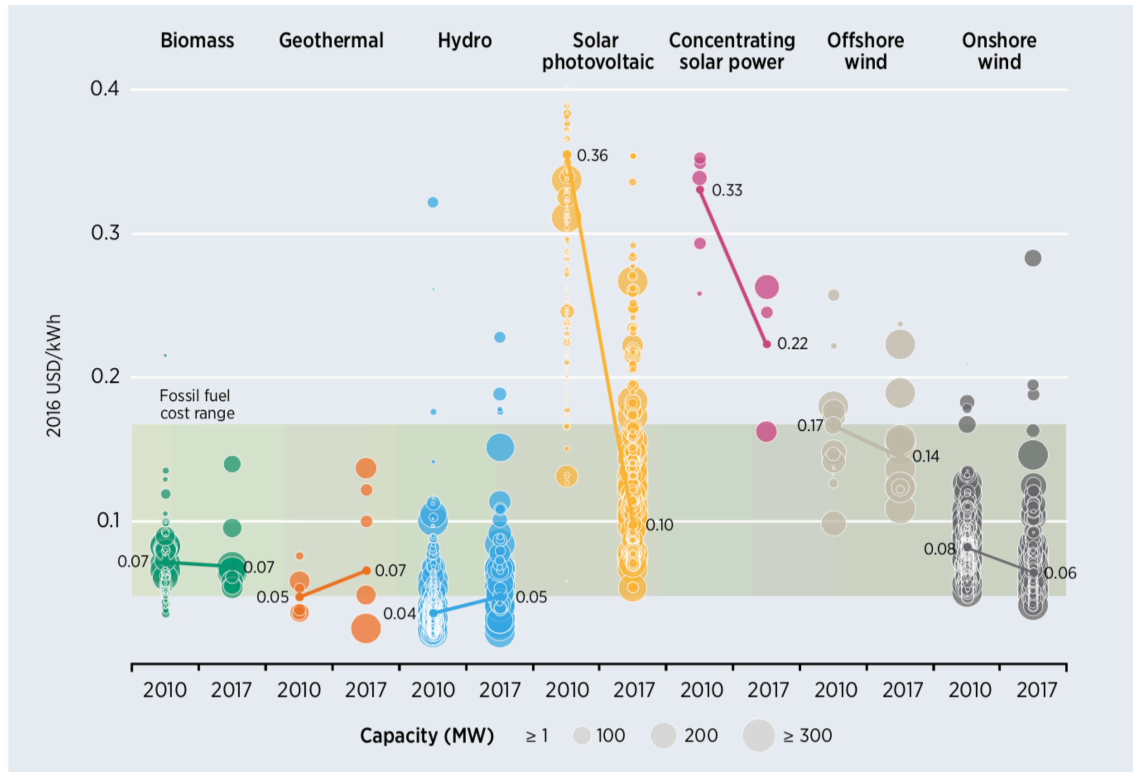

Figure 1. Global levelised cost of electricity from utility-scale renewable power generation technologies, 2010-2017. After [5] **© IRENA 2018**

Solar energy is a vast global resource which is currently under-exploited. Due to the size of the resource, solar photovoltaics (PV) have the potential to play a significant role in the energy mix. The installed capacity has been growing quickly over the last decade, as shown in Figure 2, with falling costs leading to an annual growth rate of 40% (2010 – 2016) [6]. This is faster than any other expected installed energy. In 2017, 98.9 GW of solar PV was installed globally [7], bringing the total global capacity to 397 GW [8]. For context, this is larger than the global nuclear capacity, which is 391.5 GW [9].

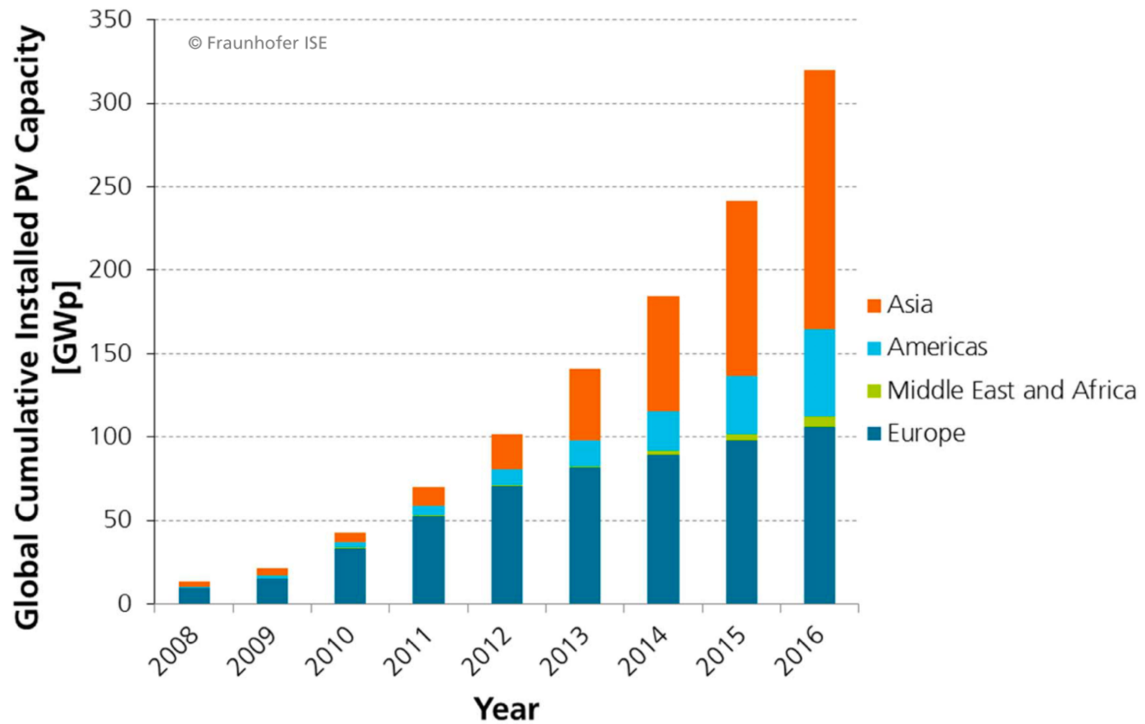

Figure 2. Global Cumulative Installed PV Capacity. After Fraunhofer ISE [6]. ©Fraunhofer ISE: Photovoltaics Report, updated: 12 July 2017

This growth in solar PV is expected to continue, with Bloomberg predicting that by 2040 solar PV will account for 32% of the global energy capacity [10].

Figure 3 shows the global cumulative installed capacity by energy source for 2016 and as predicted by Bloomberg for 2040. It is clear from these two figures that solar PV is excepted to fulfil a substantial proportion of the necessary future global renewable energy capacity. Within the solar PV industry, the majority of devices are made using silicon. In fact, in 2017, 94% of installed PV capacity was silicon based [6].

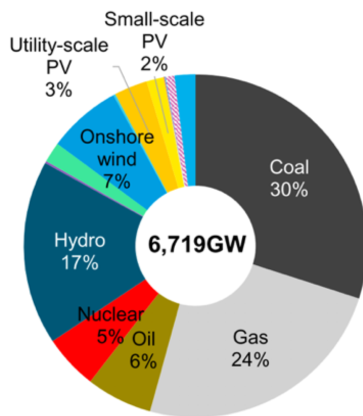

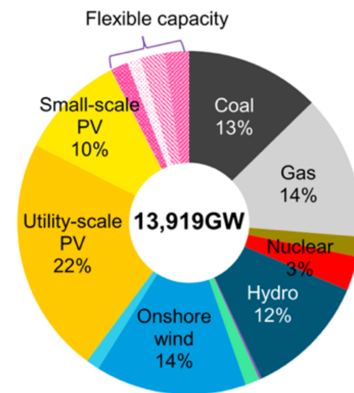

Figure 3. Global cumulative installed capacity by energy source in 2016 and predicted for 2040. Printed with permissions from Bloomberg New Energy Finance [10]

In order to meet the predictions of Bloomberg, it is fundamental that the cost per watt of installed solar PV capacity continues to decrease. For silicon PV, this can be effectively achieved by increasing the efficiency of the module rather than reducing the module cost. Naturally, high efficiency modules are of great value in regions where space is limited, for example built up urban areas. However, this is not limited to these areas. Due to the advances over the past decade, the cost of a module makes up between 25-40% of the overall cost of installation. The remaining proportion of the capital cost comes from the Balance of System (BOS) costs which consist of installation, inverters, mounting, land rental etc. By increasing the cell efficiency, it is possible to maintain the BOS costs, while increasing the capacity of the solar installation. Figure 4 shows the breakdown of BOS costs by country in 2015. For reference, the module cost per kW was equivalent to 600 – 700 USD [11] in Figure 4. Therefore, increasing cell efficiency is the focus of significant research efforts and considered vital in facilitating the continuing take-up of silicon PV.

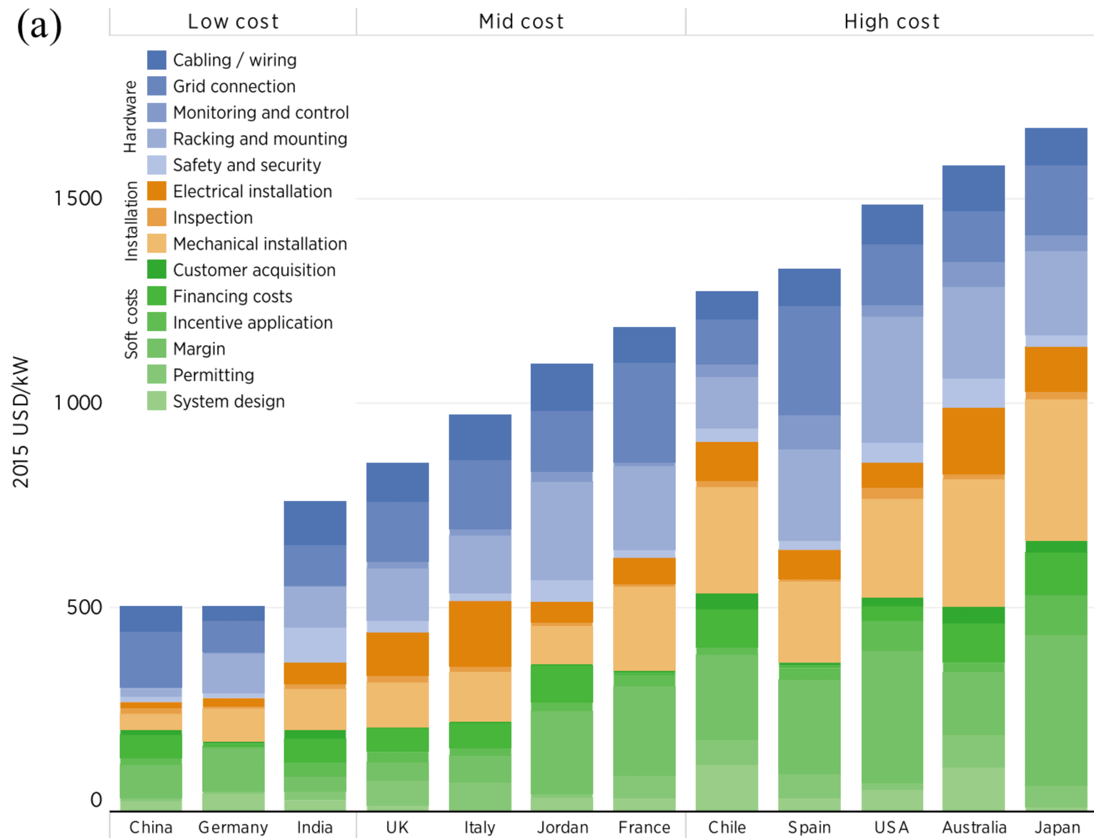

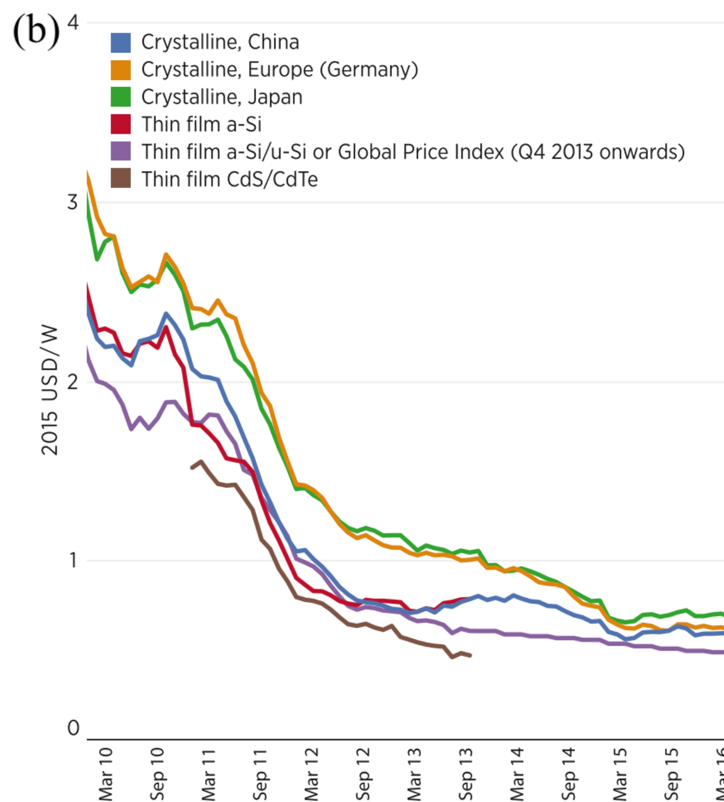

Figure 4. (a) breakdown of balance of system costs by country in 2015 in USD/kW and (b) global PV module prices in USD/W. Note the difference in cost scales. © IRENA 2016 [11]**.**

Silicon is expected to continue to dominate the PV market for the foreseeable future as the efficiency:cost ratio of silicon cells is far superior to that of other PV alternatives [12, 13]. Even with the trend towards tandem cells, that comprise two differing PV cells, silicon is the obvious candidate to fulfil the role of the base cell in the majority of the cases [12] and therefore the use of silicon cells will remain substantial. This makes silicon PV an important area of research.

1.2 Silicon Photovoltaics

Within the solar PV industry, silicon is the principal material used. The fundamentals of silicon photovoltaic energy conversion and the structures of silicon solar cells are discussed in this section.

1.2.1 Fundamental Principles

In a solar cell, photons are converted via the photoelectric effect into electrical energy that can be harnessed and used for an external load. This conversion is possible due to the semiconductor nature of silicon. Semiconductors contain a bandgap, a region of forbidden energies between the conduction and valence bands. When photons with greater energy than the bandgap interact with the silicon, they promote electrons from the valence to the conduction band. This leaves a hole in the valence band and hence the photon is said to create an electron-hole pair, as shown in Figure 5. As such, the bandgap energy dictates which photon energies in the solar spectrum can be absorbed. For silicon, photons over ~1.1 eV have sufficient energy to promote an electron from the valance to conduction band and can be absorbed.

In order for the electron-hole pair to produce useful energy, they must remain separate and be prevented from recombining until they can be harvested at the relevant metal contacts and used by an external load. To aid the extraction of the electron-hole pair, a p-n junction is used, shown in Figure 5. The minority carriers must cross the p-n junction to their corresponding sides to be collected, the electron to the n-type side and the hole to the p-type side. Once the generated minority carriers cross the p-n junction, they become majority carriers and their rate of recombination is limited by the concentration of minority carriers on that side of the p-n junction. Recombination is the unwanted loss of energy when charge carriers interact, and the conduction band electron is demoted to the valence band.

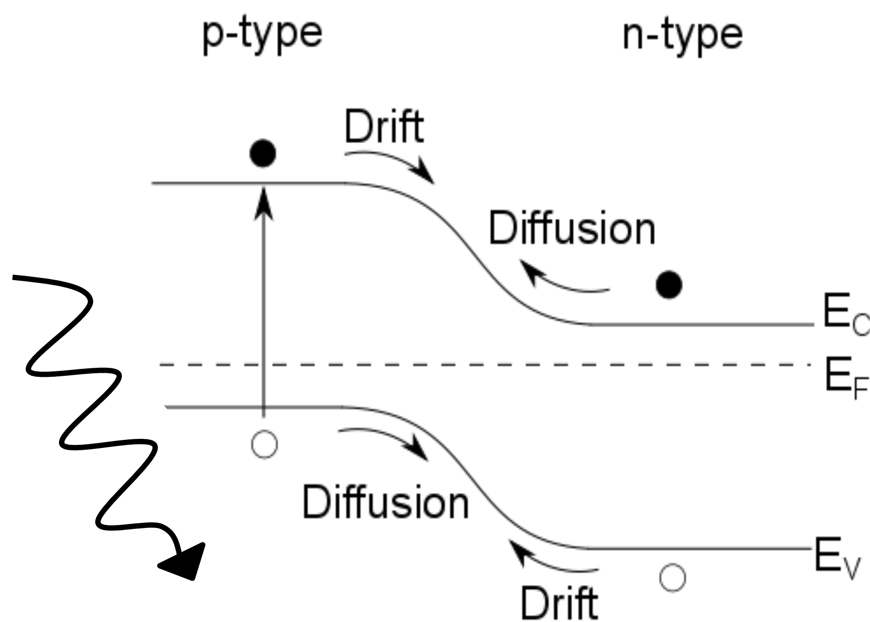

Figure 5. Schematic of energy against depth to show the p-n junction band structure and photoelectric effect. EC is the conduction band. EF is the fermi level. EV is the valence band. Filled circles are electrons and hollow circles are holes. The zig-zag black arrow represents an incoming photon.

Recombination can occur by three mechanisms. These will now be summarised, and a full explanation will follow in Chapter 2.

1.2.2 TYPES OF RECOMBINATION

There are three recombination mechanisms. Radiative recombination, Auger recombination and defect-assisted (or defect mediated) recombination, which is described by Shockley-Reed-Hall (SRH) statistics. The three types of recombination are shown in Figure 6.

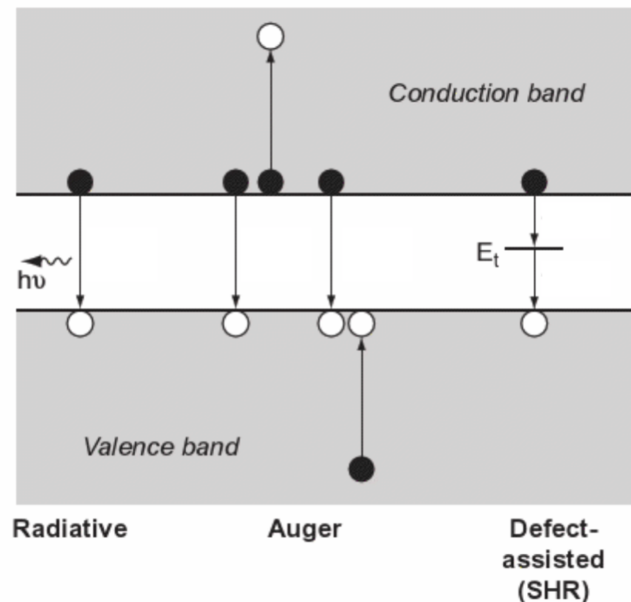

Figure 6. Types of recombination Radiative, Auger and Defect-assisted via a trap level at energy E_t. Hollow circles represent holes. Filled circles represent electrons. Arrows indicate direction of electron transition. After [14]

Radiative recombination is the reverse of electron-hole pair generation. It involves two carriers and the emission of a photon. However, because silicon is an indirect bandgap material, for an electron to move between bands a change in momentum is necessary. This means that radiative recombination is not as common in silicon as it is in direct bandgap materials.

Auger recombination requires three charge carriers. Energy and momentum is exchanged between them in one of the two ways depicted in Figure 6. This results in the demotion of an electron from the conduction to valence band.

Defect-assisted recombination exploits the existence of trap levels in the energy bandgap. These traps facilitate the transition of the electron from the conduction to the valence band as they allow for an exchange of momentum, and, as such, these trap levels are also referred to as recombination centres. Each recombination centre has electron and hole capture cross-sections associated with it. If the respective charge carriers enter this cross-section, it is assumed that they are trapped by the recombination centre. Once both type of charge carrier has entered this region, defect-mediated recombination can occur. The capture cross-section varies with recombination centre and carrier type.

1.3 CELL GEOMETRIES

The conventional silicon solar cell geometry is the Aluminium Back Surface Field (Al-BSF) design shown in Figure 7. It consists of p-type silicon, which makes up the bulk, along with a thin (< 1 μm) top layer of n-type Si which is the emitter [15]. The majority of photons are absorbed within the first few tens of μm of silicon [16]. The minority carriers must then travel to the p-n junction, and the majority carriers to the contact. In this cell design, the p-n junction is close to the region where the electron hole pairs are generated, therefore, the minority carriers do not have to travel far. The top surface is covered in an antireflection coating, to encourage photon absorption. Silver paste is then screen printed and fired to allow the paste to etch through the anti-reflection coating and contact the silicon substrate. The back surface of the cell is fully metal contacted. To ensure a good contact, after the aluminium is deposited on the back surface, the cell is fired at 800 °C, the eutectic point of Al-Si. On cooling, this creates a region at the back surface of effectively aluminium doped silicon. This ohmic contact allows for hole collection but also creates an internal field that

deters electrons from entering this region. However, it also produces an extremely recombination active region.

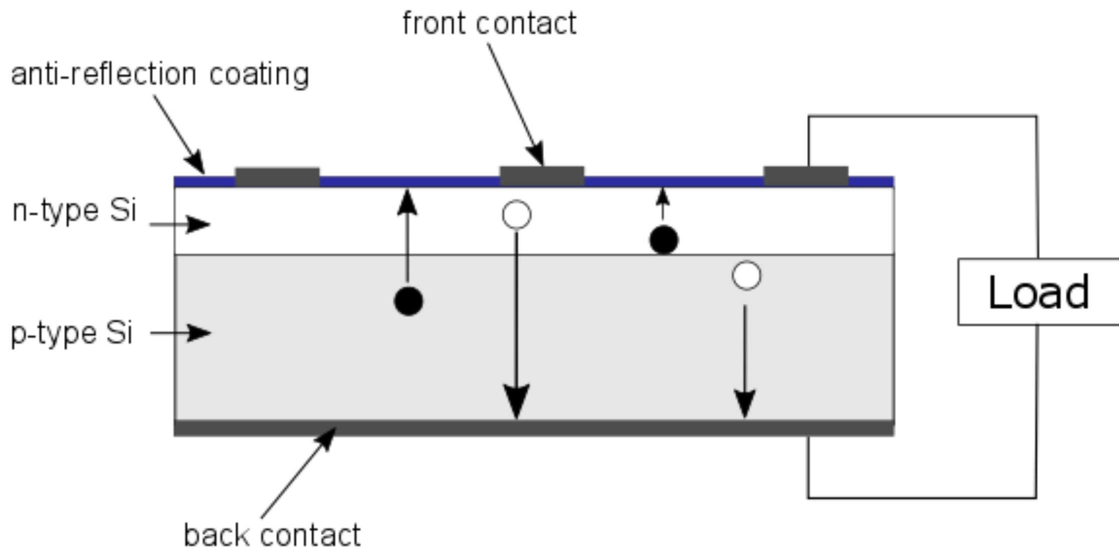

Figure 7. Schematic of a conventional p-type Al-BSF silicon solar cell. Hollow circles represent holes. Filled circles represent electrons.

There are several aspects of Al-BSF cells which can be modified to improve efficiency. Firstly, it is known that carrier recombination is more likely in p-type silicon than n-type silicon [17], discussed in Chapter 2. Secondly, the aluminium contact that covers the whole back silicon surface is an area of high carrier recombination due to a high concentration of defects. Thirdly, the design does not make the most of the irradiated top surface area due to the set of metal contacts on the front of the cell which shadow part of the incoming light. This means that less of the front surface can absorb photons. A solution to this final problem is to move the front contacts to join the contact already on the back, thereby leaving the front surface clear for photon absorption [18]. This is called a back-contact, back-junction cell. By reducing the area that the contacts cover, and by switching the bulk material to n-type, the first two problems can also be tackled. One configuration of the back-contact cell is an interdigitated back-contact design (IBC cell) as illustrated in Figure 8.

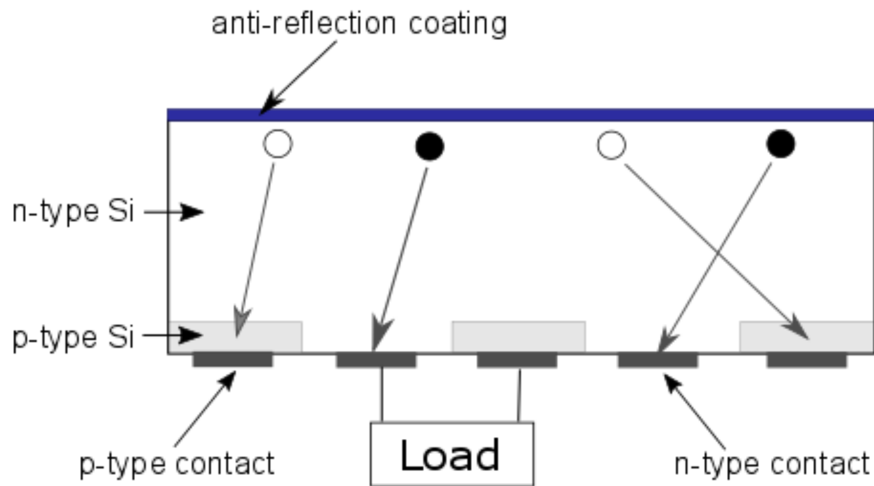

Figure 8. Schematic of an interdigitated back contact (IBC) silicon solar cell. Hollow circles are holes. Filled circles are electrons.

The bulk of the cell is generally made from n-type single crystal silicon, the top surface is covered in an antireflection coating as before, but on the back surface the contacts alternate between hole-collectors and electron-collectors. At each hole-collector there is a localised p-type silicon region; this creates a localised p-n junction to aid the efficient capture of holes.

However, the IBC cell design still has its challenges. Unless the minority carriers reach the p-n junction (at the rear of the cell), they will not contribute current to the external circuit. The p-n junction in an IBC cell, compared to an Al-BSF conventional cell design, is much further from the front surface, where carriers are mostly generated. Thus, the minority carriers must travel much further without recombining before they reach the junction. The diffusion length, *L*, of a carrier is related to the time for which the carrier exists before recombination, known as the carrier lifetime, τ, and the diffusion coefficient, *D*,:

$$L = \sqrt{D\tau} \tag{1.1}$$

In order to increase *L*, the carrier lifetime must also be increased. This is achieved by reducing recombination. The mechanisms by which this can happen have been mentioned briefly and will covered in detail in Chapter 2.

The majority of recombination in moderately doped (1 Ωcm) silicon occurs at electrically active defect sites, such as surfaces, dislocations and grain boundaries. Defects can introduce energy levels into the forbidden bandgap that are accessible to carriers, which act as recombination centres. In order to reduce recombination, the surfaces, crystal defects and grain boundaries are passivated. In this work passivation is defined as the reduction in recombination activity of a defect or surface.

In IBC cells, in order to reduce the number of defect sites in the bulk, such as electrically active grain boundaries, high purity, single crystalline silicon is used. This, along with the switch from p- to n-type silicon, reduces recombination in the bulk and increases carrier lifetime due to the inherently higher lifetime of n-type material [19]. There are two main reasons that single crystal n-type silicon has a higher lifetime. Firstly, defect-mediated recombination in the bulk of n-type Si is lower. This is because of the lack of dopant-related defect levels common in boron doped p-type silicon [20]. Secondly, the interface properties between n-type Si-SiO_2 induce less recombination than p-type Si-SiO_2 because of the difference in capture cross sections of holes and electrons [17]. However, despite a reduction in the recombination within the bulk of the silicon, recombination at the silicon surface is still prolific. This is because the surface is a large, abrupt disruption to the silicon crystal lattice, meaning it can be highly recombination active. These defects, which introduce an abundance of states into the forbidden bandgap of the silicon semiconductor surface, serve as recombination centres for the photo-generated carriers. The need to reduce recombination at the surface in a commercially-appropriate manner is thus of great importance in producing high efficiency silicon solar cells.

At present, IBC cells are available commercially, and are able to provide a 20% relative increase in efficiency compared to a standard industry cell [21, 22]. However, in order to

achieve sufficient surface passivation, a doping profile at the silicon surface is used, as will be discussed in Section 1.4.2.1. This technique is not the most effective way of passivating a front surface because it can increase recombination in the near-surface region. In order to allow the IBC cell structure to reach its potential efficiency, an alternative surface passivation technique is necessary; one that is cheap, yet more effective than the present-day version. By developing such a technique, the efficiency of silicon PV cells may be able to increase, thus reducing the cost per watt installed, leading to an increased uptake of solar. In the following sections, the means of reducing surface recombination, which is known as surface passivation, will be discussed.

1.4 Silicon Surface Passivation

Surface passivation comprises all methods by which recombination is reduced at the surface of the silicon substrate. Surface recombination is dominated by defect-mediated recombination, so three elements are necessary for recombination to occur: an electron, a hole and an electrically-active defect. If one of these components is unavailable, recombination is reduced significantly to radiative and Auger recombination only. The different types of recombination will be described in Chapter 2, section 2.2. There are two main schemes by which a surface can be passivated. This is either by the reduction of bandgap states (i.e. the removal of defects), termed chemical passivation, or by reducing the concentration of one type of carrier from the surface, called field effect passivation (FEP). Chemical passivation is generally achieved using a dielectric capping layer, or hydrogen, whereas, FEP is commonly achieved using charge. Chemical passivation and FEP can be used independently or in conjunction with one another and are illustrated in Figure 9. Methods by which both of these schemes can be employed are now discussed.

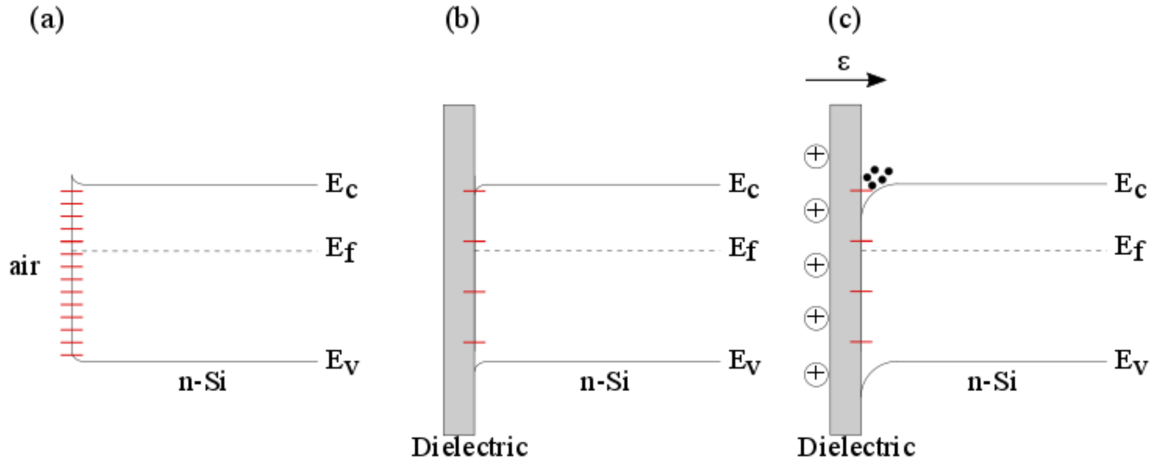

Figure 9. Schematic showing the effect on bandgap states (red lines) and silicon energy bands of a) a bare silicon surface, b) a chemically passivating dielectric layer and c) a chemically passivating dielectric layer with the addition of field effect passivation.

It is now necessary to differentiate between passivation that is inherent to the dielectric, introduced during growth or deposition, which is intrinsic passivation and passivation that can be incorporated afterwards to supplement this, which is extrinsic passivation. The benefit of extrinsic passivation is that the growth or deposition parameters no longer have to be adjusted in an attempt to optimise intrinsic passivation. Instead, they can be optimised to improve optical properties of the cell.

1.4.1 CHEMICAL PASSIVATION

There are two key methods used to chemically passivate a surface. The first is a dielectric capping layer, the second is hydrogen. Often, the two are used in conjunction with one another. They chemically passivate because the dielectric or hydrogen atoms bond to some of the unsatisfied silicon surface atoms, thereby reducing the number of recombination active defects in the bandgap.

Surface defect density, also referred to as interface trap density at midgap (D_{it}), is often used to define the quality of surface chemical passivation. This metric will be discussed in

Chapter 2 and is used throughout this section in an effort to separate chemical passivation from field effect passivation.

1.4.1.1 Dielectric Capping Layers

Although silicon grows a native oxide of a few nm, it is common practice for this to be removed because it does not provide high-quality chemical passivation. This is replaced by a dielectric layer, which has several purposes. On the top surface, one of the reasons a dielectric is useful is as an antireflection coating. This is necessary because a bare silicon surface is extremely reflective. Another property of the dielectric is as a chemical passivator, which is of use on both the top and back surface. Some dielectrics are more effective chemical passivators than others due to their deposition techniques and/or atomic structure. The most promising dielectrics are silicon dioxide (SiO_2), silicon nitride (SiN_x) and aluminium oxide (Al_2O_3). Different dielectrics are appropriate for the front and rear surface. SiO_2 is generally used on either surface for its superior chemical passivation [17]. Whereas, SiN_x generally is used on the front surface. This is for three reasons: the appropriate antireflection properties, the hydrogen passivation the deposition process introduces and the intrinsic positive charge that works to provide FEP by putting the surface of the n-type silicon into accumulation. On the other hand, Al_2O_3 is used predominantly on PERC (Passivated Emitter Rear Contact) cells, which require the rear p-type surface to be passivated between the contacts [23]. The growth/deposition processes and the properties of these dielectrics are now described in more detail.

1.4.1.1.1 Silicon Dioxide

The first capping layer to be mentioned is silicon dioxide as it is capable of providing the highest quality chemical passivation [20]. There are three main techniques for producing a silicon dioxide capping layer. It can be thermally grown under either wet or dry conditions, or it can be deposited using a CVD (although this method is not frequently used due to relatively poor chemical passivation [24]). A dry thermal oxide provides the best chemical passivation with a typical defect density at midgap of ~10^{10} $cm^{-2}eV^{-1}$ [25, 26], but this can be as low as 10^9 $cm^{-2}eV^{-1}$ [17]. However, dry oxidation is a lengthy, costly process and normally requires temperatures exceeding 900 ˚C. It is preferable to avoid these temperatures because of expense and contamination risk. In order to grow a dry oxide of 100 nm, the silicon wafer would require 1 hour at 1100 ˚C [27]. On the other hand, a wet oxide produced at the same temperature would only take 3½ minutes to reach this thickness [27]. As a wet oxide growth rate is higher, lower temperatures are often used. This can result in a poorer interface quality between the Si and the oxide as the bonds are not able to re-organise sufficiently to reduce the density of interface traps. The inherent charge density of an oxide film itself is low, resulting in almost negligible intrinsic FEP. In addition to this, both types of thermally grown silicon dioxide are incapable of providing a good antireflection coating due to the refractive index. Therefore, it is not sufficient as a top surface antireflection coating in its own right.

1.4.1.1.2 Silicon Nitride

Silicon nitride (SiN_x) provides a better antireflection coating because of its refractive index (1.9 – 2.5), which can be tuned to be well suited for use between silicon and the encapsulant glue, where a value of ~2.4 is optimal [28]. SiN_x is usually deposited by Plasma Enhanced Chemical Vapour Deposition (PECVD) and the refractive index is dependent on the deposition parameters. This process takes only minutes [29], but requires a vacuum and the

resulting chemical passivation is only able to lower the density of interface traps to ~ 10^{11} $cm^{-2}eV^{-1}$ [30]. It is important to note that this chemical passivation is not due to the presence of the SiN_x film alone but incorporates an aspect of hydrogenation which is intrinsic to the SiN_x deposition process. Hydrogenation is discussed in more detail in section 1.4.1.2, however, in brief, the hydrogen present within the PECVD chamber during the nitride deposition diffuses to the silicon surface and satisfies dangling bonds. Silicon nitride also has a substantial intrinsic positive charge, providing FEP, which will be discussed in Section 1.4.2.2. Historically, silicon nitride has been the industry standard top-surface dielectric for the majority of cell structures because of its antireflection properties, intrinsic positive charge and its benefit of being a source of atomic hydrogen. However, even with the aid of hydrogen passivation, the chemical passivation provided by a nitride capping layer is not comparable to that provided by a dry oxide. Because of this, high efficiency cell structures are said to now be incorporating a thin oxide interface layer (less than10 nm) between the silicon and nitride layer. For this reason, this thesis focuses on the use of SiO_2 as the dielectric. For completeness, aluminium oxide is now discussed.

1.4.1.1.3 Aluminium Oxide

The final capping layer to be mentioned is aluminium oxide. It can either be deposited using a PECVD technique or by atomic layer deposition (ALD). After deposition, an activation anneal is required to activate the passivation [31, 32]. Dingemans et al [33] have shown that, during the anneal, hydrogen is released from the Al_2O_3 film and passivates the silicon surface. An Al_2O_3 film reduces the interface trap density at midgap to ~10^{11} $cm^{-2}eV^{-1}$ [31, 34, 35]. However, it is the large negative charge (10^{13} q/cm^2 [34, 35]) of the film that provides a substantial proportion of the passivation by means of field effect. Due to the polarity of the charge, AlO_x is more suitable for use on back surfaces of p-type. These

surfaces are found in Passivated Emitter Rear Contact (PERC) cells, which are becoming very common in the industry, but which are not discussed in this work.

In both silicon nitride and aluminium oxide, a substantial proportion of their intrinsic passivating properties are due to the presence of hydrogen. Hydrogen can also be introduced by extrinsic techniques, decoupled from the deposition process, which are summarised.

1.4.1.2 Hydrogen

As mentioned previously, dielectric deposition can be a source of hydrogen for passivation, as it is for SiN_x. Hydrogen can also be used to improve the chemical passivation of SiO_2 or other dielectric layers. All chemical passivation discussed so far has been intrinsic, either due to hydrogen introduced during the deposition process or from the dielectric bonds with silicon. However, it is possible to improve the chemical passivation extrinsically, by the addition of hydrogen after dielectric deposition.

1.4.1.2.1 Forming Gas Anneal

A forming gas anneal (FGA) which is 5% H_2, 95% N_2 [36] is commonly performed on oxidised silicon wafers to improve the chemical passivation. It is especially effective on poor quality oxides where the original chemical passivation has greater room for improvement. Reed and Plumber [37] were able to improve the interface trap density by an order of magnitude (from 10^{11}–10^{10} $cm^{-2}eV^{-1}$) during a 10 minute FGA at 280 ˚C. However, on an industrial scale, this 10-minute anneal is not used. This is because for a process of this length, a large factory foot-print would be required to achieve the 1 wafer per second throughput.

1.4.1.2.2 Remote Plasma

Hydrogen can be introduced to dielectrics through exposure to a hydrogen containing plasma. However, it is vital that the sample is not exposed to the high energy plasma or the associated hard UV directly as this can damage the surface [38]. Remote plasma devices allow the hydrogen to reach the sample but avoid a line-of-sight between the sample and the plasma, thereby reducing damage. This requires specialist equipment and because of this is not widely used.

1.4.1.2.3 Shielded Hydrogen Passivation

Shielded Hydrogen Passivation (SHP) is a recently developed technique whereby hydrogen can be introduced to the Si-dielectric interface in PECVD equipment [39, 40]. A palladium shield prevents damage caused by charge build up on the dielectric surface and from UV. In 2017, Bourret-Sicotte et al [40] found that SHP alone could improve the carrier lifetime of thermally oxidised 1 Ωcm n-type FZ Si by almost two orders of magnitude, from 12 µs to 1050 µs. Interface trap density is not stated; however, it must be exceptionally low as with the addition of FEP the lifetime improved to 6300 µs, which at the time was the record passivation of a single layer oxide-silicon interface. This would only be possible with an extremely well chemically passivated interface.

At this point, one must recall that surface passivation is not purely about interface trap density. High quality passivation relies heavily on the field effect aspect of passivation and the methods to achieve it will now be outlined.

1.4.2 FIELD EFFECT PASSIVATION

Although good quality chemical passivation is vital in reducing surface recombination, in order to provide outstanding passivation, this must be supplemented by FEP. There are two

main techniques to control the carrier concentration at the surface, thus limiting the access of one type of carrier to the recombination active region. One is the introduction of a doping profile to the near-surface silicon, which produces an internal electric field. The other is the presence of charge in or on the dielectric capping layer which causes charge of the same polarity to be repelled within the near-surface silicon.

The overall passivation of the surface can be characterised by the surface recombination velocity (SRV). The better the passivation of the surface and the lower the recombination rate, the lower the SRV. Throughout this section SRV will be used to characterise the combined chemical and field effect passivation of the surface, along with charge density values to indicate the strength of the field effect passivation. A more complete description of the surface recombination velocity parameter will be given in Chapter 2.

1.4.2.1 SURFACE DOPING

By varying the concentration of dopant atoms with depth into the silicon, an electric field can be produced within the silicon, which limits the access of carriers. Another benefit of this method is that, by varying the doping concentration, the mobility of the minority carriers varies, decreasing as the doping concentration increases. By decreasing the mobility of the minority carriers, the availability of carriers for recombination is reduced.

This process can be used on either surface of the silicon to produce a back surface field (BSF) or a front surface field (FSF). A back surface field is traditionally achieved in an Al-BSF cell design, as discussed previously, by annealing the aluminium-silicon interface at ~ 800 ˚C, the eutectic point. On cooling, a pp^+ layer is formed at the back of the cell which repels electrons from the surface, reducing their access to the surface defects and ensuring reduced back surface recombination [41, 42].

The front surface field for a n-type IBC cell, as in Figure 8, can be produced by diffusing phosphorus into the surface silicon usually by annealing in $POCl_3$ gas at 800-900 ˚C [43]. This creates an n^+n region at the front surface of the silicon which reduces the concentration of holes at the front surface defects and thus delivers FEP. This FSF technique, although effective, has two major disadvantages. Firstly, it is a relatively expensive, slow process that requires high temperatures making it unappealing commercially [44]. Secondly, the presence of the n^+ region at the surface has the undesired effect of reduced blue light energy conversion [45]. This is reduced due to high levels of Auger recombination, which was mentioned in 1.2.2 and covered in more detail in Chapter 2. Because of its short wavelength, blue light is absorbed in this region of high Auger recombination, which is the highly doped n^+ region, meaning that many of these electron-hole pairs recombine and are unable to provide useful energy.

1.4.2.2 CHARGED FILMS

An alternative source of FEP is the presence of charge in or on the dielectric, or at the interface of the dielectric with the silicon. This reduces carrier access to the surface, but, unlike a front surface field, it does not introduce an area of high recombination. In most instances, an accumulation region at the passivated surface is desirable, so that it is the access of the minority carriers to the silicon surface that is restricted. Therefore, silicon dioxide and silicon nitride, which have a built in positive charge [46, 47], tend to be used on n-type silicon, whereas aluminium oxide, which has a fixed negative charge [35, 48, 49] is more appropriate for the passivation of p-type material. This charge density is more substantial for some dielectrics than others and is usually given in units of elementary charges per square unit (q/cm^2). For example, thermally grown SiO_2 has a small positive charge density of 10^{11} q/cm^2 [46], whereas PECVD deposited SiN_x can have a positive charge density of 2×10^{12} q/cm^2 [47]. In comparison, Al_2O_3 has a much larger intrinsic

negative charge density in the order of 10^{13} q/cm^2 [35]. The focus of this thesis will be on passivation appropriate for n-type Si.

By considering the overall effectiveness of the as-deposited SiO_2 and SiN_x surfaces at passivating, the influence of both chemical and field effect passivation is evident. SiO_2, which has a chemical passivation an order of magnitude greater than that of SiN_x but negligible dielectric charge, is capable of producing surfaces with a SRV of 13 cm/s on 1 Ωcm n-type FZ Si [50]. In comparison, SiN_x films can have a larger intrinsic charge depending on deposition parameters. Richter et al [51] have been able to produce SiN_x films with a SRV of 0.75 cm/s on 1 Ωcm n-type Si.

Although the SiN_x film may now appear to offer superior passivation than the SiO_2 film, the SiO_2 film passivation can be vastly improved by the addition of FEP, or by improving the chemical passivation with hydrogen. Through the addition of FEP and hydrogen, Bourret-Sicotte et al [39, 40] have improved the quality of a SiO_2-Si surface to give a SRV of 0.17 cm/s on 1 Ωcm n-type FZ Si. In the present work, this was improved upon further where a SiO_2-Si interface with a SRV of 0.05 cm/s was produced, which is shown in Chapter 4. To the author's best knowledge, this is a new record for silicon surface passivation, with the exception of amorphous silicon, and highlights that both high quality chemical and high-quality field effect passivation is required in order to produce surfaces of low recombination.

Modelling by Bonilla [52] has indicated that to achieve excellent field effect passivation, a charge concentration of 2-5 x 10^{12} q/cm^2 is appropriate. Beyond this, the charge concentration is not seen to significantly improve the SRV [25, 53]. To obtain a charge concentration of this magnitude, it is desirable to supplement the intrinsic charge. This is especially true if one wishes to exploit the high-quality chemical passivation of SiO_2. There

are several means by which extrinsic FEP can be introduced, and they are outlined in the following section.

By adding charge extrinsically, the charge concentration is decoupled from the dielectric deposition process, meaning that charge concentration does not have to be compromised in an attempt to optimise other characteristics. For example, the charge density of a SiN_x film varies with stoichiometry, as do the antireflection properties. For this reason, it is not possible to optimise charge density (FEP), chemical passivation and antireflection properties during a deposition. By enabling charge to be deposited extrinsically, the necessity for other parameters to be compromised is removed.

1.5 Methods of Extrinsic Field Effect Passivation

There are two methods of charging dielectric films that will be discussed in this section. One makes use of a corona discharge, which is produced by ionising molecules in the air. The other method employs diffusion and drift mechanisms to introduce atomic ions into the dielectric.

1.5.1 Corona Discharge

A corona is produced by applying a very high voltage (tens of kV) to a metal pin. This ionises molecules in the air which drift to the surface of the sample which is positioned on a grounded plate. It is a technique that has been used for decades [54, 55], but which, historically, has been viewed as a characterisation technique and not considered commercially suitable for passivation due to the decay of the corona charge.

Corona charging is extremely effective. Bonilla has produced SRVs of 1.6 cm/s on 1 Ωcm n-type FZ Si [56] and 0.65 cm/s on forming gas annealed 1 Ωcm n-type FZ Si [56]. However, it is well known that corona charge is not stable and the surface charge will disperse within several hours to several days [25, 56, 57]. This decay is believed to be caused by lateral conduction due to mobile surface ions, many of which are derived from the interaction of water with SiO_2 [58]. Therefore, by preventing access of atmospheric water to the dielectric surface, one can vastly improve the long term stability of the charge [56]. This is believed to be the reason that corona discharge is less stable on a wet thermal oxide than a dry one [17]. One method for stabilising the corona charge is the deposition of an extremely hydrophobic layer, hexamethyldisilazane (HMDS) [52, 56, 57, 59–61] as it prevents lateral surface conduction by reducing the access of water to the oxide surface. It has been seen to be effective, increasing the stability of corona charge to an effective lifetime decay time constant of > 20 years, instead of days [56] under room temperature conditions. However, it is unclear how the HDMS monolayer will interact with the EVA glue necessary for encapsulation. As an alternative, an improved method to combat the issue of charge stability is the introduction of permanent, charged ionic species into the dielectric layer which are immobile and quenched in.

1.5.2 IONIC CHARGE

Bonilla et al [61, 62] have found the introduction of Na^+ and K^+ into SiO_2 at concentrations of 5×10^{12} q/cm^2 to provide effective FEP. The improved lifetimes of samples containing K^+ are seen to be stable over 4 years, with a decay time constant of over 46 years at room temperature [62], which is more suitable for commercial solar cells designed to last over 30 years. However, the process by which ions are introduced is not appropriate for large scale and an alternative must be developed. Moreover, the migrated ions sit at the Si-SiO_2

interface and there is concern that, in large concentrations, the presence of these ions may damage the chemical passivation. Both of these issues form a focus of this doctoral thesis.

1.6 ALNEAL

The alneal is another extrinsic passivation technique discovered by Eades [63]. An alneal can produce SRVs as low as 1.7 cm/s on 1.5 Ωcm n-type Si. It has been widely accepted for decades that the passivation afforded by the alneal is purely chemical. The standard alneal is achieved by evaporating a thin, ~0.1 μm layer of aluminium onto the oxide surface and annealing in forming gas at ~400 ˚C for ~30 minutes. Inert gases without hydrogen have found to be almost as effective [37], indicating any chemical passivation is not caused by an external hydrogen source. After the anneal, the aluminium is removed using phosphoric acid at 90 ˚C [64]. It is believed that hydrogen is released due to aluminium interaction with hydroxyl ions present in the oxide [65] and this hydrogen is then free to diffuse and passivate any surface defects. A more complete review of the literature can be found in Chapter 4.

1.7 BEST SURFACE PASSIVATION AT TIME OF WRITING

In recent years, a wide number of extremely effective passivation methods have been proposed, especially with the advances in PECVD and atomic layer deposition (ALD) methods. Table I illustrates a comparison of the surface recombination velocities for high quality passivation techniques on n-type Si because n-type has higher lifetime values than p-type. The values quoted were calculated by Bonilla et al. in reference [66], using a new evaluation technique. Bonilla applied this technique to many research papers in order to allow for a more accurate comparison. This technique was then applied to the data provided

in the papers referenced within Table I. For this reason, the values for Surface Recombination Velocity (SRV) and surface saturation current density (J_{0s}) quoted in the table will vary slightly from those given in the papers.

The resistivity of the silicon is given because the SRV is dependent on it; high resistivities allow for low SRV values. The thickness is quoted for completeness as it is used to calculate the SRV from the measured effective lifetime. The surface recombination velocity (SRV) and surface saturation current density (J_{0s}) are given.

Table I. Summary of the best passivation achieved by several high-quality passivation dielectrics [66]

Dielectric	Passivation	Type	SRV (cm/s)	J_{0s} (fA/cm^2)
SiO_2	Standard Alneal Kerr & Cuevas [64]	n-type 1.5 Ωcm 285 μm	1.7	10.9
SiO_2	Extrinsic FEP (Corona) Bonilla et al. [56]	n-type 1.Ωcm 200 μm	1.6	4.6
SiO_2	Extrinsic FEP (corona) and H passivation (SHP) Bourret-Sicotte et al. [40]	n-type 1.Ωcm 200 μm	0.17	0.5
SiN_x	SiN_x Richter et al. [51]	n-type 1.Ωcm 200 μm	0.64	0.2
AlO_x	AlO_x (ALD) Richter et al. [51]	n-type 1.Ωcm 200 μm	0.26	2.1
a-Si amorphous silicon	a-Si/SiO_2/SiN_x (PECVD) Bonilla et al. [67]	n-type 1.Ωcm 200 μm	0.06	0.2

1.8 Aim of this work

In the transition towards high-efficiency cell geometries, there is a significant need for excellent quality surface passivation to be attained using commercially viable processes. To achieve this goal, both superior chemical and field effect passivation is necessary. Industry is shifting towards more frequently incorporating a thin oxide layer below the antireflection coating in order to satisfy the chemical passivation. However, the field effect passivation is most commonly only provided by the intrinsic charge of the silicon nitride antireflection coating. This charge concentration is not optimal. Thus, there is a pressing need for an extrinsic technique of providing field effect passivation at an industrial scale.

The aim of this thesis is to propose an industrially suitable ion introduction technique, quantify the concentration of charge at the oxide-silicon interface that gives the best carrier lifetimes and to investigate ionic species other than sodium and potassium. On the path to achieving this, it is vital to understand the mechanism behind the success of the alneal process which provides such excellent passivation.

1.9 Structure of this thesis

An introduction to photovoltaic devices, the need for passivation and the common mechanisms by which this is achieved has been given in Chapter 1. Further background science is overviewed in Chapter 2 before the experimental methods used throughout the thesis are described in Chapter 3. Chapter 4 presents the initial characterisation of the alneal and the system dynamics are investigated in Chapter 5. The focus of the thesis then shifts towards developing an industrially appropriate ion deposition and migration process in Chapter 6, using the findings of Chapters 4 and 5. Chapter 7 then describes the finer detail

of improving the proposed process for use in industry and the use of alternative, potentially more stable, ionic species. The thesis is summarised in Chapter 8 along with comments on potential future work.

CHAPTER 2
BACKGROUND LITERATURE ON RECOMBINATION AND SURFACE PASSIVATION

2.1 RECOMBINATION THEORY

Recombination results in the loss of potential electrical energy as an electron-hole pair meets and neutralises before being able to produce an external current in a solar cell. In thermal equilibrium, the rate of generation, *G*, is equal to the rate of recombination, *R*. For n-type doped silicon, at thermal equilibrium, full ionisation of donor atoms is assumed so that the electron carrier concentration, *n*, at equilibrium $n_0 = N_D$, where subscript '*0*' indicates equilibrium conditions and N_D is the concentration of donor atoms. The hole carrier concentration is *p*.

Under illumination, the total carrier concentration increases as excess carriers are injected into the silicon. The excess carrier concentration, Δn, is described as $\Delta n = n - n_0$. The carrier concentration at thermal equilibrium, n_0, is given by equation (2.2).

$$n_0 = n_i e^{\frac{E_F - E_i}{kT}} \tag{2.2}$$

where E_F is the Fermi energy, E_i is the intrinsic energy level of the undoped silicon, k is the Boltzmann's constant, T is the temperature in Kelvin and n_i is the intrinsic carrier concentration of the undoped silicon.

In the case where charge neutrality can be assumed and carrier trapping sites can be regarded as negligible, it is reasonable to assume that the excess injected carriers are equal, and that $\Delta n \approx \Delta p$ [68]. In order to return to equilibrium, the excess carriers attempt to recombine. The time taken for the excess minority carriers, Δp in n-type, to recombine is known as the minority carrier lifetime, τ. Historically, the majority of silicon PV devices used p-type silicon, therefore, it is convention to denote the minority carrier concentration as Δn, regardless of silicon type. The time constant of this recombination process is given by:

$$\tau = \frac{\Delta n}{U} \tag{2.3}$$

where U is the net recombination rate, $U = R - G$. Minority carriers are used to characterise this rate because, due to carrier concentrations, they are likely to have shorter lifetimes and, therefore, are the limiting factor. It is also reasonable to assume that the minority carrier concentration at equilibrium is negligible compared to that of the majority carrier. Thus, the minority carrier concentration under illumination is approximately the excess carrier concentration.

As mentioned previously, in comparison to a conventional cell with front and back contacts, in the IBC cell design the minority carriers have further to diffuse between the region where they are generated and the p-n junction. It is therefore vital that the average diffusion length of a minority carrier, L, is as large as possible. Recalling that $L = \sqrt{D\tau}$ and knowing that

diffusivity is fixed, the minority carrier lifetime must be increased in order to achieve the diffusion length.

The lifetime of a minority carrier depends on both the bulk lifetime and the effect of recombination at the surface. The average lifetime of a carrier is therefore a combination of bulk lifetime, τ_B, and surface lifetime, τ_S, known as the effective lifetime, τ_{eff}, as shown in equation (2.4).

$$\frac{1}{\tau_{eff}} = \frac{1}{\tau_B} + \frac{1}{\tau_S} \tag{2.4}$$

2.2 BULK RECOMBINATION

Bulk recombination describes the recombination that occurs away from the surfaces, within the silicon structure. As discussed in Chapter 1, there are three types of bulk recombination. These are radiative, Auger, and defect mediated recombination which is modelled by Shockley-Read-Hall (SRH) statistics. As the bulk lifetime will be affected by all of these, and often dominated by the shortest, the bulk lifetime can be written as:

$$\frac{1}{\tau_B} = \frac{1}{\tau_{rad}} + \frac{1}{\tau_{Aug}} + \frac{1}{\tau_{SRH}} \tag{2.5}$$

Bulk recombination can be classified as two types: intrinsic or extrinsic. Intrinsic mechanisms (radiative and Auger) would occur even if the lattice was perfect, whereas extrinsic recombination (SRH) is defect mediated. These three recombination mechanisms are discussed below and the most widely accepted intrinsic and extrinsic lifetime models at the time of writing are presented.

2.2.1 RADIATIVE RECOMBINATION

Radiative recombination occurs when an electron-hole pair recombine and release a photon in order to dissipate the excess energy. Silicon is an indirect bandgap material, which means that the conduction band minimum energy and valance band maximum energy are offset in momentum-space, as shown in Figure 10.

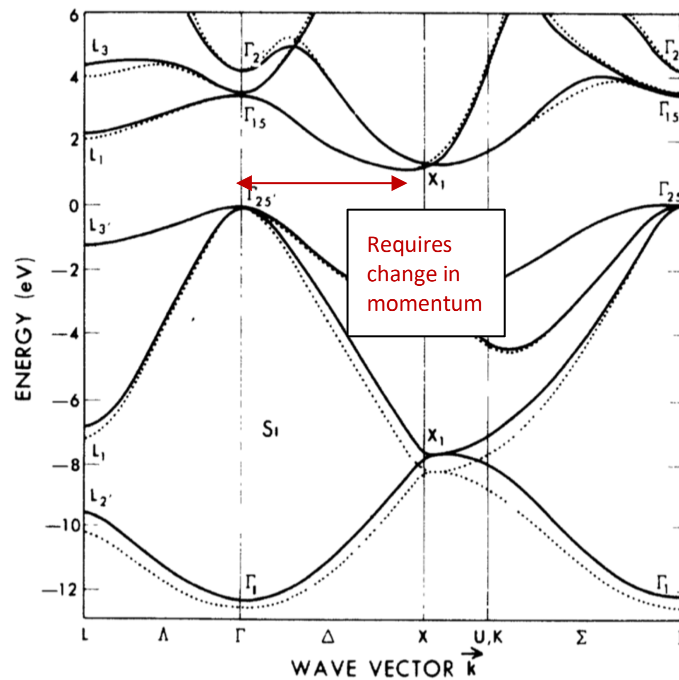

Figure 10. Energy band diagram for silicon showing the offset between the conduction and valence band in momentum-space that results in the requirement for a change in momentum. After [69]**.**

Therefore, a change in momentum is also required to enable the electron to move from the conduction to the valence band. This makes the radiative recombination mechanism less probable in indirect bandgap material than direct bandgap material. The rate of radiative recombination is given by equation (2.6) [70].

$$U_{rad} = B(np - n_i^2) \tag{2.6}$$

where B is a scaling constant. Using equation (2.3) and the assumption that $\Delta n \equiv \Delta p$ the radiative recombination lifetime can be given by equation (2.7) [71].

$$\tau_{rad} = \frac{1}{B(\Delta n + n_0 + p_0)} \tag{2.7}$$

In 2006, Altermatt [72] took into account Coulombic attraction between carriers and revised the coefficient B, previously calculated by Gerlach [73]. Altermatt [74] found that as carrier density increased, either due to doping concentration or carrier injection, B decreased. In order to characterise this, B was scaled according to the value calculated at very low carrier injection, B_0, so that $B = B_0 B_{rel}$. The values given by Altermatt in reference [74] are used to calculate radiative recombination.

2.2.2 Auger Recombination

Auger recombination occurs when, instead of the excess electron energy being released as a photon, it is passed to another carrier, along with the necessary momentum exchange [75]. This third carrier is excited further into its respective band, only to relax back to its original energy shortly afterward. As Auger recombination requires three carriers (two carriers of the same type and one of the opposite), it predominantly occurs in material which is either highly doped or under high injection conditions [70]. In the 1970s, it was believed that a weighted average of the two recombination types could be achieved by using coefficients that were constant regardless of carrier concentration. However, at low carrier concentration experimental results did not match well with the Auger recombination extrapolated from calculations at higher carrier concentrations [76, 77]. To address this, Hangleiter and Hacker [78] included Coulomb interactions between carriers in the Auger model. This was accomplished by the addition of enhancement factors g_{eeh} and g_{ehh}. This model only

qualitatively agreed with experimental data and was later replaced by a general parameterization of Coulomb-enhanced (CE) Auger recombination proposed by Kerr and Cuevas [79]. Within this parameterization, the interaction of mobile charge carriers with dopant ions was considered and thus both the dopant concentration and injection level are taken into account. However, this model was still found to underestimate the upper limit for Auger lifetime [51] and today the most commonly used model is that proposed in 2012 by Richter et al. [51]. and is given by equations (2.8)-(2.11).

$$\tau_{AugRich} = \frac{\Delta n}{(np - n_{i,eff}^2)(2.5 \times 10^{-31} g_{eeh} n_0 + 8.5 \times 10^{-32} g_{ehh} p_0 + 3.0 \times 10^{-29} \Delta n^{0.92})} \quad (2.8)$$

$$n_{i,eff} = n_i e^{\frac{\Delta E_g}{2kT}} \quad (2.9)$$

$$g_{eeh} = 1 + 13\left\{1 - tanh\left[\left(\frac{n_0}{N_{0,eeh}}\right)^{0.66}\right]\right\} \quad (2.10)$$

$$g_{ehh} = 1 + 7.5\left\{1 - tanh\left[\left(\frac{p_0}{N_{0,ehh}}\right)^{0.63}\right]\right\} \quad (2.11)$$

where $\mathrm{N_{0,eeh}} = 3.3 \times 10^{17} \mathrm{cm^{-3}}$ and $\mathrm{N_{0,ehh}} = 7.0 \times 10^{17} \mathrm{cm^{-3}}$.

2.2.3 DEFECT MEDIATED RECOMBINATION

Defects in the crystal lattice such as missing atoms, impurities, dislocations, grain boundaries and surfaces cause previously forbidden energy levels in the bandgap to become accessible. These energy levels aid the movement of carriers between bands and therefore assist recombination. The model for a single defect state was proposed by Shockley, Read

[80] and Hall [81] and considers the bulk recombination rate made possible by this single state, given by equation (2.12)

$$U_{SRH} = \frac{(np - n_i^2)}{\left[\frac{(n + n_1)}{N_t \sigma_p v_{th}} + \frac{(p + p_1)}{N_t \sigma_n v_{th}}\right]} \tag{2.12}$$

where v_{th} is the thermal velocity of the carrier and $\sigma_{n,p}$ is the capture cross section of a given defect for each carrier type. N_t is the trap density at a given energy level in the bandgap. The density of carriers at the trap energy are given by occupation probabilities n_1 and p_1 [68, 70].

$$n_1 = n_i e^{\frac{E_t - E_i}{kT}} \qquad p_1 = n_i e^{\frac{E_i - E_t}{kT}} \tag{2.13}$$

This model assumes that the defects only produce traps at one energy level in the bandgap. However, for some defects, for example a grain boundary, dislocation or a surface, this is not the case. At these locations, an array of traps at different energy levels are created and they can be present throughout the bandgap. Under these circumstances, it is necessary to sum the effect of all the trap states over the bandgap, as is discussed in Section 2.3. Before this, the limiting recombination mechanism in the bulk is considered.

2.2.4 LIMITING RECOMBINATION MECHANISM

In order to increase the overall effective lifetime of charge carriers, it is necessary to improve the lifetime of the limiting component. This can be within the bulk or at the surface. This section considers limitations due to the bulk lifetime and means by which the bulk lifetime could be increased. Firstly, the intrinsic radiative lifetime cannot be controlled by means other than doping, however in an indirect bandgap material it does not account for a

significant proportion of recombination. Secondly, Auger lifetime is intrinsic to the semiconductor and dependent on the doping concentration. Solar cells are not highly doped, and for this reason Auger lifetime within the bulk of the material is relatively long and not a limiting factor unless under high carrier injection. However, with the trend towards highly doped emitters to provide front surface fields, discussed in section 1.4.2.1, this cannot be said for the emitter region. In the emitter, Auger recombination can be significant and limiting, which is not desirable. This work aims to provide an alternative to highly doped FSFs for passivation and thereby reduce Auger recombination in this region. Finally, the SRH lifetime can be improved by using single crystal silicon. There are two dominant techniques used to grow single crystal: Czochralski (Cz) and Float Zone (FZ). Cz-Si is cheaper and although not defect-free, has a low concentration of defects and impurities. In this work, FZ-Si was used for lifetime specimens to further decrease the likelihood of defects. Until recently, FZ-Si was deemed to be defect-free. However, in the last couple of years, work by Grant et al. [82–85] has shown that defects, likely to be lattice-impurity defects, can exist in FZ silicon. In certain cases, these defects can be lifetime-limiting. However, the process of thermal oxidation, using temperatures over 1000 °C, is seen to de-activate the defect. As all samples in this study have undergone oxidation, this defect should not affect this work.

The characterisation of surface recombination is now considered. Due to the large number of energy levels present in the bandgap at the silicon surface, this region becomes a significant limiting factor in the overall effective lifetime. In order to reduce the SRV, the surface is passivated, as described in Chapter 1.

2.3 SURFACE RECOMBINATION

The silicon surface is inherently a large crystal 'defect' as the surface silicon atoms have unsatisfied bonds. This leads to defect energy states being distributed continuously and non-uniformly throughout the bandgap, which act as recombination centres. As it is no longer the case that only a single energy level is available in the bandgap, see section 2.6, the total SRH recombination must be found by integrating the recombination at every energy level across the bandgap:

$$U_s = (n_s p_s - n_i^2) v_{th} \int_{E_v}^{E_c} \frac{D_{it}(E)}{\frac{n_s + n_1(E)}{\sigma_p(E)} + \frac{p_s + p_1(E)}{\sigma_n(E)}} dE \tag{2.14}$$

where $D_{it}(E)$ is the density of interface states with respect to energy, $E,$ and n_s and p_s are the electron and hole concentrations at the surface. The capture cross-sections are $\sigma_{p/n}$ and n_1 and p_1 refer to the carrier concentration that would exist if the Fermi level was at the trap energy [17]. It is important to note that from SRH statistics the effectiveness of a trap as a recombination centre will vary with location of trap energy within the bandgap and also with its carrier capture cross-section. Traps at energy levels close to the middle of the bandgap are more effective recombination centres than those near the band edges.

From U_s the ideal surface recombination velocity (SRV) is conventionally defined as S_0 equation (2.15).

$$S_0 \equiv \frac{U_s}{\Delta p} \tag{2.15}$$

The SRV describes the ease with which recombination takes place at the surface and has units of $\mathrm{cm/s}$. A low SRV indicates low surface recombination, which is desirable. The

SRV is dependent on doping concentration and injection level, and these must be stated in order for the value of SRV to be meaningful [86].

Until now, only the ideal situation has been considered, when the conduction and valence bands within the semiconductor are flat all the way up to the silicon surface. However, this is not the practical situation. Generally, there is a region just under the surface of the silicon where the bands bend. This region is also classified as the 'surface' of the silicon and is known as the space charge region (SCR). The way in which recombination in the SCR is incorporated into the surface recombination velocity will be shown in the next section.

2.3.1 SPACE CHARGE REGION

The space charge region (SCR) may exist for several different reasons. It can be caused by a charge density at the surface of the silicon, from charge in or on the dielectric capping layer, by a metal contact with a different work function, an electric field or a doping profile. Regardless of the cause, the result is that the bands bend. The depth of the space charge region is considered to be the distance into the silicon until the point at which the bands are flat [87], defined by equation (2.16)

$$d_{SCR} = \sqrt{\frac{2\epsilon_0 \epsilon_r \emptyset_s}{qN_d}} \tag{2.16}$$

where $\emptyset_s$ is the surface voltage and N_d is the density of donor atoms.

Any recombination that occurs within this region is classified as surface recombination. Due to the silicon used, radiative and Auger recombination are generally insignificant. Therefore, recombination within the SCR is modelled by an extended SRH formalism developed by Girish et al [88].

2.3.2 Effective Surface Recombination Velocity

It is now appropriate to define the effective surface recombination velocity (S_{eff}). This is the sum of the ideal surface recombination velocity and the recombination occurring in the space charge region. However, it is not possible to measure the effective surface recombination velocity directly. Instead, the effective lifetime of the sample must be measured, and from this the S_{eff} can be inferred, provided that the bulk lifetime is known. The following section presents this method along with an approximation that will be used for calculations of this sort throughout the project.

2.4 Calculation of Effective SRV

As mentioned previously, the effective lifetime is controlled by recombination in both the bulk and at the surface, equation (2.4). Due to the quality of the wafers used in the present work, the SRH bulk lifetime can be assumed to be infinite, therefore the bulk lifetime can be calculated using Richter's parameterisation for Auger recombination, equation (2.8), and the radiative recombination coefficient, B, given by Altermatt. This leaves only the surface lifetime unknown which can be calculated by removing the bulk lifetime component from an effective lifetime measurement.

The methods discussed in the previous section enable the S_{eff} to be calculated, but do not provide a means to infer the S_{eff} from experimental measurement. This was addressed by Luke and Cheng [89] who simultaneously considered the spatial concentration of excited carriers as a function of time in their formalism. They found that S_{eff} is a function of many decaying carrier lifetime terms of which the lowest mode is dominant. This can then be written as:

$$\frac{1}{\tau_{eff}} = \frac{1}{\tau_b} + \alpha_1^2 D \tag{2.17}$$

where α_1 is defined as in equation (2.18) [17].

$$tan\left(\frac{\alpha_1 W}{2}\right) = \frac{S_{eff}}{\alpha_1 D} \tag{2.18}$$

By substituting equation (2.18) into equation (2.17), one can find S_{eff} using equation (2.19):

$$S_{eff} = \sqrt{D\left(\frac{1}{\tau_{eff}} - \frac{1}{\tau_b}\right)} tan\left(\frac{W}{2}\sqrt{\frac{1}{D}\left(\frac{1}{\tau_{eff}} - \frac{1}{\tau_b}\right)}\right) \tag{2.19}$$

where D is the ambipolar diffusion coefficient, with units of cm^2/s, [90] and W is the wafer thickness in cm. In order to calculate D, Klassen's mobility model [91] was employed using the online calculator of PV Lighthouse [92].

For low values of x, $tan(x) \rightarrow x$. Using this principle and equation (2.19), Sproul found that for values of the non-dimensional term $S_{eff}W/D < 0.25$, an approximation of $\tau_s \cong W/2S_{eff}$ was accurate to within 4% [93]. The wafers used in this project are 200 µm thick, and the diffusivity constant for holes has been calculated to be 13 cm/s. Therefore, for this approximation to be valid, the constraint $S_{eff} < 162$ cm/s must hold. This was the case for all samples used throughout this project. Incorporating Sproul's approximation gives a new effective lifetime definition of:

$$\frac{1}{\tau_{eff}} = \frac{1}{\tau_{rad}} + \frac{1}{\tau_{Aug}} + \frac{1}{\tau_{SRH}} + \frac{2S_{eff}}{W} \tag{2.20}$$

2.5 Surface Saturation Current Density

Another metric used to characterise surface recombination is the emitter saturation current density (J_{0e}). J_{0e} represents the loss due to recombination in the emitter and at the surface. However, in this work surface saturation current density (J_{0s}) values are quoted, as there is no emitter present. In recent work by McIntosh and Black [86], they report that J_{0s} is independent of doping concentration for the majority of practical conditions. For this reason, J_{0s} may even be considered to be a preferable metric for surface passivation than SRV. J_{0s} is defined by Kimmerle et al [90] as:

$$J_{0s}(\Delta n) = \frac{d}{d\Delta n}\left(\left(n_{i,eff}^{2}\right)\sqrt{D\left(\frac{1}{\tau_{eff}}-\frac{1}{\tau_b}\right)}\tan\left(\frac{W}{2}\sqrt{\frac{1}{D}\left(\frac{1}{\tau_{eff}}-\frac{1}{\tau_b}\right)}\right)\right) \quad (2.21)$$

In this thesis, J_{0s} has been calculated using a model developed by Bonilla [66] based on Mäckel and Verner's work [94], using an iterative algorithm, as proposed by Kimmerle et al [90]. The effective intrinsic concentration has been calculated using Pässler's model [95] implemented online by PV lighthouse [92]. The details of this process can be found in reference [66].

2.6 Interface Trap Theory

In Chapter 1, the density of interface traps at mid-gap, D_{it}, was used to characterise the quality of chemical passivation. However, this is a simplification of the interface properties: interface trap distribution throughout the bandgap and the capture cross-section of electrons and holes at each trap level. Firstly, interface traps are energy dependent and are not evenly

distributed throughout the bandgap. Instead, they are usually distributed with a greater number of states near the bands and a smaller number of deep trap levels, as shown in Figure 11 for a typical Si-SiO_2 interface.

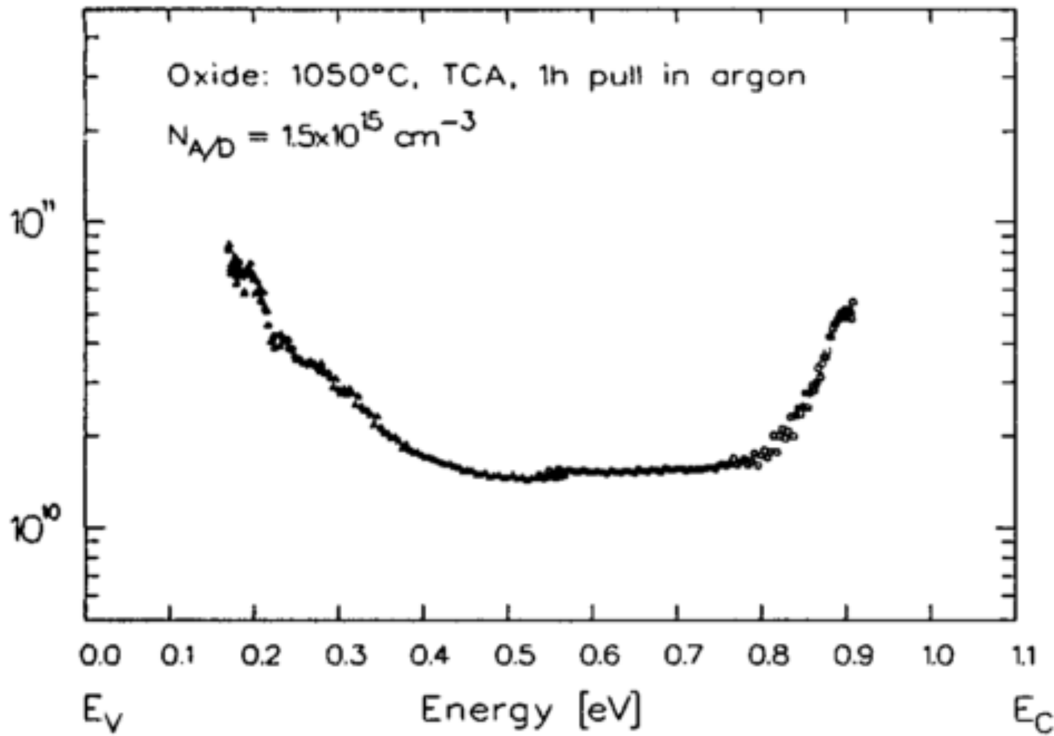

Figure 11. Energy dependent density of interface traps, typical of a thermally grown SiO_2-Si interface of 100 orientation. After [46]

Secondly, SRH statistics reveal that the effectiveness of a trap level as a recombination centre is not solely reliant on the number of traps at a given energy level but instead depends on the capture cross-section, σ, of a given trap. From equation (2.14) and (2.15) the surface recombination velocity can be re-written as:

$$S_0 = \frac{1}{\Delta n}(n_s p_s - n_i^2)\int_{E_v}^{E_c} \frac{1}{\frac{n_s + n_1(E)}{S_p(E)} + \frac{p_s + p_1(E)}{S_n(E)}}\, dE \qquad (2.22)$$

where

$$S_p(E) = v_{th} D_{it}(E) \sigma_p(E) \quad (2.23)$$

is the energy dependent recombination velocity for holes. An equivalent equation exists for electrons. By considering $S_p(E)$ and $S_n(E)$, it is clear that both the density of traps, D_{it}, and the capture cross-section of each trap, σ, play an important role in describing the effectiveness of a trap as a recombination centre. Over past decades, the energy-dependent capture cross-sections of traps at the Si-SiO_2 interface have been well studied. Aberle [46] compiled some of the published data for these capture cross-sections, shown in Figure 12.

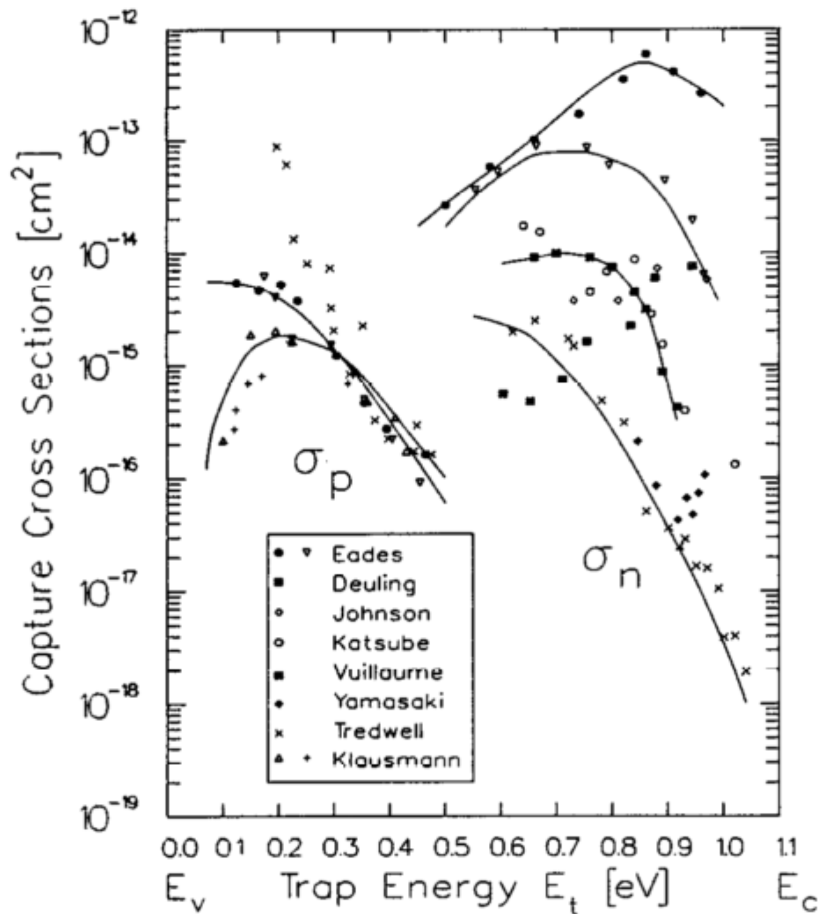

Figure 12. Energy dependent electron and hole capture cross-sections at the Si-SiO_2 interface. The solid lines represent guides to the eye. After [46]

The capture cross section for holes is generally lower than that for electrons with a ratio at an oxide surface of $\sigma_n/\sigma_p \approx 100$ at midgap [17], where the variation in experimental results is far reduced. The rate of recombination at a defect site is limited by the capture rate of the minority carrier. For n-type silicon, the minority carriers are holes, which have a smaller capture cross section and therefore lower capture rate than electrons. Thus, n-type Si-SiO_2 interfaces inherently have a lower SRV than p-type Si. This is further assisted by the positive polarity of the small intrinsic SiO_2 charge which acts to repel the hole minority carries from the interface. This explains more one of the reasons why n-type silicon is preferable to p-type for high lifetime Si PV devices. However, the difference is SRV is not as profound as the difference in capture cross-section. This is believed to be because the density of interface traps at the Si-SiO_2 interface is larger for n-type than p-type Si due to hydrogenation [96].

2.7 FIELD EFFECT PASSIVATION THEORY

Now, the impact of dielectric surface charge, or FEP, on surface recombination, S_{eff} must be considered. In order to model the effect of FEP, one must consider the chemical passivation of the surface and define the functions of $S_p(E)$ and $S_n(E)$ of equation (2.23). Bonilla et al. [97] define the Gaussian function of $S_{n/p}(E)$ with a maximum of $S_{0n/0p}$ at an energy of $E_{0n/0p}$ and a curvature of $a_{n/p}$. A model is proposed where S_{eff} is presented as a function of dielectric charge, dependent on the characteristics of $S_p(E)$ and $S_n(E)$, as in Figure 13. Bonilla then fit the model to experimental data to more accurately define $S_{n/p}(E)$ by using least-squares fitting.

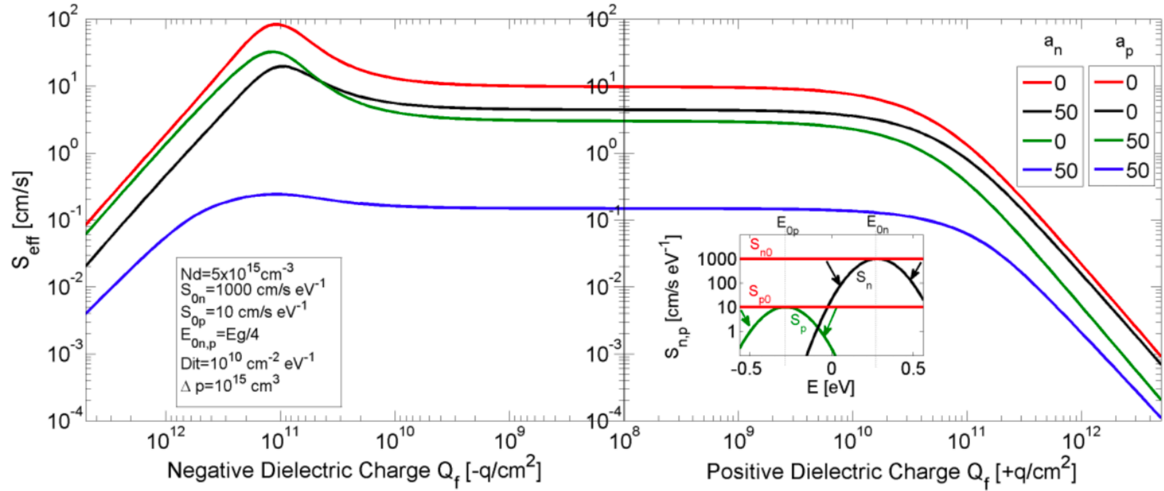

Figure 13 Surface recombination velocity for n-type silicon as a function of positive and negative dielectric fixed charge concentration in q/cm^2, for an excess minority carrier concentration of 10^{15} cm^{-3}, and a variation in the surface recombination of holes and electrons given by the curvatures a_n and a_p. Four combinations of a_n, a_p have been chosen as illustrated by the legend in the figure. Inset: Holes (green) and electrons (black) surface recombination functions used to calculate surface recombination velocity. Red horizontal lines represent the value the functions take when the dependence is eliminated ($a_{n/p}$= 0). After [98].

From Figure 13 it is evident that, regardless of the nature of the surface states as represented by $S_{n/p}(E)$, the dependence of S_{eff} on dielectric charge is significant for charge concentrations above 10^{11} q/cm^2, either positive or negative. When the charge concentration is less than this, S_{eff} is almost entirely independent of charge concentration except for at a charge concentration of -10^{11} q/cm^2 where the S_{eff} increases. This peak occurs when the band bending at the surface of the silicon is such that it maximises the carrier capture rate and $S_n n_s = S_p p_s$, leading to increased surface recombination. Within this work, surface charge concentrations of > 2 x 10^{12} q/cm^2 are sought as these concentrations appear to provide reductions in SRV that are suitable for high efficiency solar cell geographies [61, 97].

CHAPTER 3
EXPERIMENTAL METHODS

This chapter outlines both the experimental methods and the analysis techniques used throughout this thesis.

3.1 BASE SILICON

3.1.1 SUBSTRATES

Two types of mono-crystalline n-type silicon were used in this project. The one predominantly used was high purity, Float Zone (FZ) n-type silicon doped with phosphorus to a concentration of 5×10^{15} cm^{-3} giving a resistivity of 1 Ωcm. Additionally, a small quantity of phosphorous doped Czochralski (Cz) silicon of 30-40 Ωcm was used. These are summarised in Table II.

Table II Summary of silicon substrates used in this thesis

Ref.	Type	Dopant	Resistivity	Thickness	Source
Ox	n-type FZ	P	1 Ωcm	200 μm	Fraunhofer ISE
Z	n-type Cz	P	30 – 40 Ωcm	375 μm	Sun Edison
ANU	n-type FZ	P	1 Ωcm	195 μm	Australia National University

3.1.2 Surface Finish

Commercial silicon surfaces are textured to increase the probability of photon absorption. However, the silicon used in this project has a planar finish to aid characterisation and measurements. The FZ silicon was double side SEMI flat polished, and the Cz material was single side SEMI flat polished, back side alkaline etched.

However, the research used planar surfaces to facilitate characterisation. Textured silicon was not used during this project; however, it would be useful to apply the proposed processes to textured surfaces in future projects.

3.2 Dielectrics

In this work, thermal silicon dioxide was used as the dielectric.

3.2.1 Thermal Oxides Growth

Samples were dry thermally oxidised in three laboratories under different oxidation conditions which are summarised in Table III. In some instances, dichloroethylene (DCE) was used to enhance oxide growth.

Table III Summary of silicon oxidation processing of samples used in this project

Ref.	Atmosphere	Temperature	Location	Thickness
Ox	DCE/O_2	1050 °C Dry	Fraunhofer ISE	100 nm
Z	O_2, ramp down in N_2	1050 °C Dry	Oxford Cleanroom	100 nm
ANU	O_2, ramp down in N_2	1050 °C Dry	Australia National Univ.	140 nm

The purpose of this work was to investigate a process that could be implemented at large scale on thin thermal oxide layers that would form part of a dielectric stack. The SiO_2 layers described in Table III are considered thick compared to those used in industry and would be unsuitable due to the time required for growth. However, it was necessary to develop the process using oxides of this thickness because thinner oxides would limit the number of characterisation techniques accessible.

3.2.2 Optical Characterisation

In order to measure the thickness of the oxide, a Film Sense FS1 elipsometer was used. On a 100 nm silicon oxide, this equipment is reported to have an accuracy of 0.18 nm and a precision of ± 0.002 nm [99]. A refractive index of 3.9 was assumed for the silicon dioxide.

3.3 Metal Deposition

Metal depositions were conducted in several laboratories, using pieces of equipment of two types: e-beam and thermal evaporators.

3.3.1 Thermal Evaporation of metal

Thermal evaporation is achieved in a vacuum chamber by passing a high current through a tungsten filament or boat holding the metal for evaporation. Three thermal evaporators were utilised during this project, one in the Materials Department Cleanroom at the Begbroke Science Park, another in the group's main laboratory at Parks Road in Oxford, and the third in the Australia National University. The thermal evaporators in the cleanroom and at ANU were equipped with vibrational frequency thickness monitors, whereas depositions using the main laboratory evaporator were judged by the colour of the aluminium layer deposited. During the project, it became evident that the Cleanroom thermal evaporator was contaminated (albeit with extremely low concentrations of ionic species), which will be discussed in Chapter 4 and 5 of this thesis. On occasion, this contamination was found to interfere with experiments and in these instances either the Parks Road evaporator or Cleanroom e-beam evaporator were used.

3.3.2 E-beam Evaporation of metal

Evaporation using electron-beam (e-beam) is achieved by firing high energy electrons at the source metal, under vacuum. The energy from the electrons excites the metal atoms to evaporate and land on the exposed sample surface. Due to the presence of energetic particles, the process has been known to cause damage to the oxide-silicon interface and introduce trap states [37] which reduce carrier lifetime and complicate characterisation techniques. However, the trap states introduced by e-beam evaporation were found to anneal out rather effectively during a 25 minute anneal at 425 °C making e-beam another appropriate evaporation technique. E-beam evaporation was also carried out at Southampton University.

3.4 The Alneal

As mentioned in Chapter 1, the alneal process is one of the most effective techniques to reduce surface recombination at the oxide-silicon interface [100]. It is achieved by depositing aluminium onto the oxide surface and annealing the sample at 400 – 450 °C for 25 - 30 minutes before etching off the aluminium in heated phosphoric acid [64]. The passivation mechanisms behind this technique are analysed in this thesis. Alneals of oxidised silicon were carried out using evaporation equipment and furnaces in several different laboratories. Those done at ANU were conducted by Teng Kho, those at Oxford and Southampton were conducted by the author, with the generous assistance of Tasmiat Rahman in Southampton. These are summarised below. The Al etchant referred to comprised 60 % phosphoric, 2.5 % acetic, 3.5 % nitric acids and water.

Table IV Details of various alneal processing

Ref.	Al Evaporation			Anneal			Al Etch
	Location	Type	Purity	Location	Temperature	Atmosphere	
Ox	Cleanroom	Thermal	5n/6n	Parks Rd	400 – 450°C	Air or Argon	Al etchant @ ~ 50 °C
	Cleanroom	e-beam	5n				
	Parks Rd	Thermal	5n/6n				
ANU	ANU	Thermal	5n	ANU	425 °C	Forming Gas	Phosphoric Acid
Soton	Southampton	e-beam	5n	Parks Rd	400 – 450°C	Air	Al etchant @ ~ 50 °C

3.5 CORONA DISCHARGE

This technique is a remote method of extrinsically charging a dielectric surface to provide FEP. It is achieved by applying a large voltage, approximately 30 kV, to a pin which ionises molecules in the air. Depending on the polarity of the voltage applied, positive or negative, H_3O^+ or CO_3^- molecules [101–103], are deposited on the sample surface. A schematic of the corona discharge setup is shown in Figure 14.

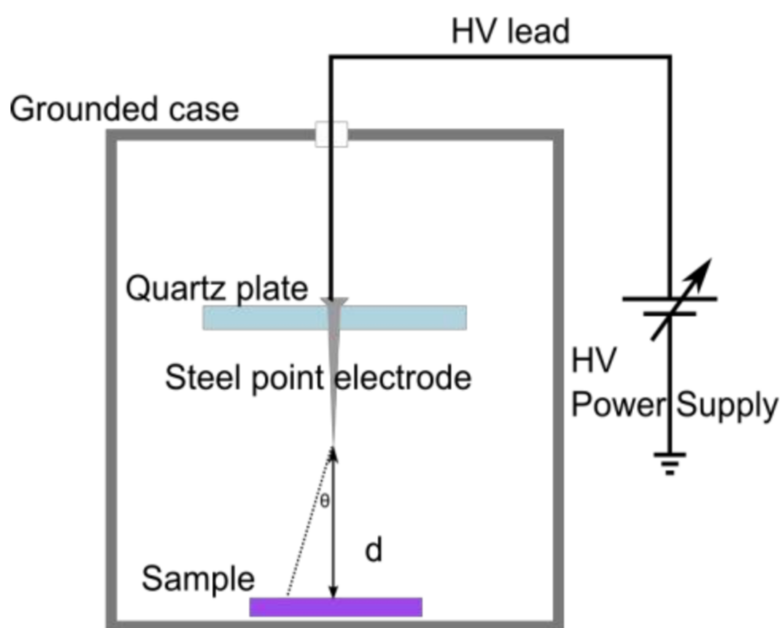

Figure 14. Corona Discharge apparatus. After [98]**.**

The uniformity of the charge distribution from the equipment used throughout this work was characterised by Woodcock and Bonilla [52, 104]. They measured surface potential using Kelvin Probe for a pin height of 15 cm above the sample. Their work showed that over a 3 x 3 cm^2 sample, the standard sample size for effective lifetime measurements, the charge deposited was within 5% of the measured average. In some of this work, a more recent corona discharge apparatus was used where the distance between sample and pin was 20 cm. This will have improved charge uniformity further and reduced the rate of charge deposition.

3.6 Ion Deposition

One of the aims of this project was to investigate the introduction of various positive ionic species in to the SiO_2 dielectric for the purpose of field-effect passivation. Previously, in work by Bonilla [61, 62, 98, 105], ionic precursors were deposited onto dielectric surfaces by thermal evaporation as suggested in work by Eldridge and Kerr [106]. After this, ions could be migrated using various processing techniques.

In order for ions to be available for migration, the formation of salt crystals on the oxide surface must be avoided. This is because the presence of salt crystals is believed to prevent the introduction of the ionic species in to the oxide layer. A uniform sub-monolayer concentration of ions is therefore desirable. This means that droplet formation during solution drying, after deposition, must be avoided. Positive ionic species were introduced from chloride salts using the following techniques: namely thermal evaporation, spin coating and spray pyrolysis.

3.6.1 Thermal Evaporation of Salts

Salts were deposited in the thermal evaporator in the Cleanroom at Begbroke. To do this, a 50 μL droplet of aqueous salt solution was pipetted onto a tungsten evaporation boat. This boat was then heated on a hot plate to allow the water to evaporate. The boat was then ready to be mounted in the thermal evaporator and a high current (30-50 A) passed through the boat until it was seen to glow white several times through the viewing pane. No shutter was used during this evaporation process, and the thickness monitor was redundant as concentrations were below the detection limit.

The concentration of the 50 μL aqueous salt solution was determined by the concentration of ionic species required on the sample surface. By assuming that the evaporated salt would

cover a hemisphere and knowing the distance of the sample holder from the evaporation source, r, it is possible to deduce the number of salt molecules necessary in the tungsten boat, Σ, in order to achieve a surface ion concentration, σ, using:

$$\Sigma = \sigma(2\pi r^2) \tag{3. 1}$$

Once the number of salt molecules was known, the mass of the salt, M_{salt}, to be dissolved in a given volume of water, V_{sol}, could be determined as:

$$M_{salt} = \frac{V_{sol}}{V_{boat}} \frac{\rho_{salt}}{N_{AVG}} \Sigma \tag{3. 2}$$

where ρ_{salt} is the mass per mol of the salt, N_{AVG} is Avogadro's constant and V_{boat} is the volume of the solution to be added to the tungsten boat.

In this project, the solution concentration was calculated to provide a surface ion concentration of 10^{14} ions/cm^2 unless stated otherwise.

3.6.2 SPIN COATING

Spin coating is a technique widely used in industry to deposit uniform layers of liquids onto substrates. In order to avoid droplets of solution forming on the surface during the drying process, it is necessary to use a solvent which wets the oxide surface effectively. For this work a solvent of 75% IPA and 25% de-ionised (DI) water was used as IPA both wets the oxide and evaporates quickly at room temperature. The water is required as the salts do not have a high enough solubility in pure IPA.

Using a pipette, 1 – 2 ml of solution were deposited on the sample surface once the spin coater had reached a speed of 2000 rpm. The process length was set to 2 minutes. The

parameters of spin coating for the deposition were investigated by Siyao Du as a component of her Part II project for her M.Eng in Materials Science [107].

3.6.3 SPRAY PYROLYSIS

During the period of this project, the Semiconductor lab did not have spray pyrolysis equipment. Instead, spray coating was conducted at USI, Haverhill MA, using their PRISM bench-top ultrasound coating system. A solution of 3×10^{-4} mol/L KCl dissolved in 10% H_2O and 90% IPA was used to give an 11 µm thick layer. This was predicted to give a surface ionic concentration of 10^{14} ions/cm^2.

3.7 ION MIGRATION PROCESSES

Once the ionic precursor was deposited on the surface, it was necessary to drive the ions into the oxide. This was done using annealing, thermally stimulated ionic conduction (heating with a bias applied using a metal electrode) and field-assisted ionic migration. All three processes are described.

3.7.1 ANNEALING

Anneals were conducted in tube furnaces or on a hotplate as described below.

3.7.1.1 TUBE FURNACE

When a tube furnace was used, the anneal could be carried out under an argon or air atmosphere. The quartz tube was retracted from the furnace casing and samples were placed inside the tubing using ceramic tweezers and then pushed into the centre of the tube using a quartz rod. A thermocouple inside a quartz sleeve was used to monitor the temperature at the centre of the furnace. Samples were retrieved at the appropriate time using the quartz

rod, which had a hooked end, and removed from the furnace tube using ceramic tweezers. Samples were held in the ceramic tweezers until cool, which would take 2-5 seconds.

3.7.1.2 Hot Plate

When a hot plate was used, to reduce contamination and support experiments at higher temperatures, a borosilicate glass petri-dish with a lid was placed on top of the hotplate. This allowed the atmosphere inside the petri-dish to reach a higher temperature than if the sample was placed straight on to the hotplate. With the lid in place, the temperature inside the petri-dish was measured using a thermocouple. When placing the sample inside the petri dish, the lid was quickly removed causing a decrease in temperature, which recovered within ~ 5 seconds. At 450 ˚C, the reduction in temperature was ~ 10 ˚C. During anneals over one minute, due to the quick recovery in temperature, this is not significant. However, during shorter anneals this may be significant. In addition, for very short anneals the time taken for the specimen temperature to increase will also be substantial compared to the total anneal time. Thus, for anneals of a few seconds, the actual temperature of the specimen during the anneal is likely to have been lower than the temperature quoted.

3.7.2 Thermally Stimulated Ionic Conduction

Thermally Stimulated Ionic Conduction (TSIC) measurements were used to quantify the concentration of ions that migrate across the oxide at elevated temperature under an external bias. For these measurements, a metal-oxide-silicon (MOS) structure was required. The metal front contact and silicon then act as electrodes between which a voltage can be applied. This results in a voltage drop across the MOS, which can be applied at elevated temperature in air ambient. The current between the two electrodes is monitored while the voltage is applied by use of a source measure unit (SMU). This enables the migration of ions across the MOS structure which produce an electrical current that is recorded. TSIC experiments

allow the magnitude of this current to be characterised as a function of temperature, applied bias and time. The set-up is shown in Figure 15. For these experiments, MOS capacitor samples were prepared by removing the back oxide using HF and evaporating aluminium onto scratched, bare silicon to create an ohmic back contact. The front contact was created by evaporating a metal dot of 2 mm diameter through a contact mask onto the SiO_2. A voltage was applied between the silicon bulk and the top metal dot while the sample was on the TSIC hotplate. The voltage continued to be applied as the sample cooled, to minimise diffusion of the ions back to their original position. The current between the contacts was recorded using LabVIEW. This current reading could then be integrated, with respect to time, and used to calculate the movement of charge between the two electrodes, denoted as Q_{ion} in Figure 15 (b).

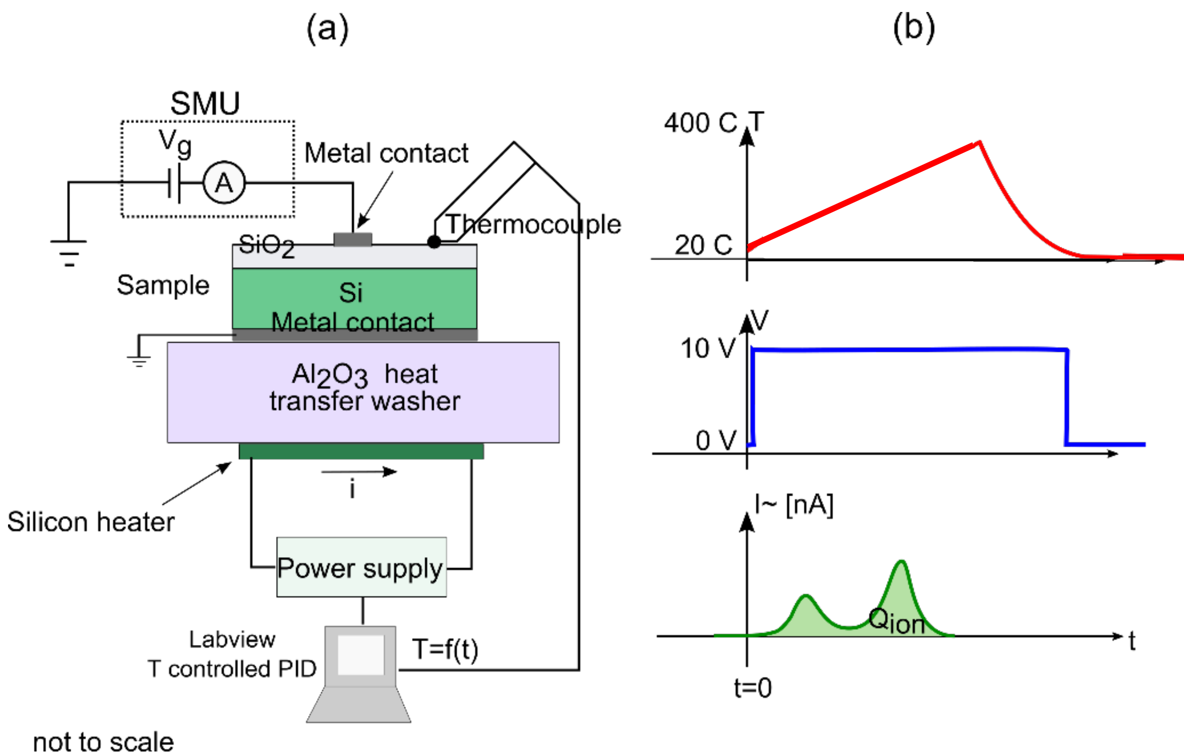

Figure 15 Thermally Stimulated Ionic Conduction (TSIC) (a) schematic and (b) typically measured parameters during processing. After [108]**.**

For the temperatures used, and with the voltages applied, other current mechanisms were found to be under 4 x 10^{11} q/cm^2 with 1 V applied, increasing to 9 x 10^{11} q/cm^2 with 5 V applied [109]. Thus, in this work, the measured current is approximated to be due entirely to the migration of ionic charge through the MOS structure, and the charge concentration calculated from the integral of the current is taken to be equivalent to the charge migrated to the SiO_2-Si interface. In addition, Capacitance-Voltage (CV) measurements of the SiO_2-Si interface charge (to be discussed in section 3.8.2) were taken of the samples after TSIC processing as an independent measurement.

The hot plate was also used for anneals of some small samples, under an air ambient. The temperature of the hotplate was monitored and controlled via a LabVIEW software. A K- type thermocouple, placed next to the sample, measured the temperature. This was recorded by the LabVIEW software and controlled via a PID using the thermocouple as the sensing element.

3.7.3 FIELD-ASSISTED IONIC MIGRATION

TSIC is a useful technique to improve understanding of the introduction and transport mechanisms of ions in SiO_2 from an Al-SiO_2 interface. However, it is only suitable on small areas under an MOS top contact due to pin holes that can exist in the SiO_2 and is not a commercial method. An alternative is to use corona as the driving force for ion migration.

To do this, corona charge is deposited using ± 30 kV from the apparatus described in section 3.5. The sample is then annealed on a hotplate, inside a petri-dish, to assist migration.

3.8 Characterisation Techniques

Several characterisation techniques were utilised during the course of this thesis. They were Photoconductance decay lifetime measurements, capacitance-voltage, Kelvin probe, and two methods to characterise the density of interface traps.

3.8.1 Photoconductance Decay Lifetime

Sinton photo-conductance decay (PCD) measurements were taken using a WCT-120 model, with samples at 25 °C, to calculate the effective lifetime of minority carriers in the silicon specimens. Measurements are taken over a range of injection levels, however it is convention to quote lifetime values at a minority carrier injection level of 10^{15} cm^{-3}. An error analysis study of this equipment was conducted with 24 participants across multiple laboratories. For transient mode, which is the equipment mode used throughout the project, the error was found to be within ±8% between the laboratories [110].

Once an effective lifetime measurement has been made, it is common to convert this into a surface recombination velocity (SRV) using equation (2.19). This parameter is useful when discussing surface passivation as, unlike lifetime results, it is independent of sample thickness. Details of these calculations are given in Chapter 2, section 2.4.

3.8.2 Capacitance-Voltage

Capacitance-Voltage (CV) is a well-established technique to determine charge concentration at the dielectric-silicon interface. It requires a metal-oxide-semiconductor (MOS) structure where the metal and the semiconductor act as two electrodes between which a voltage can be applied. In this work, the CV measurements can be taken in two ways. Either the metal is evaporated onto the surface and a probe station is used to contact the top metal dot, or, a

less permanent measurements can be made using mercury to form the top electrode. The mercury probe, or Hg-CV probe as it is referred to, is depicted in Figure 16.

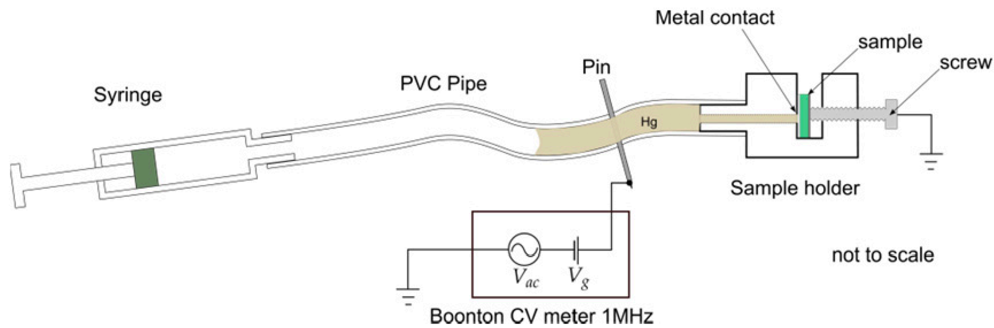

Figure 16 Schematic of Hg-CV probe. After [98]**.**

By varying this voltage, the surface band bending is modified, resulting in a space charge region at the silicon surface. The space charge region acts as a capacitor, C_{scr}, in series with the oxide capacitor, C_{ox}, while interface trap states, C_{it}, are represented by a capacitor in parallel to the depletion region as shown in Figure 17 (a).

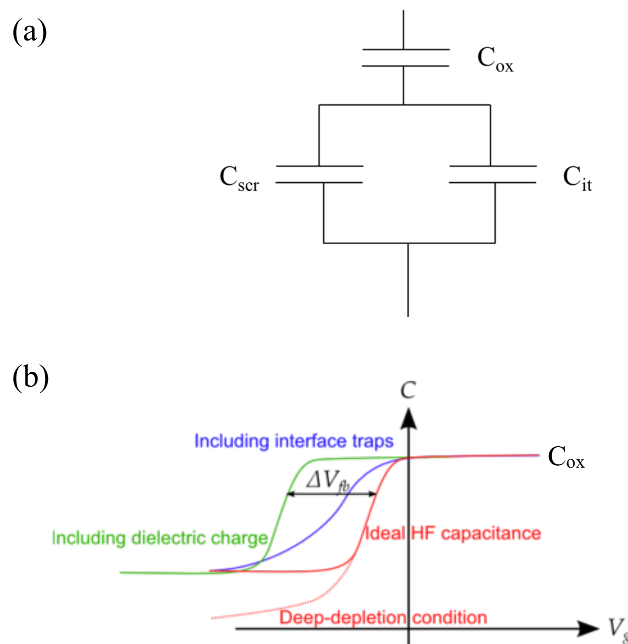

Figure 17 Schematic to demonstrate (a) equivalent circuit used in CV measurement analysis and (b) a representation of a CV curve showing ideal conditions (red), deep depletion (orange), including interface charge (green) and with interface states (blue). After [98]**.**

As a result of the quality of the interface between a thermal oxide and silicon layer, the number of interface traps and therefore the capacitance due to such traps is deemed negligible in the majority of this work. This results in an equivalent circuit where the total measured capacitance, C_{meas}, is:

$$C_{meas} = \frac{C_{scr}C_{ox}}{C_{scr} + C_{ox}} \quad (3.\ 3)$$

The oxide capacitance can be calculated using:

$$C_{ox} = \varepsilon_{ox}\varepsilon_0 \frac{t_{ox}}{A} \quad (3.\ 4)$$

where t_{ox} is the oxide thickness and A is the area of the MOS capacitor. However, as the area of the dot is often not well defined, the oxide capacitance is determined experimentally by the measured capacitance when the silicon surface is in accumulation and $C_{meas} = C_{ox}$, i.e. the maximum capacitance measured.

The conditions under which the interface charge is fully compensated by the applied voltage results in the bands within the silicon being flat, as shown in Figure 18 (b), where E_C and E_V are the conduction and valence band levels, E_i is the intrinsic energy level, E_F is the Fermi level, Φ_s is the silicon work function, Φ_m is the metal work function, $\Phi_{ms} = -\Phi_{sm}$ and is the work function difference between the silicon and the metal, V_{ox} is the voltage drop across the oxide and q is the elementary charge. The reader must not that upper case Φ is used to represent work function energy difference in eV, while lower case ϕ is used to represent voltage.

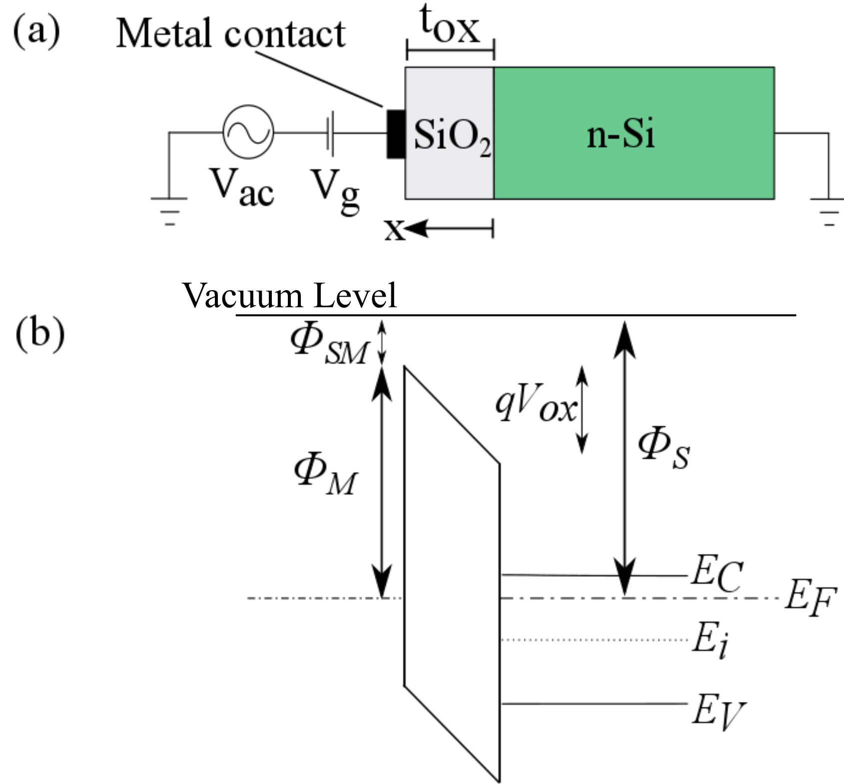

Figure 18. (a) Schematic of the CV set up, (b) band diagram for flatband conditions assuming all charge located at the SiO_2-Si interface.

The flat band capacitance within the silicon, C_{fb}, is calculated using the Debye length, L_d, and the permittivity of the silicon, ε_S, [71] as:

$$C_{fb} = \frac{\varepsilon_S}{L_d} = \frac{\varepsilon_S}{\sqrt{\frac{\varepsilon_S kT}{q^2|N_d|}}} \quad (3.\ 5)$$

This flatband silicon capacitance can be used in conjunction with the oxide capacitance to determine the total capacitance measured under these conditions using equation (3. 3). The calculated total capacitance at flatband can then be substituted into equation (3. 3) to find the total capacitance at which flatband occurred. The experimental voltage applied to achieve this capacitance can then be found and is defined at the flatband voltage, V_{fb}.

Once the flatband voltage has been determined, this is used to calculate the interface charge density. For CV measurements, it is well known that the voltage across the MOS structure, V_{MOS}, is given by [111]:

$$V_{MOS} = V_{\Delta wf} - \phi_{scr} - V_{interface} - V_{ox} \tag{3. 6}$$

$$V_{MOS} = \frac{\Phi_{ms}}{q} - \phi_{scr} - \frac{Q_{it}(\phi_{scr})t_{ox}}{\varepsilon_{ox}\varepsilon_0} - V_{ox} \tag{3. 7}$$

where Φ_{ms} is the metal to semiconductor work-function difference ($\Phi_{ms} = -\Phi_{sm}$), ϕ_{scr} is the potential difference between the bulk and the surface of the semiconductor due to the space charge region, and V_{ox} is the potential drop in the oxide, including the interface to the metal but without including the semiconductor-interface trapped charge, Q_{it}. Interface trapped charge develops due to ionized acceptor and donor states at the SiO_2-Si interface and is dependent on the semiconductor surface potential, ϕ_{scr}. This leads to the widely known expression for flatband ($\phi_{scr} = 0$) voltage in CV measurements [112]:

$$V_{fb} = \frac{\Phi_{ms}}{q} - \frac{Q_{it}(\phi_{scr} = 0)t_{ox}}{\varepsilon_{ox}\varepsilon_0} - \frac{1}{\varepsilon_{ox}\varepsilon_0}\int_0^{t_{ox}} x\rho_{ox}(x)dx \tag{3. 8}$$

where $\rho_{ox}(x)$ is the volumetric charge distribution in the insulator. It is often assumed that the insulator charge is a single sheet of charge concentration Q_{ox}, given in units of C/cm^2, at a distance x_c from the insulator-silicon interface. The volumetric charge ρ can be expressed as a delta Dirac function centered at $t_{ox} - x_c$: $\rho(x) = Q_{ox}\,\delta(x - [t_{ox} - x_c])$. In this case, the potential difference due to insulator charge is $Q_{ox}(t_{ox} - x_c)/\varepsilon_{ox}\varepsilon_0$ and the flatband voltage becomes:

$$V_{fb} = \frac{\Phi_{ms}}{q} - \frac{Q_{it}(\phi_{scr} = 0)t_{ox}}{\varepsilon_{ox}\varepsilon_0} - \frac{Q_{ox}(t_{ox} - x_c)}{\varepsilon_{ox}\varepsilon_0} \quad (3.\ 9)$$

when the flatband voltage is found in CV measurements, the inferred charge is commonly calculated as:

$$Q_{CV} = \frac{\varepsilon_{ox}\varepsilon_0}{t_{ox} - x_c}\left(\frac{\Phi_{msCV}}{q} - V_{fb} - \frac{Q_{it}(\phi_{scr} = 0)t_{ox}}{\varepsilon_{ox}\varepsilon_0}\right) \quad (3.\ 10)$$

where the subscript 'CV' has been added to Φ_{ms} to indicate the work function difference for the CV measurement, which is different to that for a Kelvin Probe measurement. This indicates that CV V_{fb} measurements are more sensitive to charge that is closer to the insulator-silicon interface than to the metal-insulator interface. So V_{fb} is larger when the charge resides at the insulator-silicon interface, $x_c = 0$.

In this thesis, interface trap charge is not considered in CV and KP calculations. The mid-gap state density at the oxide-silicon interface is generally below 10^{12} eV^{-1}cm^{-2} [102]. It is those states between the Fermi level and intrinsic Fermi level that have the greatest probability of being in the charged state and contributing to Q_{it}. For the work presented $E_F - E_i = 0.34$ eV. Therefore, the number of states likely to contribute to Q_{it} if in the charged state is 3.4 x 10^{11} cm^{-2}. Assuming that only ~ 10^{11} cm^{-2} of these near mid-gap states are charged, the potential contribution of the ionized interface states could be a maximum of ~ 0.5 V. This is neglected in the calculations and equation (3. 9) is simplified to:

$$V_{fb} = -\frac{\Phi_{smCV}}{q} - \frac{Q_{ox}(t_{ox} - x_c)}{\varepsilon_{ox}\varepsilon_0} \quad (3.\ 11)$$

The error for the equipment used in this project was characterized by Rands [113] and found to be ± 0.1 x 10^{12} q/cm^2, this is generally less than a 10 % error. The main source of error is systematic and therefore does not influence the relative increase in measurement. The error derived by Rands is considered to be conservative. Therefore error bars are not included in most instances.

3.8.3 KELVIN PROBE

The Kelvin probe technique is a non-contact method to measure the dielectric surface potential of the top of the silicon substrate from which the surface charge concentration can be calculated. A schematic of the setup is shown in Figure 19 (a) along with a typical band diagram shown in Figure 19 (b). ϕ_{scr} is the voltage drop across the space charge region.

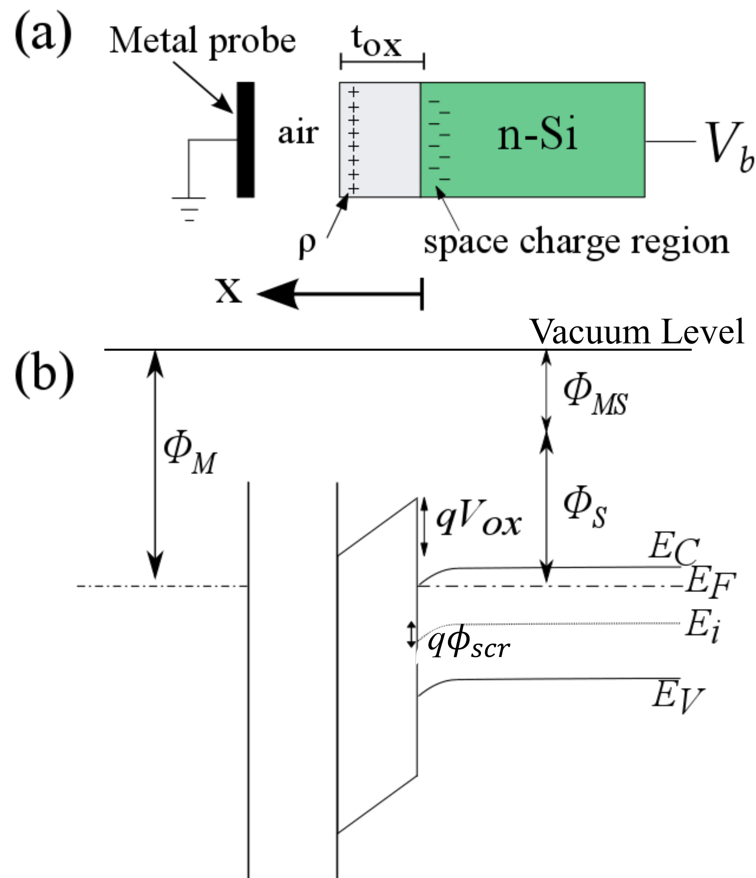

Figure 19. (a) Schematic of the Kelvin probe set up and (b) typical band diagram, with all charge located at the SiO_2 surface

This creates a capacitor where the silicon substrate and the metal pin are the two electrodes with the dielectric and air acting as the insulators. The top metal probe is programmed to vibrate, varying the distance between the pin and the dielectric surface. As a result, the capacitance varies, which induces a backing current, i_b.

$$i_b = \frac{dC}{dt} V_b \tag{3. 12}$$

where dC/dt is the change in the capacitance with time and V_b is the backing potential applied to the silicon substrate, which is used to calculate the voltage of the surface charge on the oxide. The point at which the backing potential equals the surface potential will result in zero current flow. In order to determine the voltage at which this occurs, Baikie's method [114] is employed whereby the applied backing voltage is varied and the current recorded. The current vs voltage data can then be interpolated to find the backing potential at which the current would be zero. The backing potential at which this occurs, V_{bKP}, is the opposite polarity to the dielectric surface potential, V_{surf}.

As the backing potential is defined as the external potential that must be established to equalize the potential of the pin and the semiconductor. The KP backing potential is therefore:

$$V_{bKP} = -(V_{\Delta wf} + \phi_{scr} + V_{surf} + V_i) \tag{3. 13}$$

The difference in polarity indicates that V_{bKP} compensates the other voltages to ensure the overall potential difference is zero. $V_{\Delta wf}$ represents the semiconductor to metal work function difference, V_{surf}. Is the dielectric surface potential, and V_i is the voltage due to charge throughout the insulator and includes the air gap:

$$V_i = \frac{1}{\varepsilon_{ox}\varepsilon_0}\int_0^{t_{ox}} x\rho_{ox}(x)dx + \frac{1}{\varepsilon_0}\int_{t_{ox}}^{t_{ox}+t_{air}} x\rho_{air}(x)dx \tag{3. 14}$$

where ρ_{air} is the volumetric charge concentration in the air relative to the distance from the SiO_2-Si interface. However, a sufficiently well isolated KP instrument will produce measurements where no charge concentration exists in the air, thus the insulator potential reduces to:

$$V_i = \frac{1}{\varepsilon_{ox}\varepsilon_0}\int_0^{t_{ox}} x\rho_{ox}(x)dx \tag{3. 15}$$

Once again, it can be assumed that all charge resides in a plane of concentration Q_{ox} at a distance x_c from the insulator-silicon interface. Therefore $\rho_{ox} = Q_{ox}\,\delta(x - x_c)$. Substituting this charge profile into equation (3. 15), the backing potential and the measured charge are given by:

$$V_{bKP} = \frac{\Phi_{smKP}}{q} - \phi_{scr} - \frac{Q_{it}(\phi_{scr})t_{ox}}{\varepsilon_{ox}\varepsilon_0} - \frac{Q_{ox}x_c}{\varepsilon_{ox}\varepsilon_0} \tag{3. 16}$$

$$Q_{KP} = \frac{\varepsilon_{ox}\varepsilon_0}{x_c}\left(\frac{\Phi_{smKP}}{q} - V_{bKP} - \phi_{scr} - \frac{Q_{it}(\phi_{scr})t_{ox}}{\varepsilon_{ox}\varepsilon_0}\right) \tag{3. 17}$$

where the subscript 'KP' has been added to Φ_{sm} to indicate the work function difference for the KP measurement. This calculation shows that KP measurements are more sensitive to charge at the air-insulator interface than the insulator-silicon interface. V_{bKP} is larger when $x_c = t_{ox}$.

Again, Q_{it} is neglected. Calculating ϕ_{scr} has been a well-known difficulty. Fortunately, theoretical solutions for ϕ_{scr} have been deduced [115, 116]. These can be used to demonstrate that a charge concentration in the space charge region in excess of 10^{13} q/cm^2 is necessary to produce a semiconductor surface potential $|\phi_{scr}| > 0.25$ V, on 1 Ωcm n-type silicon, using Boltzmann statistics. The accuracy of the KP instrument used here is ~ 0.4 V, thus ϕ_{scr} can be neglected from the calculation in equation (3. 16). The backing potential is now calculated as:

$$V_{bKP} = -\frac{\Phi_{msKP}}{q} - \frac{Q_{ox}x_c}{\varepsilon_{\text{ox}}\varepsilon_0} \tag{3. 18}$$

The error for this equipment was again characterised by Rands [113] and found to be ± 0.2 x 10^{12} q/cm^2. For the samples where the surface charge has a significant affect, this error is less than 10 %. The main source of error is systematic and therefore does not influence the relative increase in measurement. The error derived by Rands is considered to be conservative. For these reasons, errror bars are generally not included.

3.8.4 SIMS

Secondary ion Mass Spectroscopy (SIMS) was conducted by Aystorm Scientific. The analysis was carried out using a Magnetic Sector Spectrometer Cameca IMS 6F. A primary beam of O^{2+} ions, at an impact energy of 2 keV, which was scanned over an area of 180 µm x 180 µm. Calibration of the various elements was carried out using ion implanted reference materials in SiO_2. The depth was measured using a surface profilometer.

3.8.5 Density of Interface Traps

Although the quality of the chemical passivation can be inferred from lifetime measurements on samples that have high quality FEP, it is useful to be able to measure the interface trap density using a more direct method.

As discussed in Chapter 2, chemical passivation can be quantified by the density of interface traps, and the relative capture cross-sections of such traps. The density of traps varies across the band-gap making it an energy-dependent quantity with units $eV^{-1}cm^{-2}$. It is convention to quote the density of interface states at mid-gap as this is where the most effective recombination traps lie. Two techniques, the Terman method and the Conductance technique, are employed during this work to obtain D_{it} values, both of these are described below.

3.8.5.1 Terman Method

The Terman method [117] uses high frequency CV data to calculate D_{it}. However, this technique is known to be relatively inaccurate, usually under-estimating the density of interface traps and therefore only approximating the true value [111].

As mentioned in section 3.8.2, the capacitance measured during a CV sweep includes a capacitance term due to interface traps, C_{it}, defined as [71]:

$$C_{it} = \frac{dQ_{it}}{d\phi_s} = q^2 D_{it} \tag{3. 19}$$

where ϕ_s is the surface potential of the silicon. The relationship between the silicon surface potential and gate voltage is a voltage divider:

$$\frac{d\phi_s}{dV_g} = \frac{C_{ox}}{C_{ox} + (C_{scr} + C_{it})} \quad (3.\ 20)$$

where C_{scr} is the capacitance of the space charge region. By substituting equation (3. 19) into (3. 20), and solving for D_{it} [112]:

$$D_{it} = \frac{C_{ox}}{q^2}\left[\left(\frac{d\phi_s}{dV_g}\right)^{-1} - 1\right] - \frac{C_{scr}}{q^2} \quad (3.\ 21)$$

The relationship $d\phi_s/dV_g$ is found by comparing the measured CV curve with an ideal CV curve. Knowing that a given silicon surface potential, ϕ_s, would result in a certain ideal capacitance allows the measured V_g at the same capacitance to be compared to ϕ_s. The remaining term is C_{scr}, which is calculated from the measured capacitance and equation (3. 3), which assumes no interface trap capacitance because the ac frequency is too high for the interface traps to respond. This analysis was implemented using a Matlab script written by Bonilla [98].

3.8.5.2 CONDUCTANCE METHOD

The conductance method operates by measuring the conductance variation across a MOS structure caused by the application of a DC voltage with a small AC voltage fluctuating at different frequencies. The conductance of the MOS structure changes due to energy losses caused by charge transfer between interface traps and the silicon. The theory is thoroughly explained by Nicollian and Goetzberger [111, 118, 119].

To model the system for a single interface state, an equivalent circuit can be utilised, as in Figure 20.

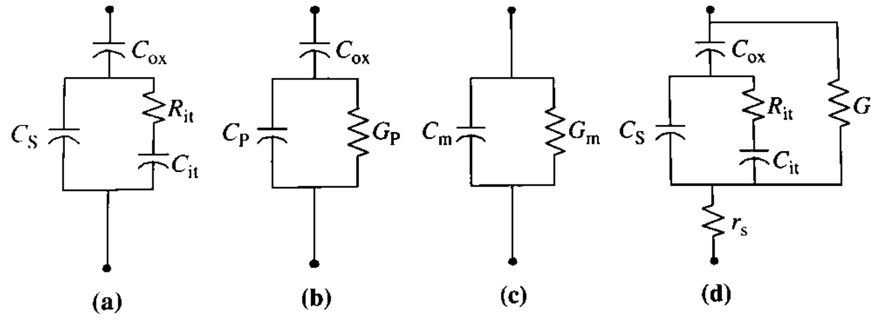

Figure 20. Equivalent circuit for conductance measurements (a) MOS structure, (b) simplified version of (a), (c) measured circuit and (d) including series resistance and tunnel conductance. After [112]**.**

For convenience, the equivalent circuit in (a) is simplified to that shown in (b) as:

$$C_P = C_S + \frac{C_{it}}{1 + \omega^2 \tau_{it}^2} \quad (3.\ 22)$$

where C_S is the capacitance of the silicon, referred to as C_{scr} in the majority of this work. C_{it} is the capacitance of the interface traps, τ_{it} is the time constant of the interface traps (τ_{it}=$R_{it}C_{it}$), and ω is the frequency.

The conductance is normalised with respect to frequency, which makes it symmetrical in $\omega\tau_{it}$, and the plotted curve easier to analyse:

$$\frac{G_P}{\omega} = \frac{C_{it}\omega\tau_{it}}{1 + \omega^2 \tau_{it}^2} \quad (3.\ 23)$$

Equations (3. 22) and (3. 23) are for the case for a single energy state. However, the surface is a continuum of states and equation (3. 23) must be integrated over the region for which the conductance peaks, which is approximately a width of kT/q centred about the Fermi level [118]. If the density of interface states, D_{it}, and capture probability can be assumed not to vary with surface potential across this energy range, which is usually appropriate [118], then the normalised parallel conductance for a continuum of states is shown to be:

$$\frac{G_P}{\omega} = \frac{qD_{it}}{2\omega\tau_{it}} ln(1 + \omega^2\tau_{it}^2) \quad (3.24)$$

The normalised equivalent parallel conductance G_P/ω can be plotted as a function of angular frequency, ω as in Figure 21. The position of the peak of this curve relative to the x-axis is used to calculate the average time constant of the interface traps, τ_{it}, which is related to the majority capture cross-section of the trap, σ. The area under the curve is proportional to the density of states, D_{it}. The theoretical model for both single and continuum levels along with experimental data are shown in Figure 21 from Schroder [112], p.348, using experimental data from [120].

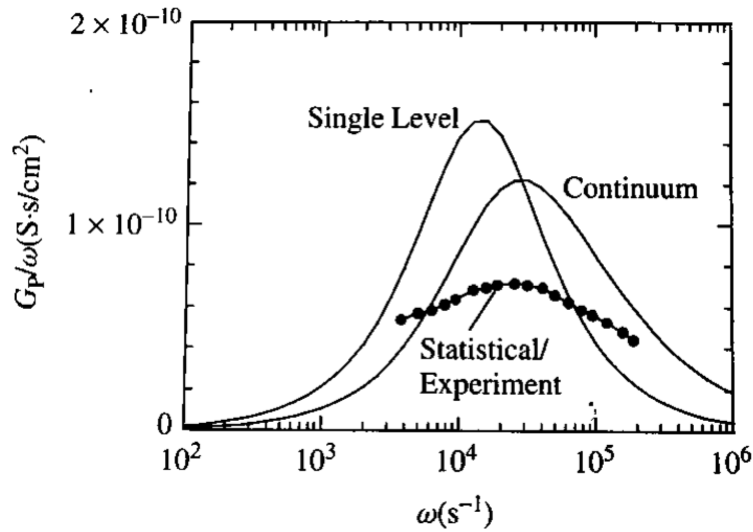

Figure 21. G_P/ω against ω for a single level, a continuum and experiments data. For all curves D_{it} = 1.9 x 10^9 $eV^{-1}cm^{-2}$, τ_{it} = 7 × 10^{-5} s. After [112].

In depletion, the conductance is normalised using the measured oxide capacitance, C_{ox}, measured parallel conductance, G_m, and measured capacitance, C_m, as:

$$\frac{G_P}{\omega} = \frac{\omega C_{ox}^2 G_m}{G_m^2 + \omega^2(C_{ox} - C_m)^2} \quad (3.25)$$

G_P/ω is then plotted against frequency as in Figure 21 and fitted with a theoretical model as in equation (3. 24). Matlab code created by Bonilla [98] was used for analysis. The theoretical curve parameters are optimised using the least-squares method to provide a good fit between theoretical and measured data.

The advantage of using the conductance instead of the capacitance D_{it} measurement technique is that it is not necessary to know the capacitance of the silicon space charge region, C_{scr}. This requires the doping concentration in the band bent region at the silicon surface to be known accurately, which is not always possible [121]. The conductance method is considerably more accurate, as the measure of parallel conductance depends directly on the interface properties.

CHAPTER 4
ENHANCING ALNEAL PASSIVATION

In the previous chapters, the motivation for this research was discussed along with the necessary background science and a summary of experimental procedures. In the following results chapters, it is important to bear in mind the different types of surface passivation: chemical and field effect. The primary aim of this work is to develop excellent extrinsic field effect passivation that allows passivation to be decoupled from the dielectric deposition parameters. As a starting point, one of the most effective passivation techniques, the alneal, was investigated to better understand the mechanisms by which it achieves such outstanding passivation. In this chapter, alneal samples from different laboratories are compared, the surrounding literature is reviewed in detail and the type of passivation present in two different sets of alneal samples is analysed.

4.1 LIFETIMES ACHIEVED USING THE ALNEAL

The alneal process is investigated because of its ability to provide one of the most recombination inactive Si-SiO_2 interfaces [64, 66, 79]. In the literature, the highest quality alneal is reported to achieve a SRV of 1.7 cm/s, equivalent to a J_{0s} of 1.1 fA/cm^2 [66] on 1.5 Ωcm n-type Si [64, 66]. In general, papers report values for SRV of 3 – 20 cm/s on both n-type and p-type c-Si ~1 Ωcm [122–124]. This shows a substantial reduction in the recombination activity of the interface compared to an as-grown Si-SiO_2 interface where a typical SRV on n-type 1 Ωcm Si would be between 50 to 150 cm/s [125, 126].

To investigate the passivation of the alneal, specimens were prepared at two laboratories, University of Oxford and Australian National University (ANU). The processing is described in Chapter 3 and below. It was largely comparable.

Samples prepared at Oxford University used 1 Ωcm, 200 µm, n-type FZ 4″ wafers which were oxidised at Fraunhofer ISE. These were cleaved into ¼ wafers before 70 - 100 nm of 99.999% purity aluminium was thermally evaporated onto both sides. The evaporation was done in the Department of Materials Cleanroom at Begbroke using a tungsten filament. Samples were alnealed under standard laboratory conditions inside a new borosilicate glass petri dish, which had been cleaned using IPA, and placed on a hot plate in air ambient at 425 ˚C for 25 minutes. After the alneal, the aluminium was etched off using commercial aluminium etchant (phosphoric acid 60 %, acetic acid 3.5 %, nitric acid 2.5 %, water). These samples are referred to as enhanced alneal samples for reasons that will become apparent.

In comparison, the ANU alneal samples were 1 Ωcm, n-type FZ Si wafers, 195 µm thick, oxidised to 140 nm at 1050 ˚C in dry oxygen. The entire 4″ wafers were coated on both sides with 100 nm 99.999% purity aluminium, thermally evaporated using a tungsten boat. The alneal for these wafers was done at ANU in forming gas at 400 ˚C for 30 minutes. After the alneal, the aluminium was etched off using warm (≤ 80 ˚C) phosphoric acid. Effective lifetime measurements for the whole wafers were taken at ANU.

The injection dependent lifetime curves for these two sets of samples are shown in Figure 22. From this, it is clear that one sample set achieved significantly higher effective lifetimes than the other. Although only the two best samples are shown in Figure 22, an increase in effective lifetime of this magnitude was not unique. Other samples processed in this way by Lobo [127] are included in Table V, with effective lifetimes ranging from 4090 to 6750 µs. The samples prepared at Oxford (as part of the present work), which present the higher

effective lifetimes, are referred to as the enhanced alneal samples, due to the enhanced carrier lifetimes. Those processed at ANU are referred to as standard alneal samples.

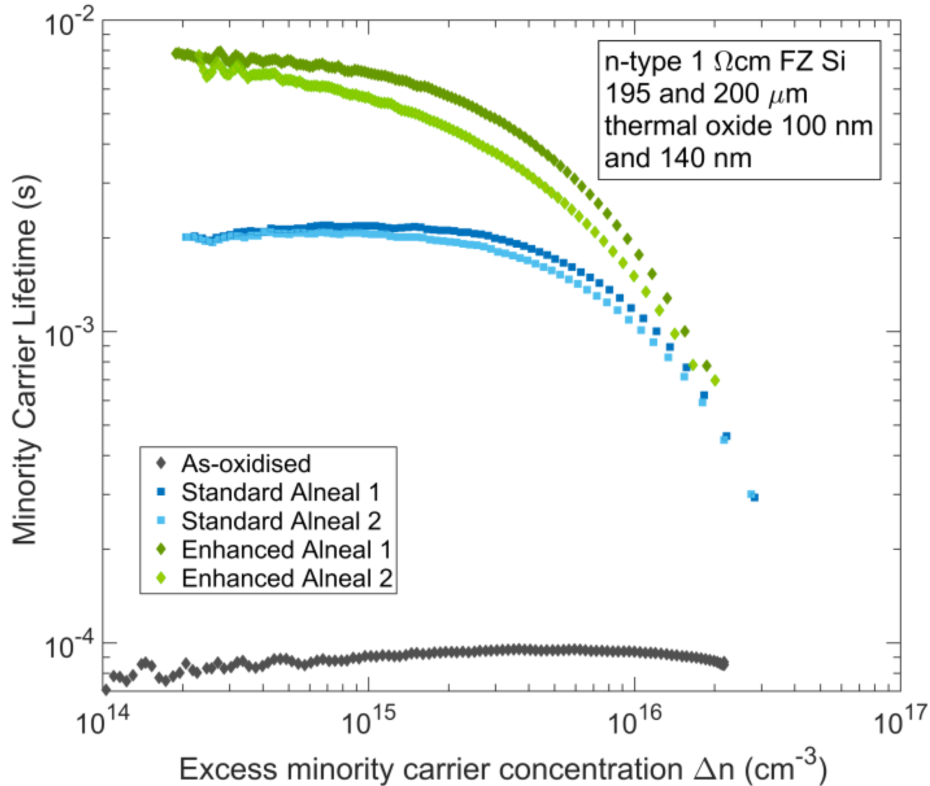

Figure 22. Injection level dependent lifetimes of enhanced alneal, standard alneal and as-oxidised samples. The numbers associated with the standard and enhanced alneal samples are for sample identification.

In Figure 22, the highest effective lifetime of the standard alneal wafer was 2180 μs, which is typical of standard alneal material reported in the literature [122–124, 126]. In comparison, the best enhanced alneal achieved an effective lifetime of 6750 μs. This is equivalent to a SRV of 0.15 cm/s and a J_{0s} of 0.1 fA/cm^2. To the author's best knowledge, with the exception of amorphous silicon [66], this is the lowest SRV reported for a silicon interface or surface at the time of writing [66]. This includes temporary near-optimal passivation techniques used for laboratory characterisation [128]. It must be noted that amorphous silicon is not suitable as an antireflection coating, it is predominantly used for selective contacts due to the superior surface passivation it achieves.

In order to understand the alneal passivation, the literature is summarised in the following section. There is substantial literature on the alneal, describing the passivation to be purely chemical.

4.2 THE ALNEAL PROCESS – BACKGROUND

The alneal, named such by Deal in 1970 [129], is one of the most effective methods of passivating the Si-SiO_2 interface [64, 65, 130–132]. The alneal process involves evaporating aluminium, ~ 0.1-1 μm thick, onto an oxidised silicon sample which is then annealed between 400 – 450 ˚C for 25 to 30 minutes [132–134], usually in forming gas (5% H_2, 95% N_2), before the aluminium is etched off in phosphoric acid at 80 ˚C [64, 130]. Annealing in alternative gas ambient has been shown to produce just as effective passivation. It was a technique used throughout the late twentieth century and was deemed to provide purely chemical passivation. Much of the characterisation was completed by measuring the density of interface traps as determined by capacitance-voltage techniques [135] or Electron Spin Resonance (ESR) [136].

From the 60s and 70s, there was much evidence to show that the alneal process would significantly reduce the interface trap density at the SiO_2-Si interface, the reduction was assumed to be caused by hydrogen. In 1965, Balk [137] proposed that the mechanism of hydrogen release was a reaction between the aluminium and water or hydroxyl ions present in or on the SiO_2 layer which releases atomic hydrogen, which is then free to diffuse through the oxide and passivate dangling bonds at the oxide-silicon interface. This theory is widely accepted [17, 20, 139–142, 31, 37, 65, 131, 132, 135, 136, 138] and no alternative has been suggested.

Balk's theory would imply water or hydroxyl ions are present, even in a dry thermal oxide, at a concentration sufficient to reduce the density of interface traps by two or three orders of magnitude from 10^{12} to 10^{9} cm^{-2} [37]. Beckmann and Harrick [143] found hydroxyl concentrations in the order of ~5 x 10^{18} cm^{-3} in dry thermal oxide using internal reflection spectroscopy. If one assumes that aluminium may react with hydroxyl ions within the first few nm of the oxide, this is equivalent to a hydroxyl density per cm^2 of ~10^{11} cm^{-2}, which is ample to provide trap passivation of the order achieved by the alneal. Unlike molecular water, which can be removed by heating at 100 °C, hydroxyl ions are not easily removed and require a vacuum anneal above 600 °C [37]. Thus, there is a source of hydroxyl ions at the Al-SiO_2 interface under most conditions.

To test whether hydrogen was responsible for the alneal passivation, Castro and Deal [139] attempted to replicate this passivation effect using molecular hydrogen from a forming gas anneal at 400 – 450 °C. They quantified the results using MOS (metal-oxide-semiconductor) measurements of interface states and found that fewer states were passivated during a pure hydrogen anneal than during an alneal. This led them to conclude that the alneal passivation is provided by hydrogen but that the hydrogen produced in the alneal is a more reactive species than molecular hydrogen. This reactive hydrogen species exists in a pure hydrogen gas as well, but at a lower concentration. This would account for the difference in passivation between the techniques. In an attempt to validate this, Swaroop [144] used both molecular and atomic hydrogen, produced by passing hydrogen over heated palladium, to passivate the SiO_2-Si interface. It was found that although molecular hydrogen gas did reduce the number of interface traps, because of the small quantity of reactive atomic hydrogen, the atomic hydrogen was four times more effective.

The theory of atomic hydrogen production during the alneal is supported by two more findings. Firstly, alneal passivation quality is unaffected by oxide thickness [37]. This indicates that the process is not limited by diffusion, which would be the case for atomic hydrogen. Secondly, the ambient under which the alneal is conducted is reported to have little impact on the effectiveness of the alneal [37, 134, 139]. This implies that the hydrogen is inherent to the alneal system and not introduced from the atmosphere. The density of interface traps is reported to reduce only for a certain length of time. After this time, the density of interface traps is seen to rise again [134, 141]. The explanation for this remains unclear.

It is suggested in some literature that alneal passivation is unstable [123] under UV conditions [131, 138, 145]. This is thought to be because the energetic photons cause hydrogen to be released from the interface where it is providing passivation. This can be characterised by boron dopant deactivation [145]. Decay in alneal effective lifetimes have also been reported by Zhao [123], who noticed the effective lifetime fall by over a third in the eight days after alnealing a 0.9 Ωcm n-type FZ material sample.

In the early 2000s, the alneal was characterised using photoconductance decay (PCD) effective lifetimes by Kerr and Cuevas [64], where a lifetime of 6 ms on 1.5 Ωcm 200 μm n-type FZ Si was achieved. This is equivalent to a SRV of 1.7 cm/s. The alneal was deemed such an effective passivation technique that it was used by Kerr and Cuevas [79] to characterise Auger and radiative bulk recombination. It has also been employed in the development of PERT [133, 146] and PERL [65, 124, 147] cells to achieve excellent surface passivation and enable high efficiency cells to be fabricated. However, it is not commercially viable because of the need for vacuum evaporation, a 30 minute anneal and subsequent etching of the metal.

The rest of this chapter will return to the standard and enhanced alneal carrier lifetimes, and assess whether in both cases the passivation is purely chemical or if there is a field effect aspect.

4.3 Comparison Between Experimental and Modelled Lifetimes

To verify whether the surface passivation seen in the enhanced and standard alneals could be achieved by chemical passivation alone, as suggested in the literature [20, 65], the experimental lifetimes were compared to an extended Shockley-Read-Hall model developed by Bonilla [66].

Figure 23 illustrates modelled lifetimes for a typical Si-SiO_2 interface, superimposed with the experimental results shown in Figure 22. Several studies have been performed on the Si-SiO_2 interface to determine the D_{it} and $\sigma_{n,p}$. Here, a range of D_{it} mid-gap values have been used to exemplify the typical and lowest reported in the work of Eades [26] and Nicollian [111], while $\sigma_{n,p}$ have been taken as typical as reported by Aberle [17].

For the standard alneal sample, it is clear from Figure 23 that an effective lifetime of this magnitude would be possible solely from extremely effective chemical passivation providing a $D_{it} \approx 10^9$ $eV^{-1}cm^{-2}$. Although D_{it} values this low are extremely uncommon, they are not unheard of. Eades [26] and Aberle [17] report some of the lowest values of D_{it} for alnealed Si-SiO_2 interfaces in the range of 1-5 x 10^9 $eV^{-1}cm^{-2}$. At a D_{it} of this value, negligible interface charge of 10^9 q/cm^2 is needed in order for effective lifetimes to reach ~ 3500 μs. As the standard alneal effective lifetimes are all below this value, the surface passivation could be entirely chemical.

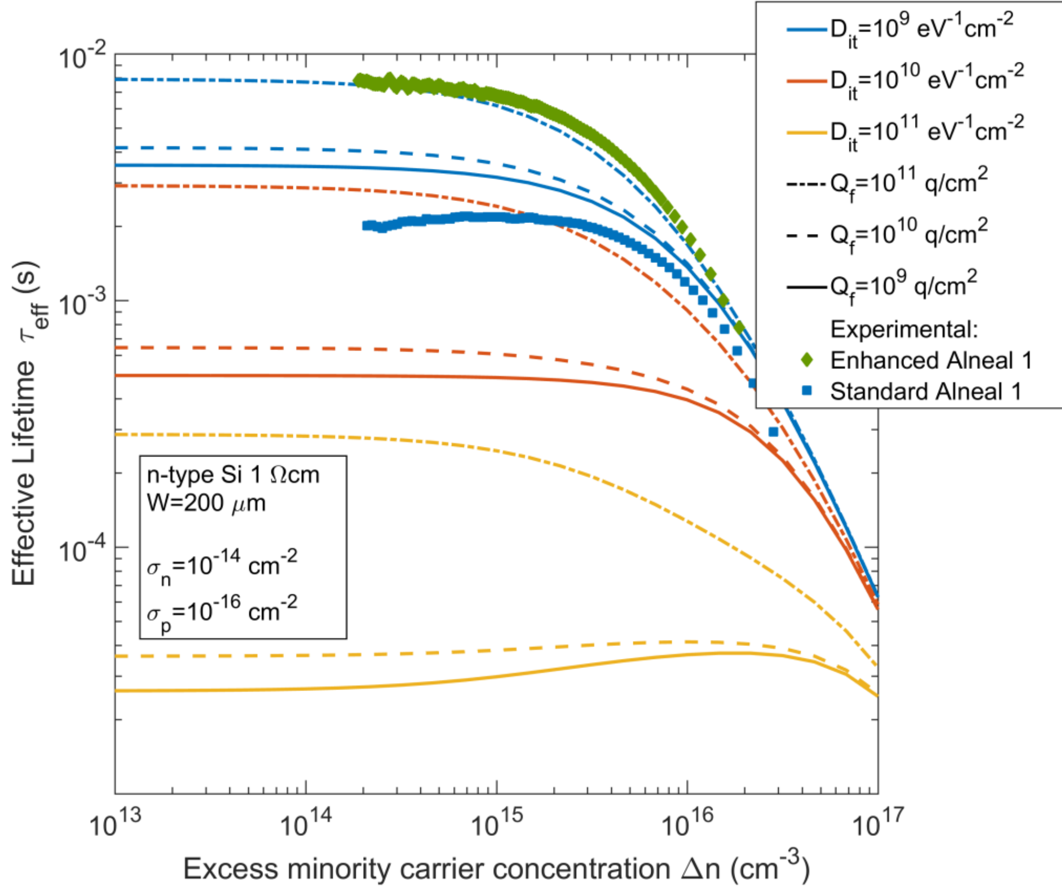

Figure 23. Simulated injection level dependent effective lifetimes showing D_{it} mid-gap values for an alnealed interface (typical, 10^{10} to 10^{11} eV^{-1}cm^{-2}, and extreme, 10^9 eV^{-1}cm^{-2}) [5], [10], [14], [36] and dielectric film charge Q_f for an as-grown thermal silicon dioxide (typical, 10^9 to 10^{10} q/cm^2, and extreme, 10^{11} q/cm^2) [17]. Experimental data from enhanced and standard alneal samples superimposed.

However, for the enhanced alneal sample, the modelling implies that there must be an aspect of field effect passivation to achieve effective lifetimes of this magnitude. From Figure 23, even if the D_{it} is as low as physically reasonable at 10^9 eV^{-1}cm^{-2}, it is not sufficient to produce lifetimes of 6.7 ms without the presence of FEP. According to the model, even with this extremely low D_{it}, a charge concentration of at least 10^{11} q/cm^2 is required.

Thus, by comparing the experimental data to the extended-SRH model, it has been shown that the most probable explanation for the high enhanced alneal effective lifetimes is the presence of FEP. In the next section, the interface trap density and interface charge concentration are investigated in detail.

4.4 FIELD EFFECT PASSIVATION AND THE ALNEAL PROCESS

The previous sections indicated that the quality of surface passivation provided by the enhanced alneal was highly likely to incorporate an aspect of field effect passivation, whereas the effective lifetimes of the standard alneal may be achieved by high quality chemical passivation alone. To validate these assumptions, dielectric charge measurements were made for both types of alneal.

4.4.1 DIELECTRIC CHARGE IN ENHANCED AND STANDARD ALNEAL

The enhanced and standard alneal samples, shown in Figure 22, were characterised to establish whether there was charge present in the dielectric. Both CV and KP measurements were taken to calculate the total concentration of dielectric charge. In all cases, the KP measurements were found to be negligible, indicating insignificant charge near the surface of the oxide. Therefore, the total dielectric charge is equivalent to the interface charge. Where noted, the CV measurements were taken on both sides of the sample to see if there was a variation between the two sample sides. Both sides of the silicon were planar polished. Two methods were used to measure the D_{it} of the Si-SiO_2 interface. Where it was possible, conductance D_{it} measurements were taken because the technique is more accurate. However, for the earlier measurements, Terman was used because the conductance measurement equipment was not yet operational. Before the enhanced alneal treatment, the samples showed an interface charge of ~ 2 x 10^{11} q/cm^2 and a D_{it} of 1 x 10^{11} $eV^{-1}cm^{-2}$ using the Terman method. The effective lifetimes, surface recombination velocities, surface saturation current densities, density of interface traps and interface charge values are summarised in Table V.

Table V. Alneal samples τ_{eff}, SRV, J_{0s}, D_{it} and $Q_{interface}$

Batch	τ_{eff} (µs)	SRV (cm/s)	J_{0s} (fA/cm^2)	D_{it} at midgap (eV^{-1} cm^{-2})	$Q_{interface}$ (10^{12} q/cm^2)
As-oxidised	90	112	1.3	1 x 10^{11} (Terman)	0.2
Standard Alneal 1 (ANU_7_1Ohm_2)	2170	3.3	1.6	1 x 10^{11} (Terman)	0.06
Standard Alneal 2 (ANU_8_1Ohm_2)	2050	3.5	2.4	Side 1: 1.1 x 10^{11} (Conductance)	Side 1: 0.2 Side 2: 0.2
Enhanced Alneal 1 (Ox_13_9_3_Al_BB_TE_ hp_425C_25m)	6720	0.15	0.1	Side 1: 2.8 x 10^{10} (Conductance)	Side 1: 1.8 Side 2: 1.3
Enhanced Alneal 2 (Ox_13_9_4_Al_BB_TE_hp_ 425C_25m)	5560	0.46	1.2	Side 1: 1.4 x 10^{10} (Conductance)	Side 1: 2.0 Side 2: 1.4
Enhanced Alneal L1* (UnOx_2-14_3)	4090	1.1	4.6	3 x 10^{11} (Terman)	1.4
Enhanced Alneal L2* (UnOx_2-14_10)	5640	0.4	2.1	3 x 10^{11} (Terman)	1.7
Enhanced Alneal L3* (UnOx_2-15_1)	4920	0.7	3.8	1 x 10^{11} (Terman)	1.3
Enhanced Alneal L4* (UnOx_2-15_3)	4550	0.9	4.2	1 x 10^{11} (Terman)	1.1

*Data from Lobo [127]

It was found that the interface charge differed substantially between the standard alneal and the enhanced alneal. For the standard alneal samples, the interface charge was small, in all cases less than 0.2 x 10^{12} q/cm^2. This is within the typical range of an as-oxidised Si-SiO_2 interface (0.05 x 10^{12} to 0.2 x 10^{12} q/cm^2 [17]). Whereas, for the enhanced alneal samples, the interface charge calculated from CV measurements was approximately an order of magnitude higher at 1 to 2 x 10^{12} q/cm^2.

It is postulated that this interface charge may be due to the presence of ionic species at the SiO_2-Si interface. If this were the case, this concentration of ions would represent only 1/100th of a monolayer as the density of silicon surface atoms is ~ 7 x 10^{14} cm^{-2} [17]. Historically, there has been some concern that the presence of ionic species at the SiO_2-Si interface may introduce states into the bandgap resulting in a reduction in chemical passivation. There are several unknowns regarding ion behaviour at the SiO_2-Si interface. Firstly, it is possible that only a proportion of ionic species that reach the SiO_2-Si interface remain charged and contribute to FEP. Secondly, not all ions may have an impact on the chemical passivation. Thirdly, it could be the case that once a certain number of ions are situated at the SiO_2-Si interface, the subsequent species are no longer charged, but could be electrically active, thus introducing bandgap states. All of this is investigated in greater detail in Chapter 6, where the relationship between effective lifetime and interface charge concentration is studied.

In the work presented in this chapter, due to the high-quality effective lifetimes of the enhanced alneal samples, the chemical passivation does not appear to be compromised by the presence of ions at the interface. This is supported by the D_{it} measurements, which are low across all samples, and especially low for enhanced alneal 1 and 2. There are several possible explanations for this. Either the concentration of ionic species introduced is not

sufficient to affect the chemical passivation, the species causing the charge do not introduce recombination active trap levels in the bandgap or, if trap levels are introduced, simultaneous passivation of these traps is occurring.

This data led to the conclusion that the remarkably low SRV values provided by the enhanced alneal are due to the presence of increased interface charge, which is absent in standard alneal specimens.

Having determined that the enhanced alneal passivation was due to an aspect of FEP, it was of interest to establish whether the standard alneal chemical passivation could be improved to provide the same quality passivation as the enhanced alneal with the addition of FEP. This was achieved by the use of corona charge on the oxide surface.

4.4.2 ADDITIONAL CHARGE FROM CORONA DISCHARGE

To investigate the impact of increasing FEP for both standard and enhanced alneal samples, corona charge was deposited in incremental steps onto both oxidised surfaces of the quarter-wafer samples. After each deposition, both the effective lifetime of the sample and a KP measurement was taken to calculate the surface charge density of the corona deposition. The cleaved edge, on which no SiO_2 was present, was used to contact the silicon substrate directly in order to achieve a KP measurement. This was used to calculate the total surface charge concentration. Once the effective lifetime was found not to increase further with additional corona charge, the process was stopped. This prevented damage to the sample through oxide breakdown.

By maximising FEP on both types of sample, it is possible to gather an understanding of the quality of the chemical passivation. With the addition of corona charge, the field-effect

passivation is optimised and because FZ n-type silicon is used, the bulk lifetime is high enough to make it unlikely to be the limiting factor. Therefore, the effective lifetime is limited by the chemical passivation of the SiO_2-Si interface and any differences between samples in chemical passivation are exposed.

The effective lifetime variation with dielectric total surface charge for a 1 Ωcm standard alneal sample is shown in Figure 24 (a) and the same is shown for an enhanced alneal sample in Figure 24 (b). The standard alneal surface charge is initially slightly negative, unlike that of the enhanced alneal, which is zero.

From Figure 24 (a) it is clear that the addition of FEP is capable of improving the lifetime of a standard alneal specimen. By increasing the oxide surface charge to + 0.9 x 10^{12} q/cm^2, the effective lifetime improves to 5300 µs, equivalent to the SRV reducing to 0.5 cm/s. This is a significant improvement on any SRV reported solely due to the standard alneal process and reiterates that FEP can improve alneal passivation, which is already considered high quality. In fact, the effective lifetime achieved by the standard alneal with the addition of FEP corona charge is remarkably similar to that of Enhanced Alneal 2 of 5500 µs. This indicates the importance of FEP in providing outstanding effective lifetimes.

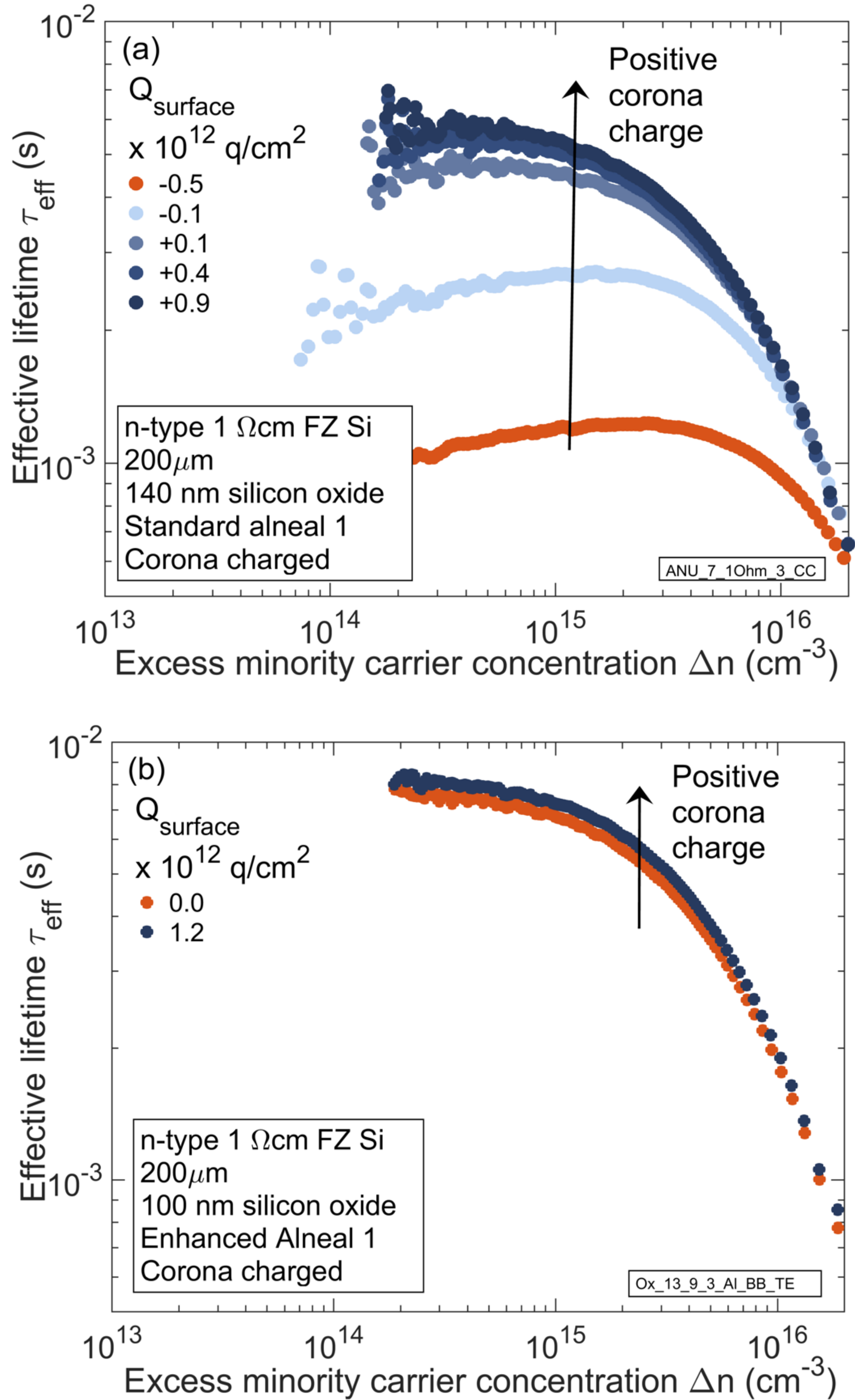

Figure 24. Injection dependent effective lifetimes for (a) standard alneal 1 and (b) enhanced alneal 1 both with the addition of positive corona charge to the oxide surface, with the total surface charge reported as $Q_{surface}$.

Enhanced Alneal 1 also underwent corona charging, as shown in Figure 24 (b). This was to understand how close to optimal the dielectric charge concentration already was. With the addition of corona charge the effective lifetime of the enhanced alneal improved from 6720 μs to 7250 μs. With the exception of an amorphous silicon coating [66], these lifetimes are believed to be the highest achieved on 1 Ωcm n-type material. The effective lifetime of 7250 μs is equivalent to an SRV of 0.05 cm/s. It is not possible to calculate an accurate J_{0s} for an effective lifetime of this magnitude as it exceeds the theoretical bulk lifetime used in the model. When surface passivation is of such high quality, the recombination at the sample edge can become limiting. Bonilla [148] established that for 1 Ωcm FZ material, the size of a quarter 4″ wafer, edge recombination becomes limiting at effective lifetimes ~ 7.2 ms. Therefore, it is likely that the effective lifetime of the corona charged, enhanced alneal sample is edge limited instead of surface limited, meaning that the actual SRV is probably lower than the value quoted in this work. This effective lifetime is very significant because, despite the potential limiting effect of the edges, the lifetime exceeds the Richter [51] limit for intrinsic lifetime at certain injection levels. This is shown in Figure 25 and highlights the need for a new model for the intrinsic lifetime limit. Since first submitting this thesis, Veith-Wolf et al. [149] published an article re-assessing the intrinsic carrier lifetime limit.

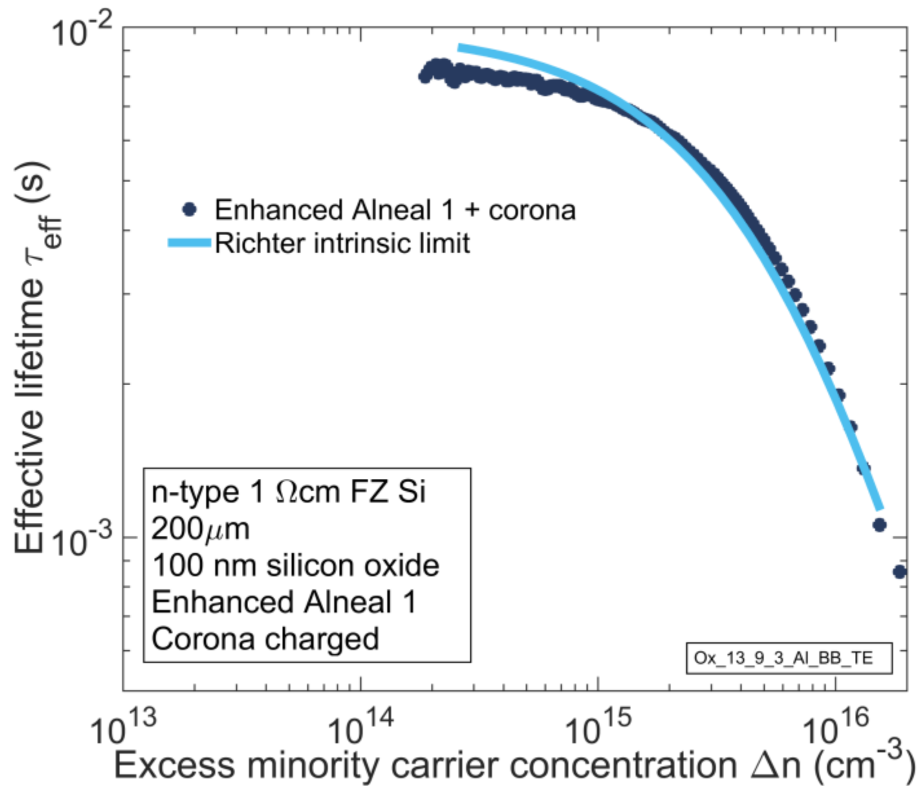

Figure 25. Injection dependent effective lifetimes for enhanced alneal 1 with the addition of positive corona charge to the oxide surface and Richter intrinsic lifetime limit.

The results in this section have shown that the quality of the enhanced alneal passivation was due to the presence of charge in the oxide. However, the cause of the dielectric charge was unknown and will be considered in the following section.

4.5 DETAILS OF CHARGE IN THE ENHANCED ALNEAL

It was hypothesised that the increased interface charge was due to the presence of ionic contaminants that were present for the enhanced alneal specimens but were not present in the standard alneal specimens.

4.5.1 IDENTIFYING CHARGED SPECIES

Two techniques were employed to identify what was causing the charge in the enhanced alneal, and to analyse whether it was due to ionic species. The first is thermally stimulated ionic conduction (TSIC) and the second is Secondary Ion Mass Spectroscopy (SIMS).

4.5.1.1 TSIC ANALYSIS

The hypothesis of ionic contaminants was tested by Thermally Stimulated Ionic Conduction (TSIC) processed using a constant temperature ramp rate up to a temperature of 300 ˚C. This temperature was held for the time necessary to see the current reading fall to near its original value. This was taken to be an indication that interface charge had saturated and that the available ions had all migrated across the oxide. In this instance, the TSIC was performed with a 5 V bias using an aluminium front contact deposited in the same thermal evaporator as the aluminium for the enhanced alneal specimens.

The TSIC showed an ionic drift current during processing, indicating that the migration of ions through the oxide was likely to be occurring. From TSIC current-time curves it is not possible to identify if positive ions are migrating in one direction or if negative ions are migrating in the opposite direction. It is also not possible to ascertain whether the migrated ions remain charged at their destination position. This must be characterised by CV measurements. However, much work was done in the 70s and 80s to characterise the temperature of current peaks caused by Li, Na and K ions migrating from the Al-SiO_2 interface to the SiO_2-Si interface [150–152]. By comparing the position of the peaks in the TSIC current-time data shown in Figure 26, to the position of known contamination peaks, it is possible to identify these ions.

From the position of the peaks it is likely that both Na^+ and K^+ migrated through the oxide layer to the Si-SiO_2 interface. A greater concentration of K than Na appears to be present. This can be quantified by integrating the area under the TSIC curve and by assuming that the species exist in a +1 charge state. The TSIC data is shown in Figure 26 along with the integrated current values showing the charge density for Na and K.

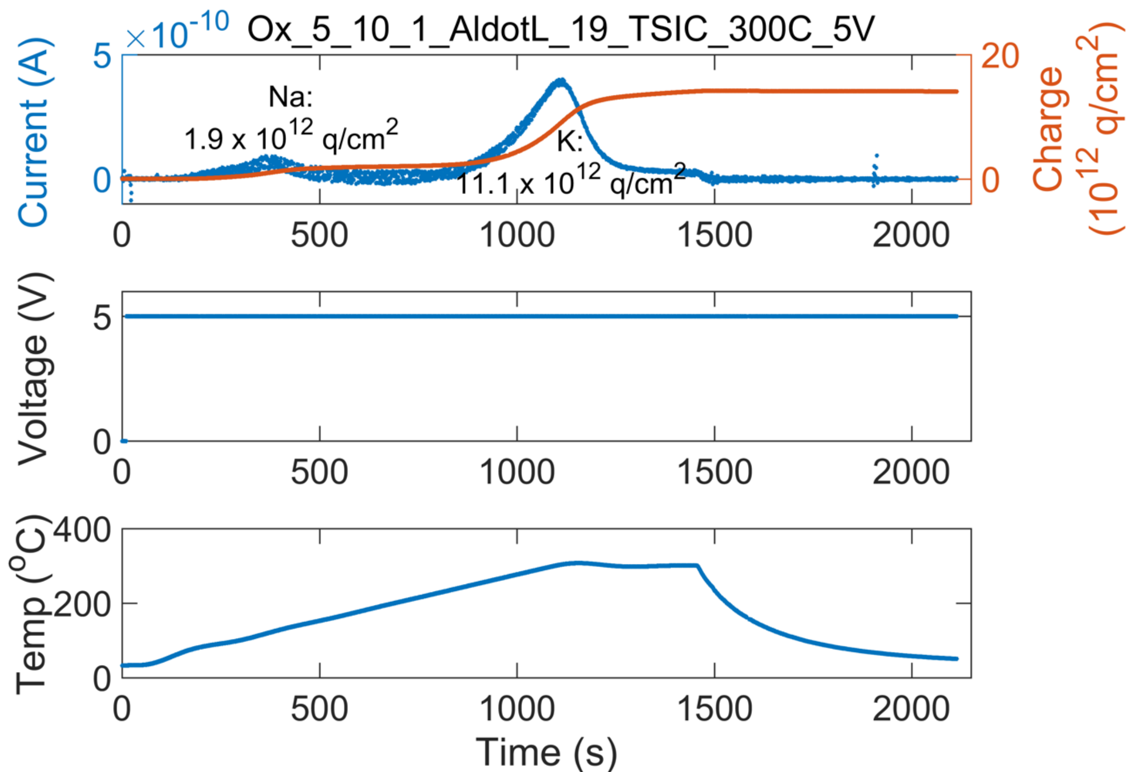

Figure 26. TSIC data for an Al front contact deposited in the same thermal evaporator and the Al for the enhanced alneal with sub plots of current and charge, voltage, and temperature, all against time. The maximum temperature is held for a given time to ensure all the available ions have the opportunity to migrate.

After TSIC processing, the interface charge was measured by CV, and the interface charge concentration was found to be even greater than that found in the enhanced alneal specimens. For TSIC processed samples the interface charge concentration ranged from 4 to 13 x 10^{12} q/cm^2, due to variation in contamination. For enhanced alneal specimens it was in the range of 1 to 2 x 10^{12} q/cm^2. Due to the small area of the TSIC process, these specimens could not be used for lifetime measurements. The magnitude of charge introduced

through TSIC also discounted the possibility of D_{it} analysis as the voltage it would have been necessary to apply to the sample was beyond the equipment range. In an attempt to identify the ionic species causing the interface charge, samples were analysed using SIMS.

4.5.1.2 SIMS Analysis

The second analysis method was SIMS. These measurements were conducted at Aystorm Scientific Ltd. The SIMS profile for a TSIC sample, processed in the same way to that shown in Figure 26, is displayed in Figure 27 (a) and the profile of Enhanced Alneal 1 is shown in Figure 27 (b). Both the SIMS profiles show that sodium and potassium are present at the SiO_2-Si interface. The broadening of the impurity peaks across the SiO_2-Si interface can be an artefact of the technique.

From the SIMS data it is possible to calculate the cumulative charge per unit area within the dielectric. This is calculated by integrating the concentration (at/cm^3) of K and Na detected with respect to depth using the cumulative trapezoidal method and are given in Table VI. The integration is conducted for the peak at the marked interface between a depth of 97 nm and 135 nm for Figure 27 (a), and between 100 nm and 140 nm for the sample in Figure 27 (b). For the TSIC processed Al dot in Figure 27 (a) the concentrations of Na and K near the interface were very similar to the value of charge calculated from the CV measurement and the total migrated charge calculated fr om the TSIC current data, which are given in Table VI. This similarity in concentration of Na and K from SIMS and charge concentration from TSIC and CV is strong evidence that Na and K atoms are the ionic species responsible for the interface charge.

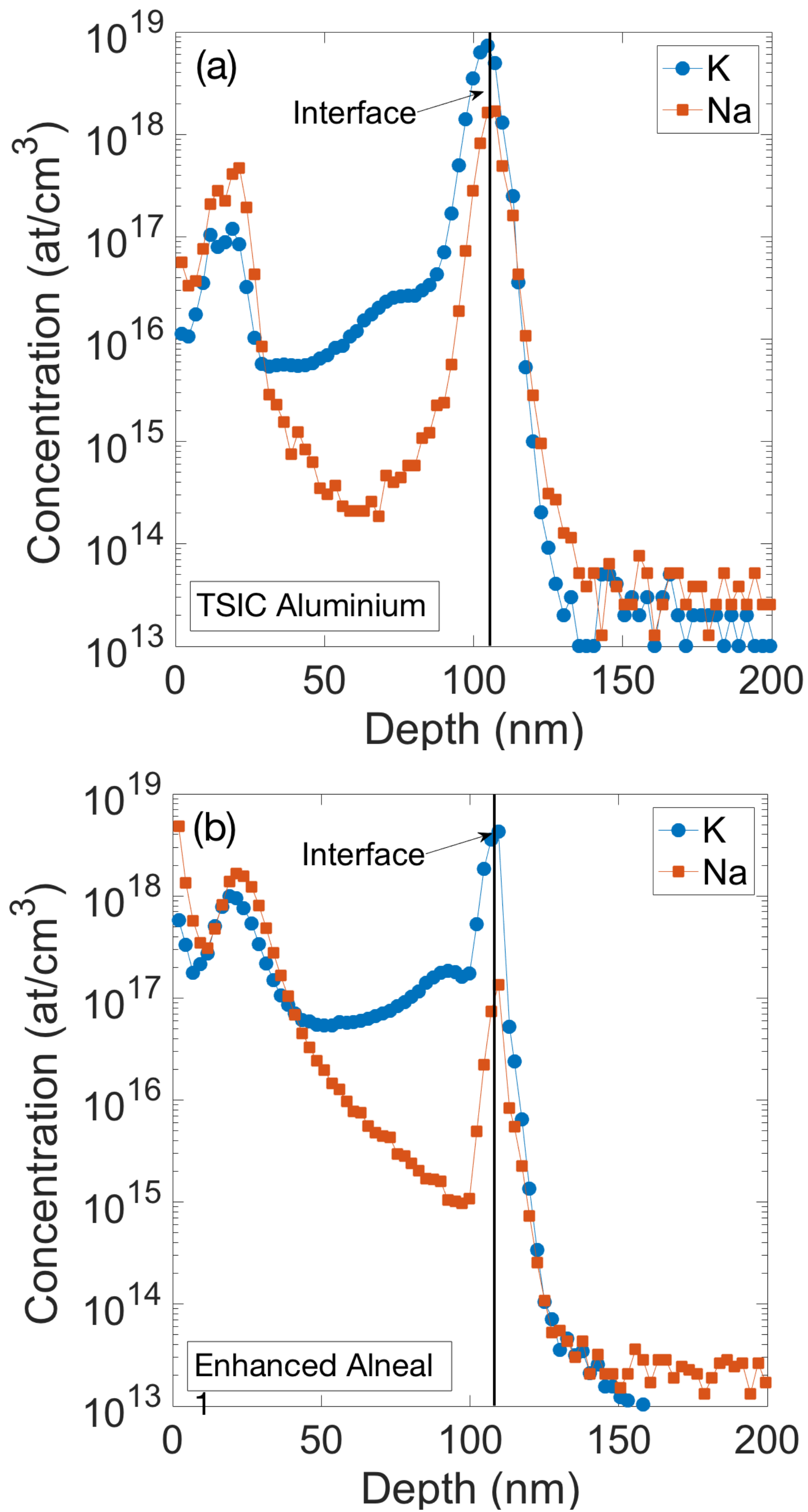

Figure 27. SIMS results of (a) a sample with an Al front contact deposited in the same thermal evaporator as Al for the enhanced alneal, which has undergone TSIC with the temperature ramping to 300 ˚C with a 5 V bias applied and (b) Enhanced Alneal 1. SiO_2 on the left and Si on the right of the marked interface.

For the Enhanced Alneal 1 there was not such a clear similarity between the SIMS concentration of Na and K species and the charge concentration measured from CV. This could be because the resolution of the SIMS is lower for the Enhanced Alneal 1 sample due to a larger depth between measurements. The cumulative trapezoidal method could therefore result in an overestimation of the species concentration at the interface.

Table VI Species concentration from integrated TSIC current-time data and from integrated SIMS concentration data

Sample	Measurement Type	Na	K	Total
TSIC sample	CV (10^{12} q/cm^2)	-	-	13.0
	TSIC (10^{12} q/cm^2)	1.9	11.1	13.0
	SIMS (10^{12} at/cm^2)	1.9	9.3	11.2
Enhanced Alneal 1	CV (10^{12} q/cm^2)	-	-	1.8
	SIMS (10^{12} at/cm^2)	0.07	2.8	2.9

Having identified the charged species using SIMS, it was important to ascertain at which stage the contamination was introduced into the system. Until this was accomplished, control over the concentration of ionic contamination was not possible.

4.6 SOURCE OF CHARGE

The next step was to identify the origin of the charge. It is possible to diffuse, or drift, both Na and K ions into a thermally grown SiO_2 film where they reside at the Si-SiO_2 interface in a charged state [61]. However, for the enhanced alneal, no intentional Na or K contamination had occurred. In addition, Fraunhofer ISE, where the oxidation was performed, had no evidence of contamination. Samples which had not undergone an anneal after aluminium deposition also showed no interface charge. Charge appeared only after aluminium deposition (in the Oxford cleanroom thermal evaporator) and annealing. Several routes by which charge could be introduced to the system were identified. Contaminants may have come from the oxide surface, from the vacuum chamber, be contained within the evaporated aluminium, or come from the tube furnace. Each of these possibilities was tested and a summary is given below. The results are available in Appendix I.

Extensive tests were conducted in order to eliminate each of these sources of contamination. RCA cleaning was used to clean the surface of the oxide, this was found to make negligible difference. To test the surface in an alternative manner, e-beam aluminium was used instead. After processing using TSIC, no interface charge was found using the e-beam aluminium; therefore, the contamination could not be from the oxide surface. The furnace was also found to be an unlikely source of contamination as controls without the presence of Al were annealed. The vacuum at the time of deposition in the thermal evaporator was varied and found to make little difference. Higher purity aluminium was used on a tungsten coil, which again did not eliminate the contamination. It was not possible to evaporate the aluminium from an aluminium oxide crucible due to current limits of the equipment. However, after cleaning the thermal evaporator walls using etchant, replacing the copper electrode arms, and using a new sample holder, contamination was still present in the system. It was

concluded that the contamination was highly likely to be due to the thermal evaporator. Fortunately, at this time, an alternative thermal evaporator at the main laboratory was refurbished and available, so attempts to clean the thermal evaporator in Begbroke ceased.

4.7 CONCLUSIONS

In this chapter, it was shown that alneal passivation, which for decades was considered the most effective passivation technique, can be improved by the addition of ionic field effect passivation. Although the origin of the ions could not be isolated and is understood to be due to contamination, it was possible to identify the ionic species. Thermally stimulated ionic conduction evaluation and SIMS measurements showed the ionic species to be K and Na. The presence of these ions at the interface, with the addition of the chemical passivation provided by the alneal, enabled world record surface passivation to be achieved. From this, one can conclude that ionic field effect passivation has a significant role in achieving high quality surface passivation and an industrial process by which these ions can be introduced could be of value to the industry. The mechanism by which the ions migrate to the SiO_2-Si interface remains undefined. This is investigated in the next chapter with the hope that the findings may aid the development of an industrially-viable deposition and migration technique.

CHAPTER 5
ION INTRODUCTION DURING ENHANCED ALNEAL

In the previous chapter, the source of the charge present in the enhanced alneal was identified. It was concluded that it is caused by potassium and sodium contamination of the thermal evaporator. However, the mechanism by which the charge is introduced to the Si-SiO_2 interface during the alneal was not considered. As the enhanced alneal improves the surface passivation of samples significantly, reaching values superior to that of the standard alneal, understanding the mechanism of ion introduction could help to develop an industrially appropriate process. In this chapter, the introduction of charge is characterised with respect to anneal parameters and a model for the charge introduction is presented.

5.1 ION INTRODUCTION

To understand the rate at which the ionic charge is introduced, samples were alnealed for various lengths of time before the interface charge concentration was measured. Cz, n-type Si, ~ 40 Ωcm, thermally oxidised to 100 nm was cleaved into samples ~ 1 cm^2. These were deposited with 100 nm aluminium on one side, using the thermal evaporator which had been found to be contaminated with Na and K, as explained in Chapter 4. The samples were then annealed at 400 °C in air on a hot plate to allow sufficient control over the sample temperature and anneal time. After the anneal, the aluminium was removed using commercial etchant at 50 to 80 °C, as described in Chapter 3. The back oxide was etched off using hydrofluoric acid on the tip of a cotton wool bud and a contact was made directly

to the silicon using indium-gallium and conductive silver dag. Hg-CV measurements, as described in Chapter 3, were performed to measure the charge at the Si-SiO_2 interface and the results are shown in Figure 28. It was found that ionic charge was present at the Si-SiO_2 interface after the shortest anneal time of only 15 seconds.

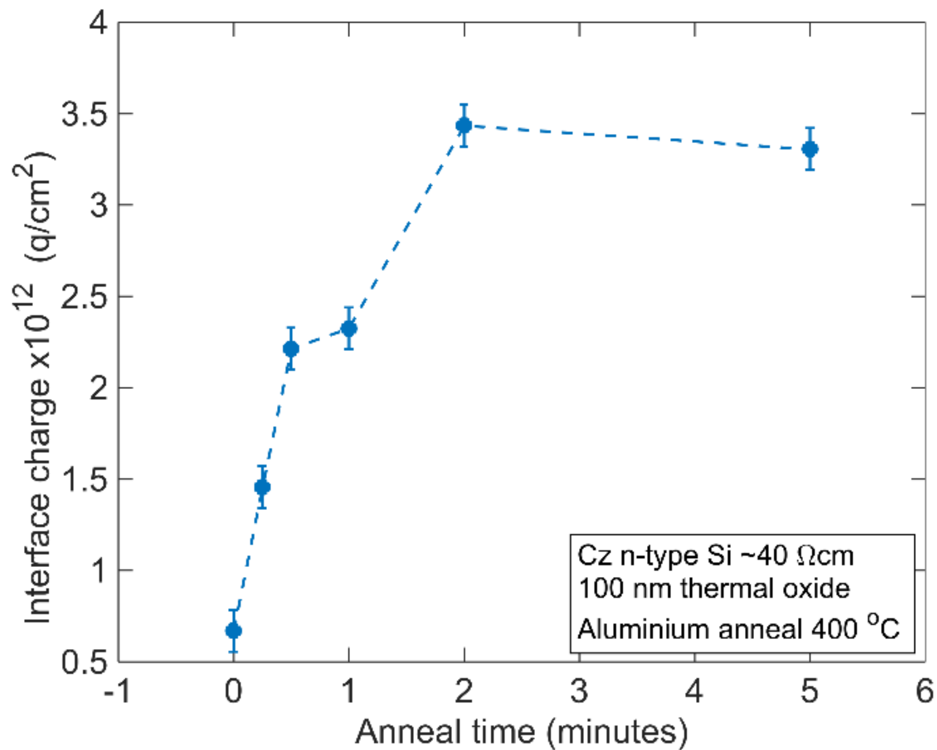

Figure 28. Interface charge concentration after an aluminium anneal at 400 ˚C. Al deposition in contaminated thermal evaporator.

The data in Chapter 4 shows that the high effective lifetimes achieved by the enhanced alneal incorporated a charge concentration of 1-2 x 10^{12} q/cm^2. From Figure 28, a charge concentration of this magnitude is introduced at 400 °C in under 15 seconds. It appears that the interface charge concentration saturates in 2 minutes, which is believed to be because the supply of available ions at this temperature is depleted.

The speed at which ions are introduced to the Si-SiO_2 interface from the Al-SiO_2 interface is much faster than when ions diffuse from the air-SiO_2 surface to the Si-SiO_2 interface. Work on this has been conducted by Bonilla et al [61] who found that, at 400 °C,

introduction of K into the dielectric can take over an hour to provide charge concentrations similar to those seen in the enhanced alneal. In comparison, the enhanced alneal ion introduction takes 15 seconds.

For the ions to reach the Si-SiO_2 interface requires a two-stage process of injection and migration. Previously, authors have concluded that diffusion of mobile ions is not the limiting step [152–154]. Instead, the required anneal time for ions to reach the SiO_2-Si interface is said to be defined by the rate of injection. Figure 29 presents an energy diagram for a positive ion in an electrically isolated Al-SiO_2-Si structure. It is modelled with an energy well for ions both at the Al-SiO_2 interface and the SiO_2-Si interface. It is this energy well which provides the barrier for the introduction of positive ions into the oxide. The ion injection rate will depend on the attempt frequency, *s* (which has a weak dependence on activation energy [152]), and the required activation energy, $E_{A(Al\text{-}Ox)}$, necessary to overcome the barrier height. The barrier height at the Al-SiO_2 interface and the SiO_2-Si interface can vary, which is indicated by the differing depth of energy wells in Figure 29.

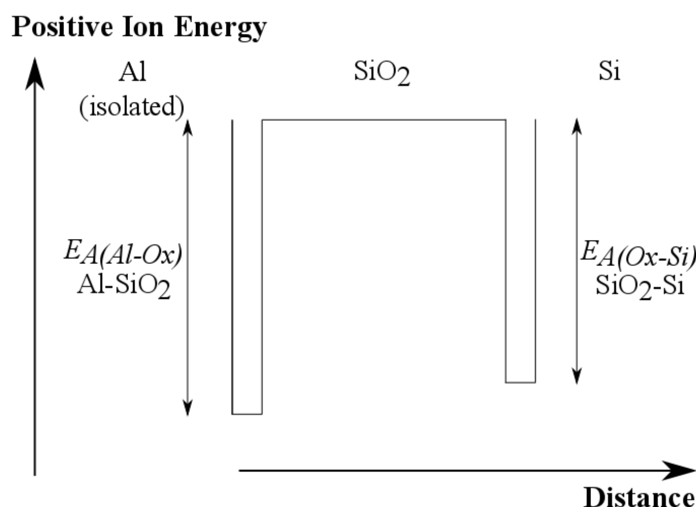

Figure 29. Schematic energy diagram of energy against distance into the sample (from the aluminium top contact, left, to the silicon, right) for a positive ion in an electrically isolated Al-SiO_2-Si structure.

The activation energies for Na and K injection into SiO_2 from the Al-SiO_2 interface and the SiO_2-Si interface have been investigated in the literature [150, 152–159]. Hickmott [150, 152, 155] describes the probability of ion injection, P, with first order kinetics, as in equation (5.24), assuming a single energy trap level.

$$P = s.\exp\left(\frac{E_A}{kT}\right) \tag{5.24}$$

In later works, a distribution of traps was found to better model the system [152], however, it is necessary to know the initial distribution of the trap energies [150]. Attempts to model the initial trap distribution in different ways have been made [151, 160], although so far a satisfactory model is yet to be developed.

Nauta and Hillen [151] found that, under a bias of ± 170 kV/cm, $E_{A(Al\text{-}Ox)}$ = 1.10 eV for Na and 1.65 eV for K and $E_{A(Ox\text{-}Si)}$ = 1.01 eV for Na and 1.65 eV for K. Hickmott [150] describes how the application of an electric field is capable of lowering the activation energy for Na release from the SiO_2-Si interface from 1.1 eV to 0.7 eV under a field of 8 x 10^5 V/cm. The effect of this external bias is considered in section 5.3, as it is believed to have a significant impact on the migration process.

As described by the results presented in this section, the rate of injection and migration of ions to the SiO_2-Si interface is greater for an enhanced alneal than from an air-SiO_2 interface. This indicates that either the energy well where the ions sit at the Al-SiO_2 interface is shallower than at the air-SiO_2 interface, or that there is some driving force encouraging the escape or migration of ions, or both.

In order to better understand the system, further experiments were conducted. During these experiments, variation in the concentration of interface charge between samples was

recorded. Under some conditions charge was apparent at the interface after an anneal, and under other conditions no charge was present.

5.2 The Effect of Different Sample Structures

In the process of analysing ionic introduction, two sample structures were tested. One type was prepared for the purpose of alnealing and had an oxide surface fully covered on one side (the top side) in Al. The back oxide was left intact during the anneal but without aluminium deposition. For the aluminium deposition on the top surface, no mask was used during the evaporation and therefore the whole oxide surface and the sides of the sample were exposed to the aluminium evaporation source. This is referred to as a fully covered sample. The second type was prepared for TSIC. These had a MOS structure of an electrically isolated dot of aluminium in the centre of the oxide surface created by using a mask during evaporation. When the two types of samples were annealed, the MOS structures showed very little interface charge. Whereas, specimens with an oxide surface fully covered in aluminium, deposited under the same conditions, showed significant charge. The interface charge after annealing the two sample structures on a hot plate at 400 °C for 5 minutes is shown in Figure 30. The results shown are for different samples rather than repeat measurements of the same samples.

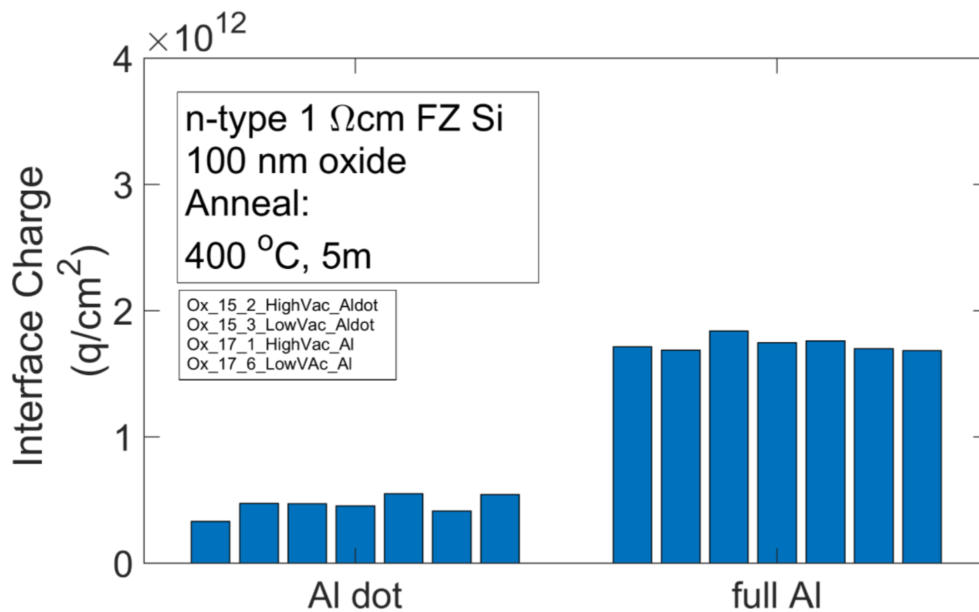

Figure 30. Interface charge after annealing with either the oxide fully covered in Al or an Al dot in the centre of the oxide. Al depositions made in the contaminated thermal evaporator.

This clear difference between the two sample types could have been caused by the following variations in sample processing between the sample types. The first variation was the use of a mask during aluminium deposition for the MOS structures. The second was that an etchant was used to remove the aluminium from the surface of the fully covered sample before CV measurements. The third was that different CV measurement types were used; Hg-CV was used after aluminium removal for the fully covered samples, whereas the aluminium remained in place and the CV measurement was carried out using probes for the MOS structure. Alternatively, the final option could be that the difference in resulting charge could be inherent to the difference in the aluminium coverage of the oxide surface. Each of these variations is investigated in turn to identify the cause of the different interface charge concentrations.

5.2.1 USE OF MASK DURING AL DEPOSITION

A mask was used during MOS structure preparation to ensure individual aluminium dots were evaporated onto the oxide surface. A mask was not used when aluminium was evaporated to cover the full surface of the oxide and the edges of the sample. When the MOS samples were annealed, no charge was present at the interface. In order to determine whether the mask was interfering with the aluminium deposition, an aluminium dot was fabricated without the use of the mask. To do this, a sample was fully coated with aluminium and through chemical processing, using lacomit to protect a region of the aluminium surface, the rest of the aluminium was removed with Al etchant. This structure was then annealed, and the interface charge measured, as shown in Figure 31. This process removed the use of a deposition mask but maintained the MOS structure.

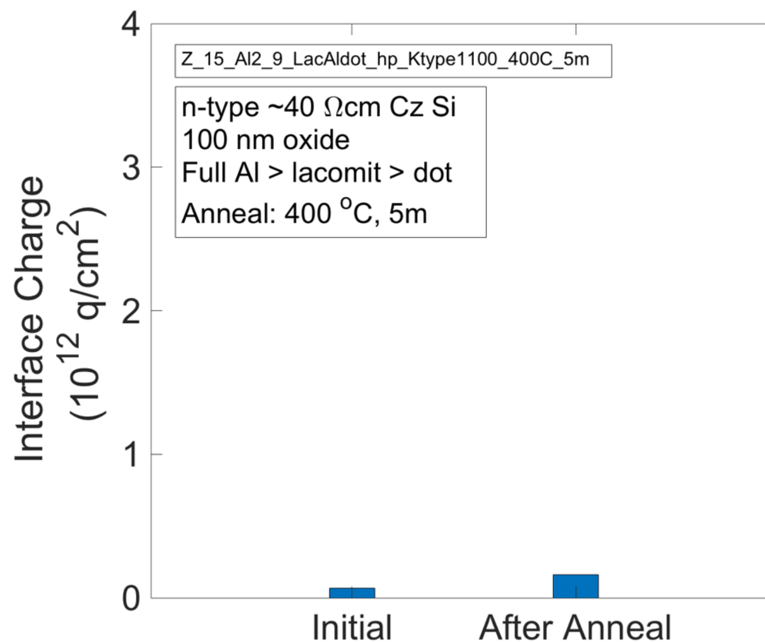

Figure 31. Interface charge measurement before and after the following processing: Full Al evaporation in contaminated thermal evaporator. MOS structure formed using Al etchant and lacomit to protect an area of the Al. This structure was then annealed at 400 °C for 5 minutes. After the anneal, the back oxide was removed with HF and a back contact was formed using InGa and silver dag. CV measurement was taken using the probe station and Al dot on the top surface.

As seen in Figure 31, there was no significant interface charge after the anneal, as the equipment error is 0.1 x 10^{12} q/cm^2 [113]. This suggests that the presence of the mask during aluminium deposition was not responsible for the lack of charge. This led to the investigation of the etchant.

5.2.2 AL ETCHANT OR TYPE OF PROBE

In order to clarify if the etching process was responsible for the introduction of charge to the Si-SiO_2 interface, a sample fully covered with aluminium was annealed. It had been the case previously that after an anneal of this type, the aluminium would be etched, and charge would be present at the interface if a Hg-CV measurement was taken. But now the question was whether the charge would be present if no aluminium etchant was used. The simplest way to test this was to leave the aluminium in place. This could not be done using the whole metal surface as the front contact, because a front contact of a smaller area was required. A diamond scribe was used to break through the aluminium and oxide layer, leaving an island of oxide and aluminium in the centre of the sample. Electrical isolation from the surrounding aluminium was confirmed using a resistance meter. This allowed a CV measurement to be taken using probes, as was the norm for CV measurements of the MOS structures. This CV measurement confirmed the presence of charge at the Si-SiO_2 interface, as shown in Figure 32, thereby proving that the charge was already present before the use of aluminium etchant, so it could not be the etchant causing the charge.

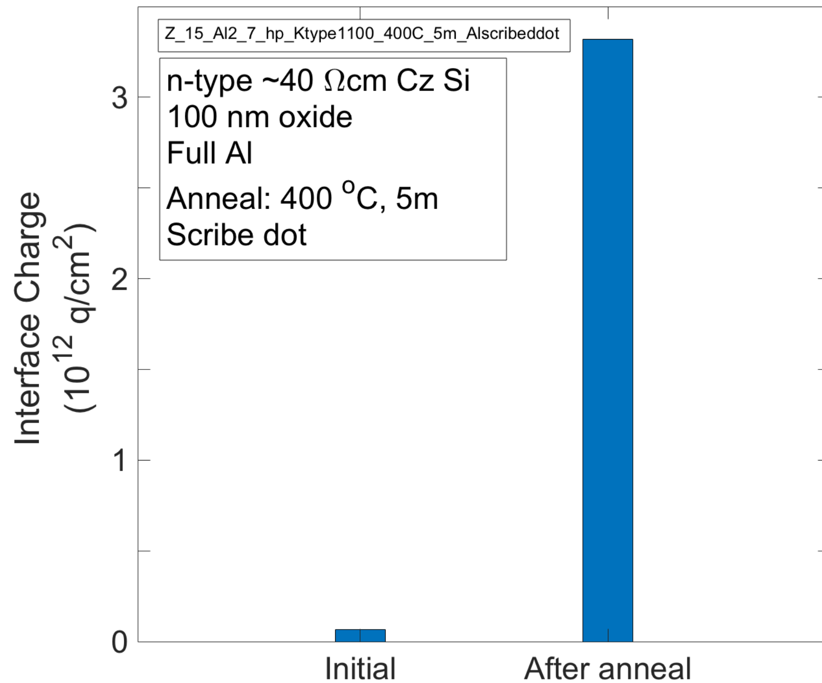

Figure 32. Interface charge before and after the following processing: Full Al deposition using contaminated thermal evaporator. Annealed at 400 °C for 5 minutes. After annealing, an MOS structure was fabricated using a diamond scribe to form an isolated dot in the top metal. Back oxide was removed with HF and contacted using InGa and silver dag. CV measurement was taken using the probe station and Al dot on the top surface.

This also discounted the possibility that the different CV measurement devices, probe vs Hg, were causing different results because the result here, using the probe CV, was as would be expected had the Hg-CV probe been used.

Having recognised that the discrepancy in interface charge was not caused by the evaporation mask, the etchant or the type of CV measurement, the difference in aluminium coverage of the oxide during the anneal was investigated.

5.2.3 The Impact of Differing Aluminium Coverage of the Oxide During the Anneal

The above results demonstrate that it is not the difference in processing steps between the two types of sample that results in charge being present in one sample type and not the other after an anneal. Therefore, it must be the difference in aluminium coverage of the oxide that is responsible for the migration of charge in the fully covered samples and not in the dot samples. As mentioned above, the fully covered samples did not use a mask during aluminium deposition, which left the side of the samples exposed to the evaporation source. As full wafers were not used during the experiments carried out at the Oxford laboratories, all samples had been cleaved (the process of cutting wafers) which leaves an exposed silicon edge. This exposed silicon edge would be deposited with aluminium during the evaporation process. This would allow an electrical contact to exist between the silicon and the aluminium.

It was hypothesised that, because charge at the interface was only seen in samples where the oxide surface was fully covered in aluminium and where an electric contact between the aluminium and silicon was likely along a cleaved edge, it was possible that charge only migrates when the aluminium is electrically connected to the silicon. In order to test this hypothesis, a MOS sample was annealed on the TSIC equipment with a 0 V bias applied between the silicon and the top metal dot contact to enforce electrical connection. The interface charge results for both sample structures, annealed for different lengths of time, are shown in Figure 33 along with the MOS sample where the aluminium dot was electrically connected to the silicon.

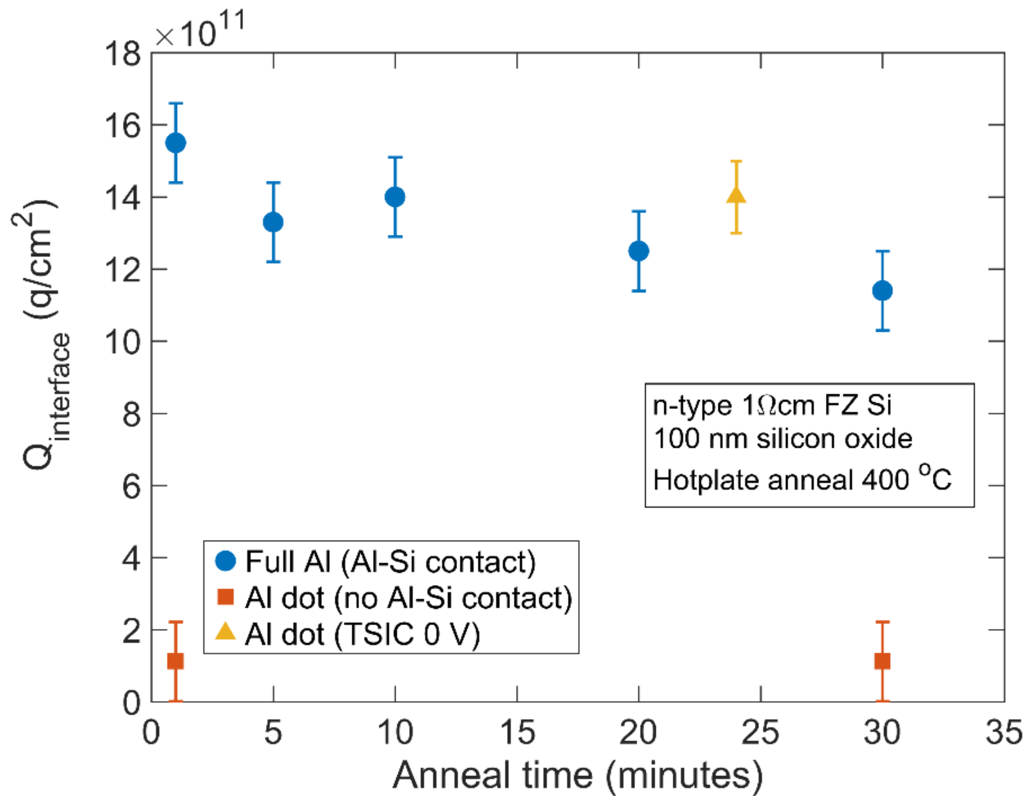

Figure 33. Interface charge against anneal time at 400 ˚C on hotplate. The anneals were conducted with the oxide surface either fully covered in aluminium (blue), or a 2 mm diameter aluminium dot in the centre of the oxide (orange). Error bars are shown as calculated in [113]**. For comparison, a sample with an Al dot that underwent TSIC with a 0V bias at 400 ˚C is included. Al deposited in contaminated thermal evaporator.**

From this data, it is evident that when there is no electrical contact between the Al and Si, as in the case of the Al dots, negligible ionic charge is introduced, even after a 30 minute anneal. However, when the Al covers the entire oxide surface, including a cleaved edge where it can make electrical contact with the exposed silicon, charge concentrations of ~1.3 to 1.5 x 10^{12} q/cm^2, which are sufficient for effective field effect passivation, are consistently introduced. What is particularly interesting is that when a sample with an Al dot is subjected to an enforced electrical connection between the silicon and aluminium, by means of TSIC with a 0 V bias, charge is introduced. The quantity of interface charge is very similar to that seen when a sample is annealed with the Al fully covering the oxide. This implies that an electrical contact is necessary between the Al contact and Si substrate in order for the charge to migrate to the interface.

It is worth noting here that once this relationship had been recognised, HF was used to etch the oxide from the corner of two quarter-wafer lifetime samples before aluminium deposition. This was to ensure a good electrical connection between the silicon substrate and the aluminium during the alneal. These samples achieved the highest effective lifetimes for enhanced alneal samples recorded and produced record passivation for a silicon surface. They are the Enhanced Alneal samples presented in Figure 22 of Chapter 4. The next section explains why this electrical connection may be significant.

5.3 MODEL FOR IONIC MIGRATION

It is clear that during the enhanced alneal, charge will only migrate to the SiO_2-Si interface when there is an electrical connection between the Si and the Al.

5.3.1 NO ELECTRICAL CONNECTION BETWEEN THE ALUMINIUM AND SILICON

The situation where the aluminium top surface is electrically isolated from the silicon is considered first. In this structure, the energy barrier for an ion to be injected from the Al-SiO_2 interface into the SiO_2 will be overcome when the necessary thermal energy is provided. As this occurs, a positive ion will enter the SiO_2, and migrate towards the SiO_2-Si interface, as shown in Figure 34 (b). Once situated at the SiO_2-Si interface, this ion has effectively charged a capacitor, with the oxide layer acting as the dielectric, and an electric field will build up as depicted in Figure 34 (a). The energy wells at both the Al-SiO_2 interface and the SiO_2-Si interface are shown here as the same depth for simplicity.

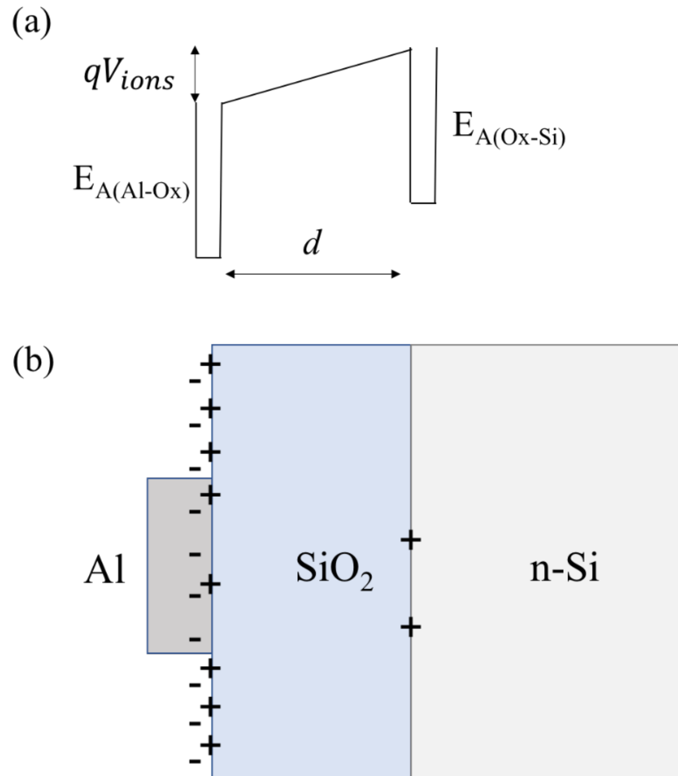

Figure 34. (a) Energy band diagram for a positive ion in a system of electrically isolated Al on top of SiO_2 and (b) schematic of charge location within an electrically isolated Al SiO_2-Si structure.

As shown in Figure 34 (a), this creates an electric field, V_{ions}/d, that opposes the migration of positive ions towards the SiO_2-Si interface. Although further ions may overcome the energy barrier to be injected into the SiO_2, they will be swept back to the Al-SiO_2 interface by the presence of this field. Therefore, many fewer ions will be able to migrate and provide field-effect passivation, which is evident by the lack of interface charge calculated from CV measurements of annealed MOS structures.

By varying the voltage applied during TSIC, it is possible to identify the bias, V_{ions}, at which no ions migrate. This was found to be between an applied bias of -0.4 and -0.6 V, see Figure 38. By using the potential difference across the oxide and the capacitance of the oxide, it is possible to calculate, using Q = CV, the maximum charge concentration that can migrate before a potential is developed which is sufficient to stop further migration of charge to the

interface. The capacitance per unit area for a 100 nm silicon oxide is 3.45×10^{-8} F/cm^2 and if we take the upper limit of -0.6 V. The maximum charge that can migrate under a floating MOS dot is calculated to be 1.3×10^{11} q/cm^2. In fact, in Figure 30 and Figure 31, the interface charge measured after annealing a floating dot is within this range, which supports the suggested model.

5.3.2 With an Electrical Connection Between the Aluminium and Silicon

In the alternative scenario, where an electrical connection exists between the Al and the Si, charge does migrate. Here, the electrical connection means that the system still acts as a capacitor but now with the two terminals shorted. Therefore, the movement of charge does not affect the electric field across the dielectric and the migration of charge will continue until the availability of ions at the Al-SiO_2 interface becomes limiting. This effect explains the difference in charge measured at the SiO_2-Si interface between the fully covered and TSIC Al dot specimens. It is noted that for very few, < 10%, of the Al dot specimens, significant charge was found after an anneal. A possible explanation for this is that in these specimens there was a pin hole or other means of weak electrical connection between the metal and the silicon substrate.

In order to develop a more complete model for the movement of ions in an electrically contacted Al-SiO_2-Si system, a further effect must be taken into account. This is the difference in work function between the metal and the silicon substrate, shown schematically in Figure 35. It shows that when the metal contact and the silicon substrate are electrically connected, there exists a field across the dielectric due to the difference in work functions.

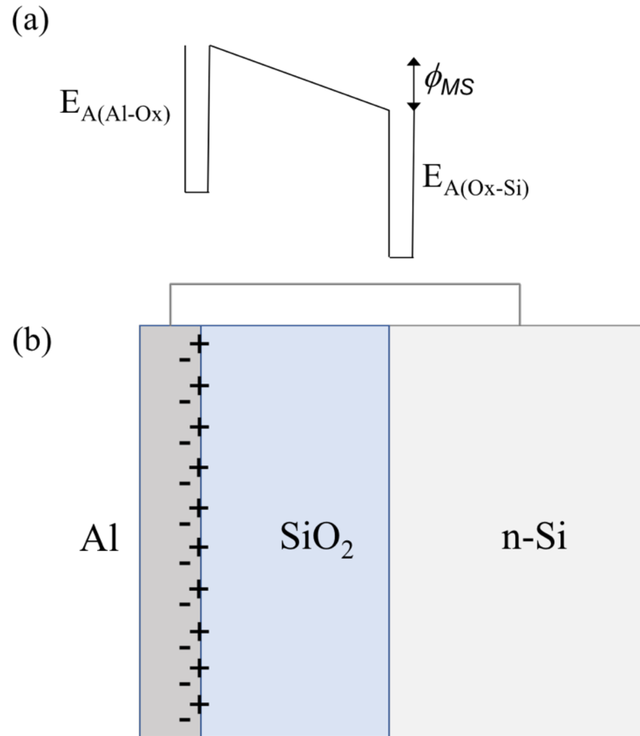

Figure 35. (a) Energy band diagram for a positive ion in this system of Al electrically connected to n-type 1 Ωcm Si and (b) schematic of electrically contacted Al-SiO_2-Si structure.

In the context of the alneal process: aluminium has a work function of 4.1 eV [161], while 1 Ωcm n-type Si has a work function of 4.32 eV, and when the two are in electrical contact, there exists a work function difference of 0.22 eV. In fact, a small error may occur in calculating this work function difference because it is possible for a dipole to emerge when two metals join, which can cause the work function difference to differ from the theoretical value. The presence of aluminium, which has a work function lower than the silicon substrate, sets up an electric field of 22 kV/cm across the oxide, encouraging movement of positive charge from the Al-SiO_2 interface to the SiO_2-Si interface. It is this internal field that is postulated to be responsible for the very rapid migration of ions to the silicon – oxide interface that is observed in an enhanced alneal. It is also noted that the work function difference between the silicon and aluminium, Φ_{ms}, would increase with more highly resistive n-type material, or with p-type. In order to asses this theory, a metal with a work function greater than that of the silicon was used as a comparison.

5.4 USING GOLD INSTEAD OF ALUMINIUM

In order to test the hypothesis that the work function difference between the metal and the silicon substrate was providing the driving force for ion migration, experiments were performed using Au instead of Al. Au has a larger work function than 1 Ωcm n-type Si, at 5.1 eV [162]., and thus the electric field it establishes in the dielectric will be of the opposite polarity to that when Al is used. Thus, the electric field direction would prevent ion migrating to the SiO_2-Si interface. To overcome any uncertainty regarding the source of the ionic contaminants in the thermal evaporator, a fraction of a monolayer of KCl was thermally evaporated onto the oxide surface, as described in the Chapter 3. This ensured an ample supply of ionic charge was present and was used for both the anneal and TSIC samples reported below.

5.4.1 ANNEAL USING GOLD AND ALUMINIUM

Gold or aluminium were deposited on top of the deposited KCl to fully cover the oxide surface of the 1 cm^2 1 Ωcm n-type FZ samples. For the gold evaporation, a tungsten boat was used instead of a tungsten coil. These samples were then annealed on the hot plate at 400 ˚C for varying lengths of time. After this, the aluminium was removed using commercial etchant as previously, and the gold was removed using aqua regia (1:3 nitric:hydrochloric acids). The back oxides were etched off using HF and an ohmic contact to the silicon was created using InGa and silver dag. The interface charge concentrations from Hg-CV measurements for the two different metals, annealed for different lengths of time, are shown in Figure 36. From this, it is evident that when Au is used, no charge is introduced into the oxide layer, whereas when Al is present, significant quantities of charge are measured at the Si-SiO_2 interface after the anneal.

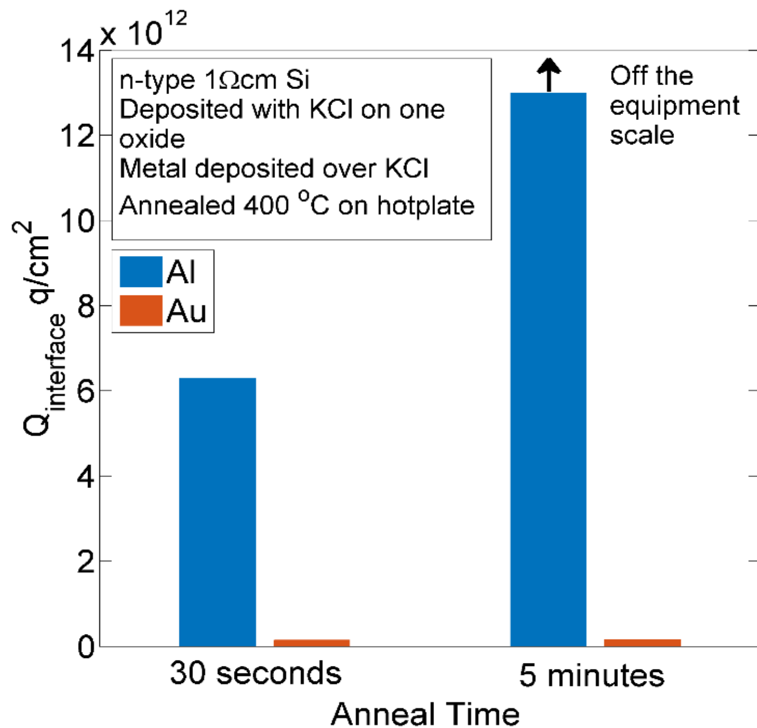

Figure 36. Interface charge concentration for anneals of 30 seconds and 5 minutes at 400 °C on samples with KCl deposited on the oxide surface using either aluminium (blue) or gold (orange) during the anneal. Aluminium deposited to cover the full surface, and edge of the silicon sample.

In Figure 36, when aluminium is used, charge is present at the interface after an anneal of only 30 seconds. A five minute anneal at this temperature increases the quantity of interface charge to be over the equipment measurement capability. However, the interface charge was not seen to increase when gold was used, even after five minutes; instead it remained in the order of 10^{11} q/cm^2. This indicates that either the energy barrier for the ions to leave the Au-SiO_2 interface is greater than that of the Al-SiO_2 interface, or that the field across the SiO_2 is preventing their migration to the interface. In order to test whether it was possible to inject K into SiO_2 from the Au-SiO_2 interface once the Au-Si work function difference was overcome, TSIC samples were fabricated and a voltage applied to increase the potential difference across the oxide. Again, these samples were purposefully contaminated with K to guarantee an ample supply of K, and both Au and Al were used as top contacts for the MOS structures.

One must note that for the specimens shown in Figure 36 and Figure 37, K was introduced on purpose. Therefore, in Figure 36, the magnitude of interface charge when an aluminium layer is used is one to two orders of magnitude greater than for the samples in Figure 33, where no intentional ion deposition occurred.

5.4.2 TSIC USING GOLD AND ALUMINIUM

The MOS structures were fabricated on 1 Ωcm n-type FZ silicon with KCl salts deposited before the metal front contact. After the TSIC experiment, the total migrated charge concentration was calculated from integrating the recorded current as described in Chapter 3. The migrated charge, assumed equivalent to the interface charge, is plotted against TSIC voltage applied to the top contact, in Figure 37. This shows that ions will migrate to the Si-SiO_2 interface when gold is the top contact metal, however, a bias greater than zero is necessary.

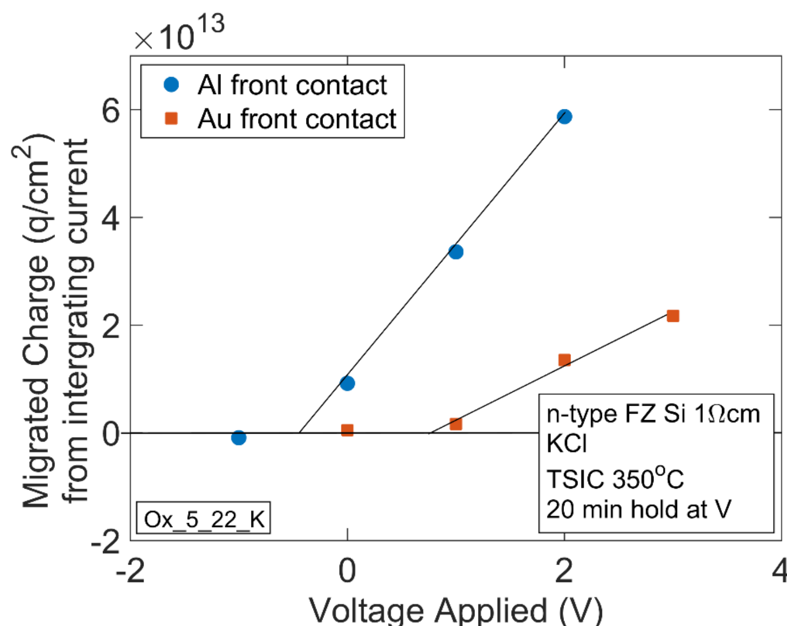

Figure 37. Concentration of migrated charge, calculated by integration of TSIC current, against voltage applied to top contact during TSIC for samples deposited with KCl salts, using aluminium or gold contacts. The error in the measurement of charge is of the order of 10^{12} q/cm^2 [109]**. Lines are a guide to the eye.**

When the 0 V bias condition of Figure 37 is considered, for the Au contact, negligible charge is migrated after 20 minutes, whereas for the Al contact, a significant quantity of charge migrates (>1 x 10^{13} q/cm^2), as is the case for the (unbiased, but electrically contacted) anneals shown in Figure 36. Although no charge is introduced when gold is used in the zero-bias condition, it is possible to migrate the K ions to the Si-SiO_2 interface when a larger voltage is applied. Extrapolation of the migrated charge versus bias voltage to zero migrated charge allows a threshold bias voltage to be identified. The intercept for an Al-SiO_2-Si structure would indicate that ions migrate at bias voltages above -0.4 V, whereas the Au intercept demonstrates that a bias greater than + 0.8 V is necessary before the K ions migrate, a difference between the two metals of 1.2 V. This difference is very similar to the work function difference between aluminium and gold. Work functions vary depending on lattice orientation and range from 4.06 to 4.28 eV for Al [161] and 5.1 to 5.5 eV for Au [162]. It must be noted that as Au is not very adhesive to SiO_2, the area used to calculate the charge concentration may have introduced a slight error. This may have resulted in a slight under-estimation of the interface charge concentration at a given TSIC bias.

5.5 TSIC WITH VARIED TEMPERATURE AND BIAS

TSIC processing was carried out on MOS structures fabricated with the top aluminium dot deposited in the contaminated thermal evaporator. No purposeful ions were deposited. The back oxide was removed with HF and contacted with thermally evaporated Al. The TSIC processing was conducted with a temperature ramp to either 200 °C or 400 °C, with a bias between - 0.6 V to + 5 V applied. Samples were held at the target temperature for 25 minutes in an attempt to allow the ionic charge concentration to saturate. Unfortunately, the TSIC

current data is extremely noisy and therefore the current-time curves cannot be analysed to confirm if the ionic migration had ceased. It is likely, from the TSIC curve of Figure 26, that the charge had saturated after 25 minutes for the TSIC processes at 400 °C. However, there is uncertainty with regard to the processing at 200 °C, however, it is included for completeness. After TSIC processing, the interface charge was measured using the Al dot and probe station CV. This is shown against TSIC bias in Figure 38.

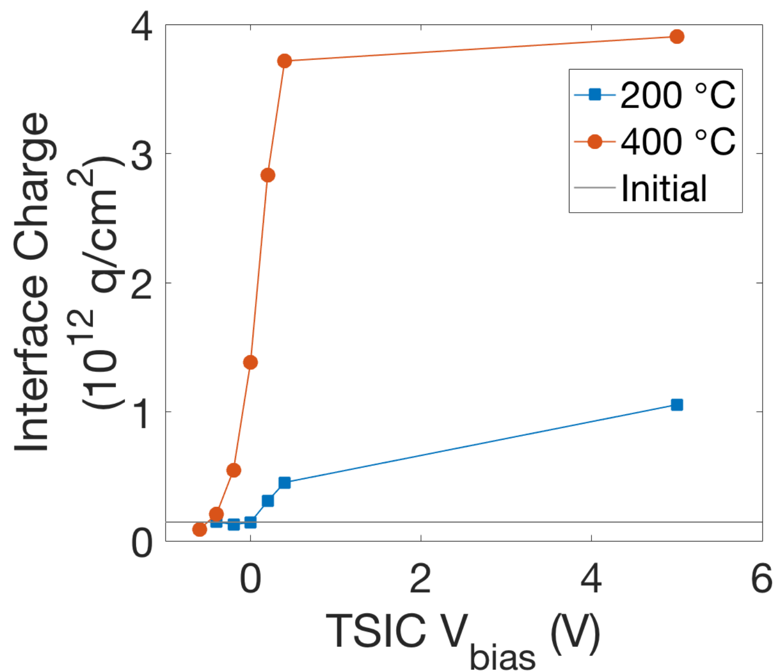

Figure 38. Interface charge from CV measurements after TSIC under various gate biases with the temperature ramping to 200 °C or 400 °C. Samples were held at this temperature for 25 minutes before they were cooled with the voltage still applied. Al dot deposited in contaminated thermal evaporator, all samples were deposited with Al in one batch. The average initial interface charge concentration is given by the grey horizontal line. Material used was 1 Ωcm n-type FZ Si with a 100 nm thermal oxide.

Figure 38 shows that at 400 °C a linear relationship exists between bias applied during TSIC and interface charge concentration, until the interface charge concentration plateaus at what is assumed to be the contamination limit. This data at 400 °C, along with that in Figure 37, was used to identify the cross over voltage at which no charge would migrate through the oxide layer to the SiO_2-Si interface.

The results presented in this chapter emphasise the necessity of an electric field across the oxide during the enhanced alneal in order to achieve rapid migration of ionic species. For industrial application, one wishes to avoid the use of a metallic contact. Therefore, it is important to study the air-SiO_2 interface and the mechanisms by which a bias can be applied to that without a metallic contact, which is the focus of Chapter 6.

5.6 CONCLUSIONS

In this chapter it is concluded that the ionic species responsible for the high-quality passivation of the enhanced alneal, are only introduced when there is an electrical contact between the silicon and the aluminium layer deposited on top of the SiO_2. This electrical connection is believed to facilitate the injection and migration of ionic species due to the work function difference of Al and Si, which produces an electric field across the Al-SiO_2-Si system. To test this theory, a negative voltage was applied across the oxide, to compensate the built-in work function difference. This resulted in no charge migration. An alternative test was achieved by purposefully depositing ionic species onto the oxide surface to ensure an adequate supply and using gold as the top metal contact as it provides a work function difference which opposes the migration of positive ions to the SiO_2-Si interface. When gold was used, either by annealing with an electrical contact or TSIC with the bias set to 0 V, no interface charge resulted, thus supporting this theory. If TSIC processing was applied to an Al-SiO_2-Si sample, purposefully deposited with ions, a linear relationship between bias potential and interface charge was seen. This discovery is of use in the next chapter where the findings from the work on the enhanced alneal are employed to assist the development of a commercial technique for depositing and migrating ionic species.

CHAPTER 6
TOWARDS INDUSTRIAL ION INTRODUCTION

In previous chapters it has been concluded that ionic field effect passivation (FEP) can produce outstanding minority carrier lifetimes. However, the method by which this was achieved in previous chapters was suitable at the laboratory level, where there is less time pressure, but it was not suitable commercially. This chapter applies two techniques by which ions for ionic FEP can be introduced into a dielectric in a way that is suitable for large-scale deployment.

Ion introduction is most commonly a two-stage process: ion deposition and ion migration. There are two important criteria when selecting a method to introduce ionic charge into a dielectric. First, the ion precursor must be deposited in uniform, sub-monolayer concentrations to avoid salt crystal formation. Second, the precursor deposition and ion migration techniques must be scalable processes, which can be carried out quickly.

In this chapter, there will be an initial review of the relevant literature, highlighting the challenges faced. This will be followed by an analysis of different ion precursor deposition techniques and the characterisation of a scalable, rapid ion migration mechanism that is suitable for inline processing. Experiments are conducted on 100 nm oxide material for ease of characterisation. However, the findings of this chapter should be applicable to the thin thermal oxides < 10 nm used in industry. While this chapter focusses on potassium as the ionic species, the next chapter will consider alternative ions.

6.1 Literature Review of Introduction of Ions to Silicon Dioxide

Metal diffusion into SiO_2 has been of significant interest because of the potential impact on MOSFET performance. In 1965, Yamin [163] reported the diffusion of ionic species in SiO_2 using various metal contacts to produce metal-oxide-silicon (MOS) structures. A field was then applied at an elevated temperature for thermally stimulated ionic conduction (TSIC) processing. On cooling, migrated charge of the order of $10^{12} – 10^{14}$ q/cm^2 was calculated from the integration of current data. Yamin proposed that the charge was likely to be caused by sodium, which was known to drift through silicon dioxide as an ion from the research done by Snow et al. [153]. Hickmott [150] discovered that the metal contact also dictated the temperature at which Na^+ ions began to drift through the oxide. Later, potassium was also found to diffuse through silicon dioxide as a charged species [151] at a higher temperature than Na.

In order to study this further, Kerr [106] developed a salt precursor deposition technique of thermal evaporation. Bonilla [98] found, in adopting this process, that if the concentration of salt in solution was too high (> 10^{14} q/cm^2), salt crystals could form on the oxide surface. These salt crystals are believed to prevent the dissociation of the ionic species and thus the injection of the ions into the silicon dioxide. Therefore, the salt concentration must be kept below the concentration at which salt crystals are formed.

All of these investigations used TSIC as the migration mechanism, which is not compatible with large-scale production or effective lifetime measurements as the processed area is too small. Without effective lifetime measurements, it was unclear whether or not the presence of these ions at the interface would improve the silicon surface passivation. An alternative

migration method to TSIC processing is therefore required. Initially, diffusion was tested by Bonilla [61] at temperatures ranging from 400 to 500 °C, but the introduction of ions was slow, as shown in Figure 39. For a suitable quantity of Na or K to be diffused, ~ 2 x 10^{12} q/cm^2, required over 30 minutes at 400 °C. Even at 450 °C the diffusion was found to take 3 to 5 minutes.

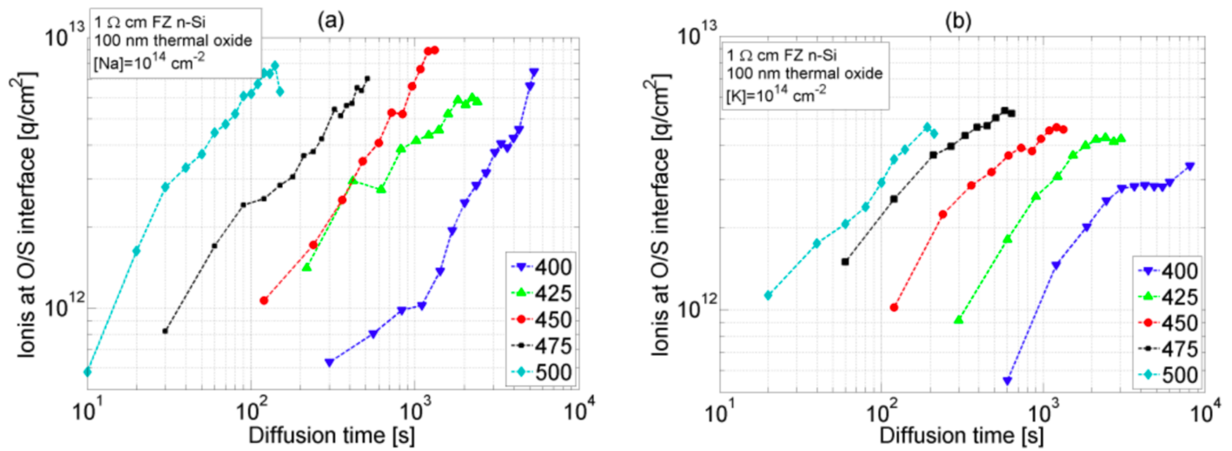

Figure 39. Concentration of (a) sodium and (b) potassium ions migrated to the oxide-silicon interface as a function of anneal time for a range of temperatures. After [61]**.**

These lengths of anneals are not appropriate in industry, where quicker processes at lower temperatures are more favourable. Manufacturers aim to have a process rate of 1 wafer per second [96], so the slower the process, the larger the footprint of the equipment required, making it more expensive.

In order to reduce the time taken for ion migration, Bonilla et al. [105] used corona discharge to incorporate a field component to the ionic migration. This means that ions not only diffuse but drift from the air-SiO_2 interface to the SiO_2-Si interface. Throughout this thesis, this is referred to as field-assisted ionic migration. The process involves the deposition of a quantity of corona charge onto the dielectric surface, which is then annealed. Bonilla et al. [105] found this migration technique to be successful and it was noted that the effective lifetime

of the samples increased to a greater value when field-assisted migration was employed than when pure diffusion was used.

From effective lifetime measurements, it became evident that the presence of ionic charge at the interface was improving the minority carrier lifetime by introducing an aspect of field effect passivation [105]. However, Bonilla also noted that as the concentration of interface charge increased above a certain point, the effective lifetime of the sample began to decrease again [61]. This is thought to be due to the ionic concentration compromising the chemical passivation.

In order to be commercially viable, effective lifetime improvements from ionic FEP must be stable. The stability of potassium ions at the interface was monitored by Bonilla [62] and the decay time constants of the effective lifetime, under standard laboratory conditions, was found to be in excess of 45 years, which is compatible with commercial solar panels which are designed to operate for between 30 to 40 years. However, no industry-appropriate ionic deposition technique had been identified and field-assisted ionic migration had not been well characterised.

The rest of this chapter focuses on initial experiments investigating scalable deposition techniques for ion precursors in conjunction with field-assisted ionic migration.

6.2 Development of an Industrially Compatible Technique

As discussed previously, techniques suitable for large-scale manufacture must be fast and scalable with a throughput of 1 wafer per second. There are two important criteria when considering a method to introduce ionic charge into a dielectric. First, the precursor must be deposited in uniform, sub-monolayer concentrations, to avoid crystal formation. Second, the technique must be both rapid and scalable. In this chapter, industrially applicable techniques for introducing ionic FEP are outlined and studied. The deposition of ion precursors is carried out through spin or spray coating, (developed respectively by Du [107] and Bonilla in the Oxford Semiconductor group), which are both widely used industrial processes. The deposition process is followed by field-assisted ionic migration where corona charge is used to provide the electric field. Corona charge deposition is a widely used technique being applied, for example, in laser printers [54, 164]. For these experiments 200 µm thick, 1 Ωcm n-type FZ silicon with a 100 nm thermal oxide grown at Fraunhofer ISE was used. The processing methodology for the specimens is shown in Figure 40.

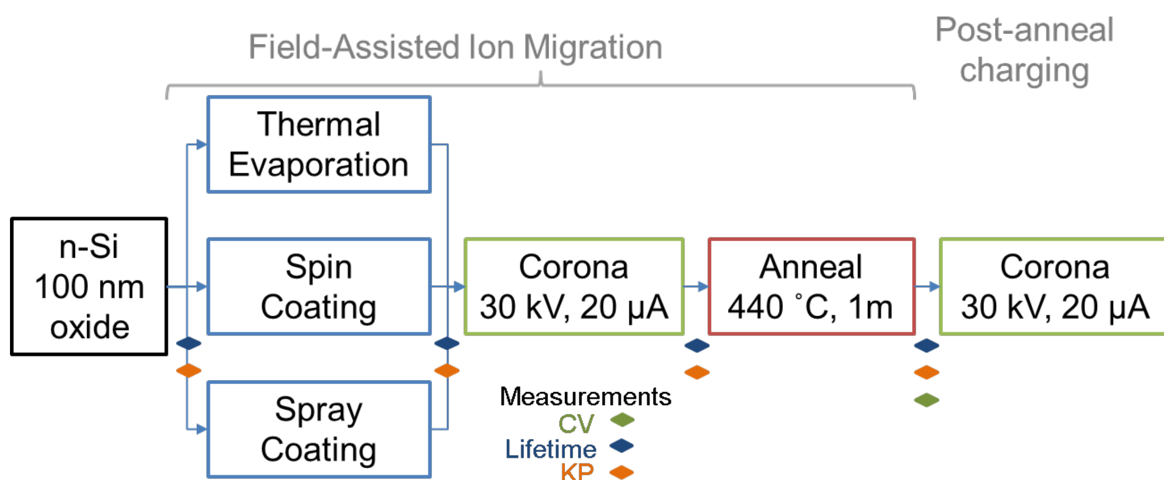

Figure 40. Experimental process flow chart

6.2.1 IONIC PRECURSOR DEPOSITION

Spin and spray coating, were compared to the well understood laboratory deposition technique mentioned in section 6.1, thermal evaporation. For thermal evaporation of ions [62], DI water was the solvent. For spin coating, KCl was dissolved in 25% H_2O, 75% IPA by volume. 1 ml of 4.4 x 10^{-5} mol/L KCl solution was pipetted on to the sample once the spinner was at 2000 RPM. Spray coating was conducted at USI, Haverhill MA, using their PRISM bench-top ultrasound coating system. A solution of 3 x 10^{-4} mol/L KCl in 10% H_2O, 90% IPA by volume was used to give a 11 μm thick layer.

From section 6.1, it is clear that relying on pure diffusion to introduce ions into a dielectric, is a slow process, unsuitable for industrial use. For that reason, corona induced field-assisted ion migration was used, as described in section 6.1. Corona discharge is deposited on the oxide surface, after the ion precursor, this is followed by a hotplate anneal, between 250 – 450 °C.

The migration of ions, and their ability to provide surface passivation, was characterised by the effective lifetime which was measured throughout the processing sequence, as indicated in Figure 40. After ionic migration, corona charge was added to some samples to optimise the FEP and thus to identify the maximum achievable effective lifetime. This additional corona charge was used to determine whether there had been any change in the chemical passivation by comparing the achieved effective lifetime to that of a corona charged control that had not undergone ion deposition or field-assisted ion migration.

It is important to note that an appropriate deposition technique must not only be suitable for large-scale processing, but must allow controlled, sub-monolayer deposition of ions and avoid the formation of crystals which prevent the release of ions into the dielectric. Three techniques were used for ion deposition. These were: thermal evaporation, which is a laboratory technique, spin coating and spray coating.

6.2.1.1 THERMAL EVAPORATION

Thermal evaporation was used to deposit a well-defined sub-monolayer concentration of KCl on the oxide surface. This technique was taken as the baseline to evaluate the new deposition techniques. The effective lifetimes and SiO_2-Si interface charge concentrations with thermally evaporated and field-assisted migration of K^+ ions are shown in Figure 41.

It is evident that this technique provides very effective FEP, as indicated by lifetimes increasing from 100 μs to ~ 2100 μs. The amount of interface charge produced in different specimens was varied by changing the amount of corona charge deposited on the oxide surface. The resulting interface charge ranges from 1.5 to 2.8×10^{12} q/cm^2, which includes values of dielectric charge necessary for high-quality FEP as modelled in [97] and as measured in the Enhanced Alneal results presented in Chapter 4. Unexpectedly, the effective lifetimes produced with these quantities of ionic interface charge are all similar, despite indicating an increase in FEP caused by the increasing interface charge. This is investigated further by corona charging the samples.

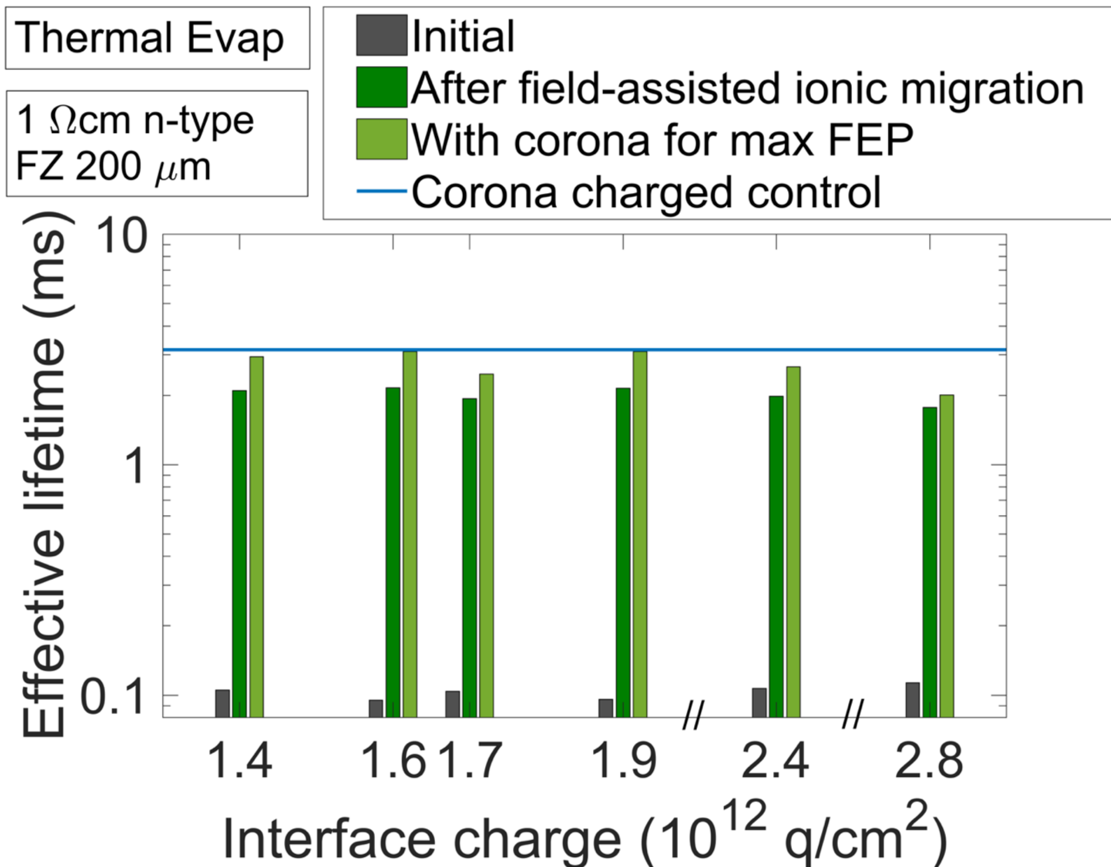

Figure 41. Effective lifetimes before and after field-assisted ionic migration with thermally deposited KCl as a function of interface charge concentration. Effective lifetime after field-assisted ion migration, with the addition of surface corona charge for maximum FEP. The horizontal line represents the effective lifetime of an as-received sample with surface corona charge for maximum FEP. FZ n-type Si, 1 Ωcm, 200 µm, 100 nm thermal oxide. The migration anneal was performed at 450 ˚C for 1 minute.

After processing, the samples were corona charged to maximum FEP. Most of the samples, with the addition of corona charge, reached a comparable effective lifetime to that of the corona charged control. This indicates that the chemical passivation had not been compromised, apart from for the sample with the highest concentration of interface charge. For this sample, the effective lifetime with maximised FEP from the addition of surface corona charge, is lower than that of the control. This may indicate that, at these high concentration, ionic species at the SiO_2-Si interface may be damaging the chemical passivation of the surface. This is in agreement with results in [61, 105]. Due to the size of the samples, it is also possible that edge recombination is limiting the effective lifetimes of

the FEP passivated samples with the addition of corona charge [148]. The effective lifetimes and interface charge concentrations presented in this section are now compared to those produced by the techniques with industrial potential.

6.2.1.2 SPIN COATING

Oxidised silicon samples were spin coated with KCl precursor ions. The effective lifetime and interface charge after field-assisted migration for these samples are shown using various concentrations of surface corona charge in Figure 42.

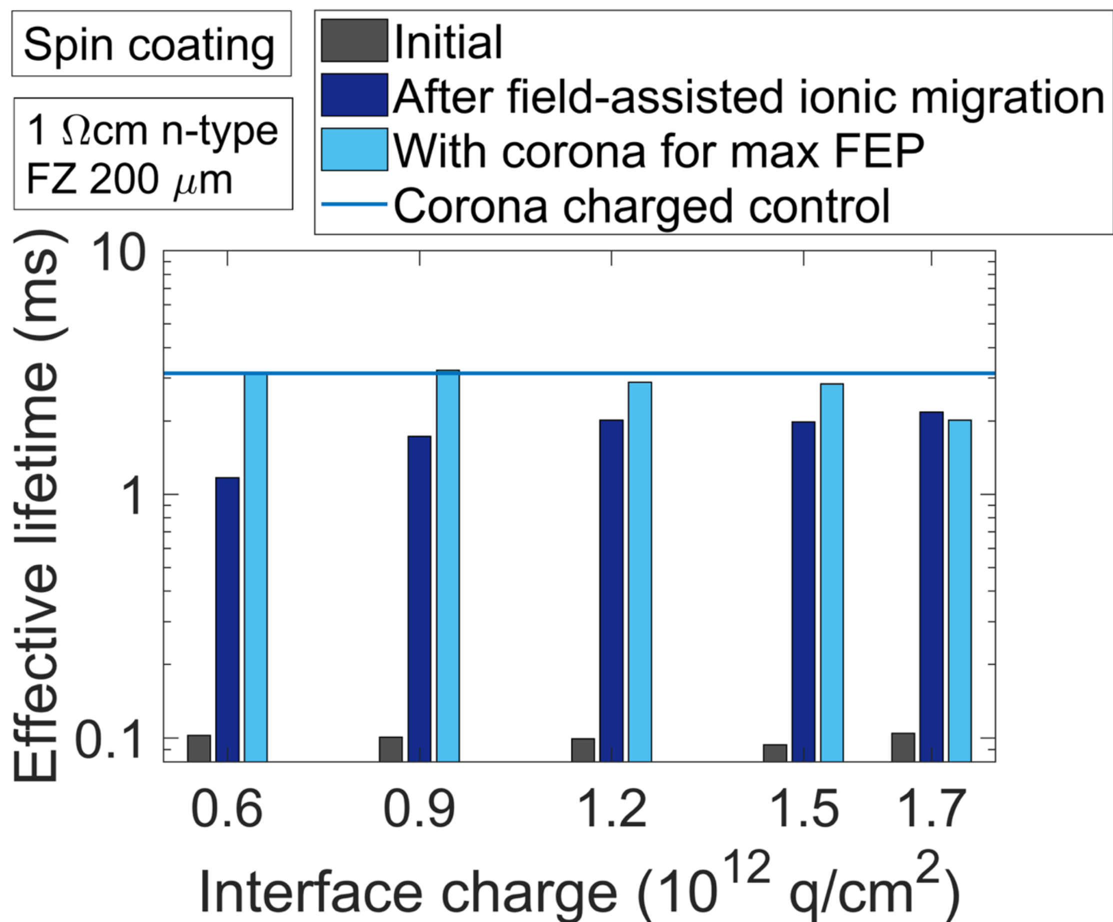

Figure 42. Effective lifetimes before and after field-assisted ionic migration with spin coated KCl as a function of interface charge concentration. Effective lifetime after field-assisted ion migration, with the addition of surface corona charge for maximum FEP. The horizontal line represents the effective lifetime of an as-received sample with surface corona charge for maximum FEP. FZ n-type Si, 1 Ωcm, 200 μm, 100 nm thermal oxide. The migration anneal was performed at 450 ˚C for 1 minute.

The presence of interface charge, demonstrated in Figure 42, shows that spin coating deposition is capable of delivering the precursor in sub-monolayer concentrations and that the formation of salt crystals on the oxide surface is suitably avoided.

In Figure 4, lower concentrations of interface charge were introduced compared to Figure 3. The purpose of this was to find the interface charge concentration that provides the best surface passivation, and therefore best effective lifetime. At the given interface charge concentrations, the effective lifetimes increase continually, reaching 2100 μs at 1.7×10^{12} q/cm^2, a very similar lifetime to that of the thermally evaporated sample with a similar interface charge. This effective lifetime is equivalent to the SRV improving significantly from 101 cm/s to 3.3 cm/s and gives a J_{0s} of 8.4 fA/cm^2.

After field-assisted ionic migration, the samples are corona charged to maximise FEP. For interface charge concentrations $< 1.5 \times 10^{12}$ q/cm^2, the effective lifetimes are similar to that of the control, indicating that ionic FEP is effective and that there is no substantial damage to the chemical passivation. However, at a charge concentration of 1.7×10^{12} q/cm^2, the effective lifetime with the addition of corona charge for maximum FEP does not improve. This is unusual because, for the thermally evaporated sample in Figure 41 with a comparable interface charge concentration, a small improvement in effective lifetime is visible with additional FEP. This suggests that the lower effective lifetime in Figure 42 may be unique to the sample. It is possible that the as-grown chemical passivation of this sample, which came from a different wafer to the other samples in Figure 42, is lower. This could have been limiting the effective lifetime.

From Figure 42, it is clear that spin coating as an ion precursor technique is capable of providing high quality surface passivation.

6.2.1.3 Spray Coating

Although spin coating is an effective technique to deliver precursor ions to the oxide surface, spray coating has the potential to be a faster, inline process. Samples were spray coated with KCl using a high performance ultrasonic coating system. K+ ions were subsequently introduced into the oxide using field-assisted migration. TSIC measurements in a MOS structure confirmed that a concentration of 10^{13} K^{+} ions/cm^2 had been sprayed on to the SiO_2 surface as a lower bound. It is noted, however, that the Al-SiO_2 interface possesses different characteristics to the air-SiO_2 interface. Effective lifetimes and interface charge concentration after migration are shown in Figure 43. Due to limited material, only one deposited corona charge concentration was used.

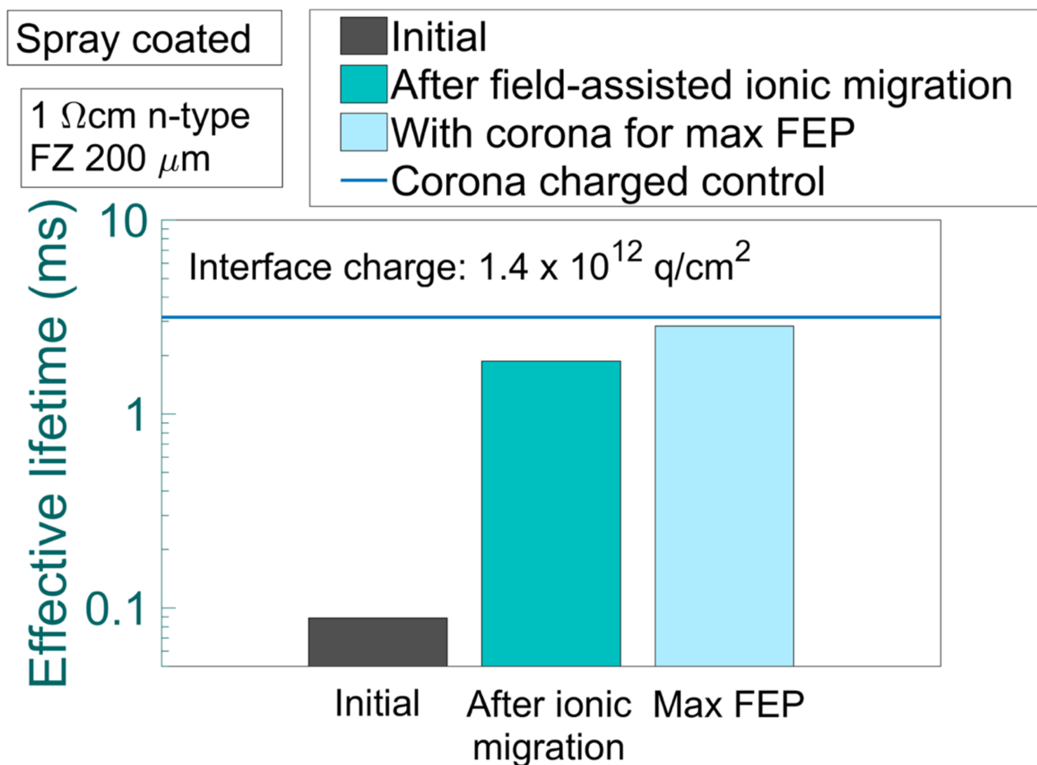

Figure 43. Effective lifetimes before and after field-assisted ionic migration with spray coated KCl. Effective lifetime after field-assisted ion migration, with the addition of surface corona charge for maximum FEP. The horizontal line represents the effective lifetime of an as-received sample with surface corona charge for maximum FEP. FZ n-type Si, 1 Ωcm, 200 µm, 100 nm thermal oxide. The migration anneal was performed at 450 ˚C for 1 minute.

It is evident that spray deposition is also effective at delivering the precursor to the oxide film without the formation of salt crystals. Field-assisted ion migration is successful, improving surface passivation and giving an effective lifetime of 1870 µs, equivalent to an SRV of 4.1 cm/s and a J_{0s} of 8.6 fA/cm^2. For a spin coated sample with the same interface charge the effective lifetime is ~ 2000 µs, which is comparable.

6.2.1.4 DISCUSSION

As seen in Figure 41 and Figure 42, the effective lifetimes achieved by spin and spray coating are comparable to one another, and to those from thermal evaporation of the precursor, which is promising for industrial application.

Figure 41 showed that as the concentration of ionic species at the SiO_2-Si interface increased, the effective lifetime plateaued with interface charge concentrations exceeding 1.9×10^{12} q/cm^2. It is possible this could be due to increased concentrations of ionic charge at the interface decreasing the chemical passivation.

In order to assess how industrially-suitable a technique for ionic field effect passivation is, the uniformity of ionic introduction must be considered. The interface charge concentration may vary locally if the deposition technique results in the formation of salt crystals anywhere on the oxide surface. Where salt crystals form, it is unlikely that the ionic species of interest will dissociate and be available for injection into the SiO_2. The uniformity of the interface charge concentration was measured by cleaving 3×3 cm^2 lifetime samples into ~ 16 pieces. These samples were then prepared for Hg-CV measurements. Half of the samples were prepared to measure one surface, and the other half of the samples were prepared to measure the other surface. The variation in interface charge measurements across both surfaces in each sample is presented in Figure 44, for all three deposition techniques. The average

interface charge is different for each sample due to the field-assisted ionic migration parameters that were used when processing the sample.

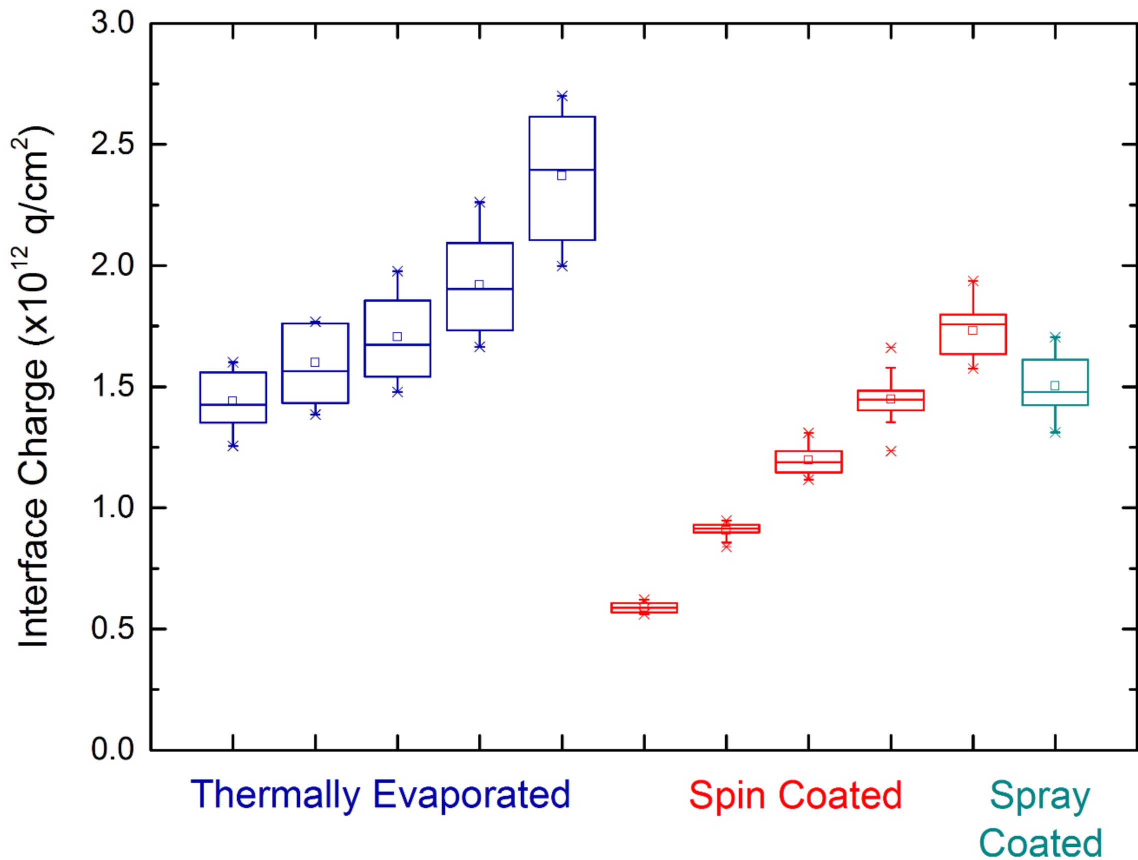

Figure 44. Box plots to show statistical data for interface charge concentration. All three deposition techniques shown. Five different average interface charge concentrations are displayed for thermal evaporation and spin coating to show the statistical distribution using different field-assisted ionic migration parameters, resulting in differing average interface charge concentrations. The interface charge concentrations are measured across both surfaces of 3 x 3 cm^2 samples. Lines of the box represent the median, lower and upper quartile values, indicates the mean and x marks the minimum and maximum values.

From the data in Figure 44, it is clear that spin coating and spray coating ion precursor deposition techniques provide very uniform interface charge concentrations. These two techniques appear to be more uniform than the thermal evaporation technique. This is extremely promising for a commercial technique, where uniformity and repeatability are of paramount importance.

6.3 FIELD-ASSISTED MIGRATION

Spin coating and spray coating offer promising, commercially-suitable techniques for ion precursor deposition. However, the deposition is not the only aspect to introducing ionic field effect passivation. A commercially suitable technique to migrate the ions into the dielectric films is also required.

In the previous section, corona-induced field-assisted ionic migration, as described in section 3.7.3, was employed. The process has been shown to be an effective technique to introduce ionic charge to the SiO_2-Si interface from the oxide surface and is preferable to simple annealing due to time savings. Instead of a simple anneal, corona induced field-assisted ionic migration enables ions to migrate in a more commercially appropriate time-frame by incorporating a drift component.

For commercial applications, it is important to identify any migration characteristics that might affect the migrated ion concentration, as well as to understand how quickly charge can be introduced.

6.3.1 DEPENDENCE OF INTERFACE CHARGE ON INITIAL SURFACE CORONA CHARGE

It is postulated that the effect of surface corona charge concentration on the resulting concentration of interface charge is as follows: immediately after ionic precursor deposition, the sample has a neutral surface and in-diffusion of the K^+ ions is very slow, even at 450 °C [61]. The diffusion is slow because when a K^+ ion enters the SiO_2, it leaves behind a Cl^- on the oxide surface. This negative charge creates an electric field that opposes the migration of the K^+ to the SiO_2-Si interface and instead encourages the K^+ to return to the SiO_2 surface. This will significantly reduce the rate of charge migration to the SiO_2-Si interface as injected

charges will only be likely to migrate when the Cl^- surface ions are neutralised by undefined mechanisms, potentially charge transfer with passing molecules in the air or dust particles.

In the instance of field-assisted ionic migration, after the initial deposition of the ionic precursor, leaving a neutral surface shown in Figure 45 (a), corona charge is deposited on the oxide surface. The presence of this charge creates an electric field across the oxide layer that encourages the migration of positive ions away from the oxide surface to the SiO_2-Si interface, as shown in Figure 45 (b). This ensures that once the K+ has overcome the energy barrier to enter the SiO_2, the ion rapidly moves to the SiO_2-Si interface. As each K^+ ion successfully leaves the surface and migrates to the SiO_2-Si interface, the net surface charge is reduced and so is the electric field across the oxide. Once the total number of K^+ ions that have reached the SiO_2-Si interface is equal to the deposited surface corona charge, the enhancement effect is removed, as shown in Figure 45 (c), and the system returns to the very slow diffusion process.

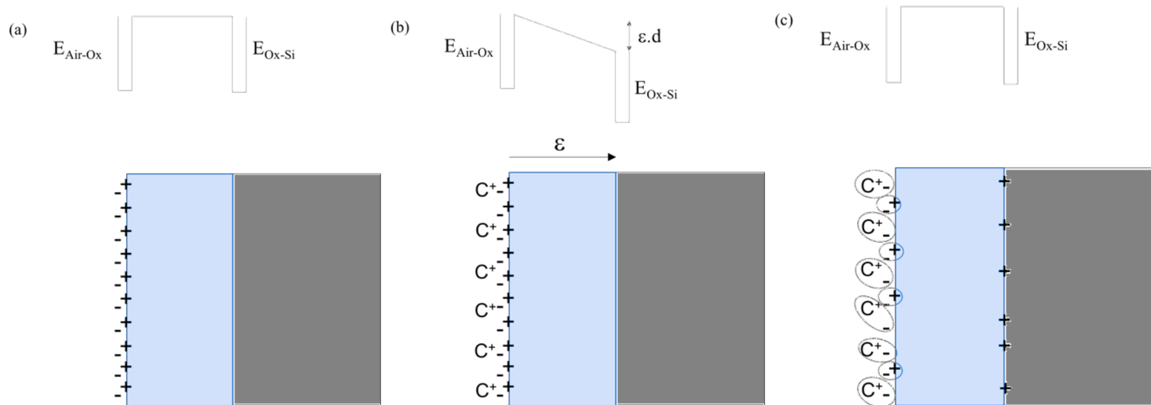

Figure 45. Schematic of sample structure and energy diagram for a positive ion (a) after ionic precursor deposition, (b) after corona charge deposition and (c) after ion migration.

In order to test this hypothesis and evaluate interface charge dependence on concentration of deposited surface corona charge, samples of approximately 1 x 1 cm^2 were cleaved from samples that had been deposited with ionic precursor, either by thermal evaporation or by spin coating. These small samples had various quantities of corona charge deposited. The

samples were then annealed on a hot plate at 450 °C for 60 s. After this time the surface charge concentration was negligible. Carrier lifetimes were not recorded due to the sample size. The interface charge concentration as a function of corona charge measured by Hg-CV is shown in Figure 46 for different precursor depositions. The data show a linear relationship between interface charge and corona charge.

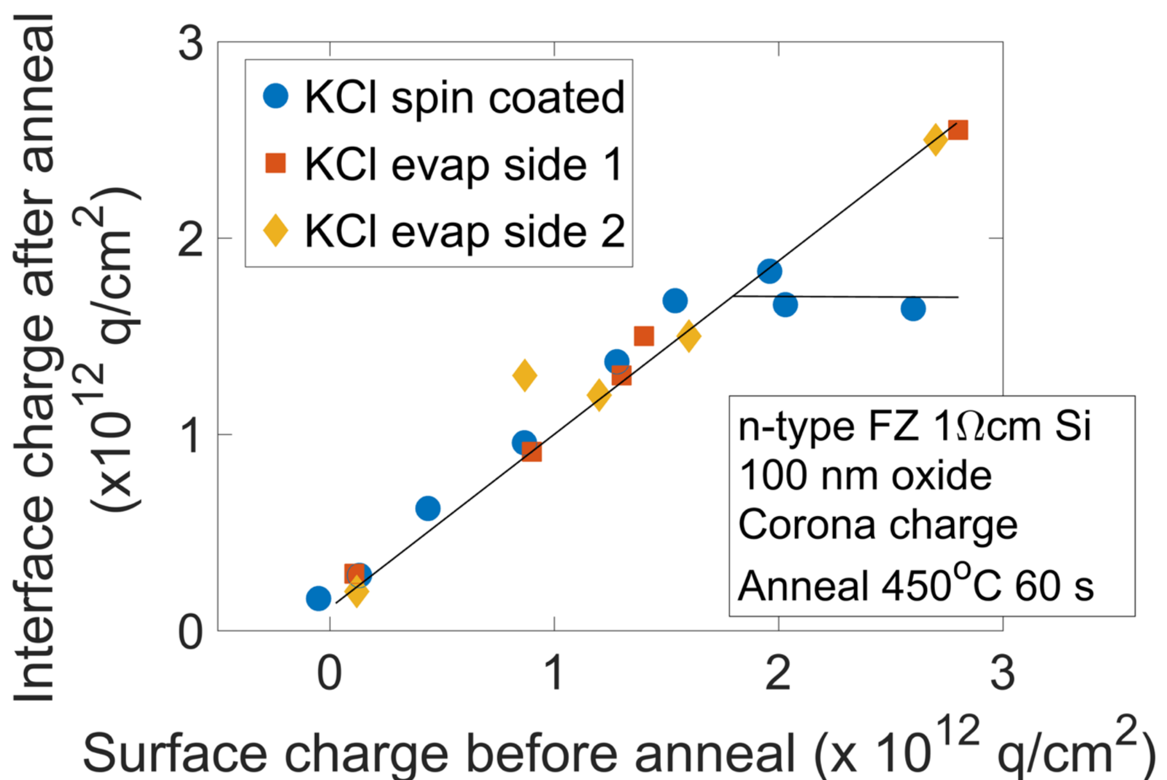

Figure 46. Interface charge concentration dependence on surface corona charge concentration before migration anneal. Shown for various precursor depositions using both thermal evaporation and spin coating techniques.

From Figure 46 it is clear that the hypothesis is supported as there is an almost one-to-one relationship between the surface corona charge concentration before the migration anneal and the interface charge concentration measured afterwards. The results deviate only slightly from a true one-to-one relationship. This could be due to corona charge leakage or neutralisation (by mechanisms other than movement of the K^+ ions) during the anneal or to insufficient anneal time, meaning that the process is incomplete because a small net

concentration of positive charge was still present on the oxide surface. For the spin coated sample, the interface charge concentration plateaus at ~ 2 x 10^{12} q/cm^{-2}, which is close to the concentration initially deposited.

This linear relationship shown in Figure 46 allows the concentration of interface charge to be controlled by the concentration of corona charge deposited before the anneal. This implies that the interface charge can be controlled in two ways: either by the amount of corona charge deposited, if there is a surplus of ions on the surface, or by the concentration of ions deposited if a surplus of corona charge is available.

6.3.2 ANNEAL TEMPERATURE AND TIME

Having established the relationship between surface corona charge concentration and resulting interface charge, it was necessary to investigate the relationship between anneal parameters and interface charge, and more importantly its surface passivation. One of the main drivers for investigating this is that, industrially, low temperatures and fast processes are preferable because they decrease costs by requiring lower cleanliness standards and allowing greater throughput.

Samples of 3 x 3 cm^2 were deposited with thermally evaporated KCl, deposited with corona discharge and annealed at four temperatures: 250 ˚C, 300 ˚C, 350 ˚C and 450 ˚C for anneal times of 2, 120 and 180 seconds. It is noted that for the two-second anneals the experimental parameters of time and temperature are subject to large measurement errors due to the difficulty in controlling the experiment for such short time periods. Thus, for the two-second anneals the time and temperature should be treated as indicative values only due to the initial reduction in temperature, as described in Chapter 3. As a control, an as-received oxidised sample was deposited with corona and this was annealed for 3 minutes at 300 °C. A set

quantity of corona charge was deposited on the surfaces of all samples prior to annealing to give a surface charge concentration of 1.9 x 10^{12} q/cm^2. This concentration was selected because it was shown in Figure 46 to cause an interface charge of ~ 1.7 x 10^{12} q/cm^2, which in Figure 42 was shown to produce the highest effective lifetime. This quantity of interface charge has also been shown to provide outstanding effective lifetimes and FEP in the enhanced alneal [108].

During the lower temperature anneals, not all the surface corona charge dissipated during the anneal, so immediately after processing some corona remained on the oxide surface. This is in line with the suggested model, as the rate of neutralisation of the surface corona charge will be limited by the rate of injection of the K^+ ionic species into the oxide layer at lower temperatures. If left in place, the residual surface corona charge would have provided an element of FEP, thus increasing the effective lifetime. Therefore, the samples were dipped into grounded IPA to remove this residual surface charge. The effective lifetimes, with no residual surface corona charge, along with the interface charge after field-assisted ionic migration at each temperature for the anneal times are shown in Figure 47. Error bars represent three standard deviations of the interface charge uniformity data taken from Figure 44.

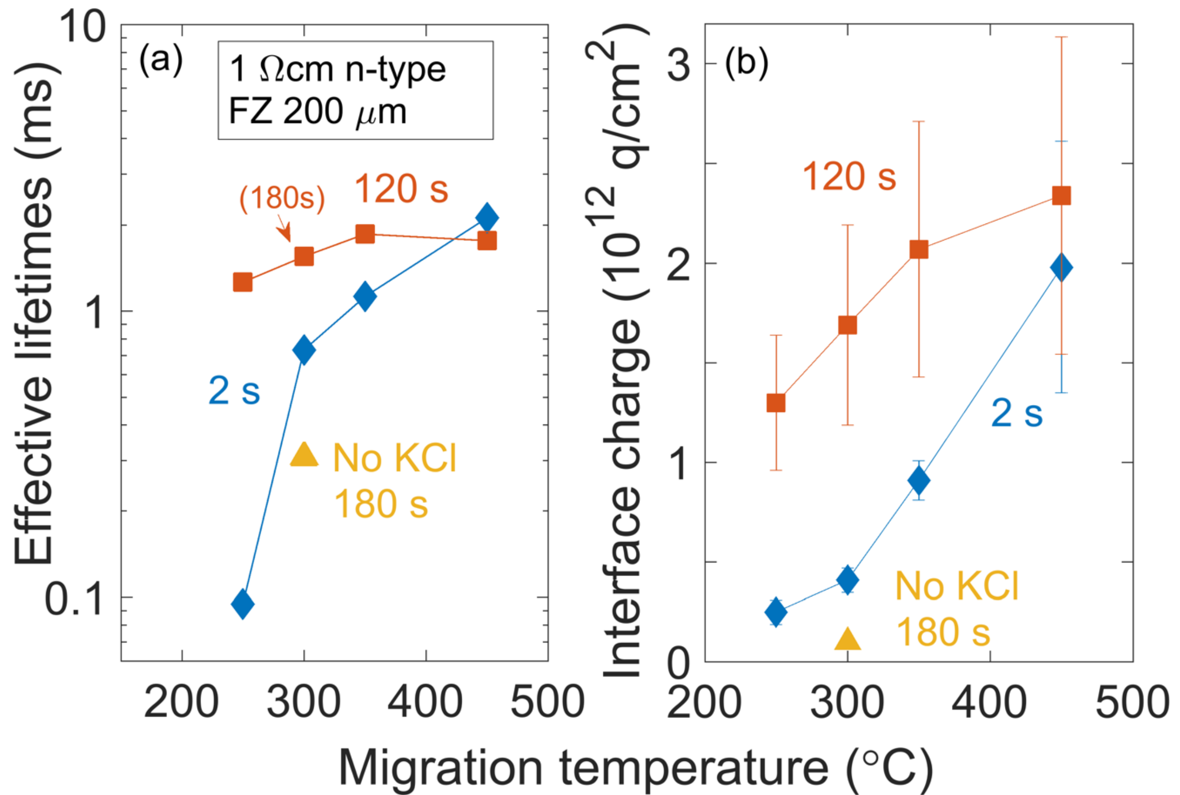

Figure 47. (a) Effective lifetimes and (b) interface charge after corona-induced field-assisted ionic migration of thermally evaporated potassium precursor using a surface charge of 1.9 x 10^{12} q/cm^2 with varying anneal temperature for various anneal times. Effective lifetimes shown are with no residual surface corona charge. Error bars show ±3σ of interface charge uniformity, taken from results shown in Figure 44.

Figure 47 reveals that the control, with no KCl but the same corona-induced electric field and migration anneal at 300 °C, shows an increase in effective lifetime compared to the initial lifetime of 75 μs, but an almost negligible interface charge. It is possible that the sample, as-received, had higher chemical passivation than the other samples shown in Figure 47 as they came from different wafers. Alternatively, it is possible that a 3 minute anneal at 300 °C, could be improving the chemical passivation at the SiO_2-Si interface by facilitating bond re-formation.

6.3.2.1 DISCUSSION

From Figure 47 (b) it is clear, especially for the two-second anneals, that at higher migration anneal temperatures it is possible to achieve higher concentrations of interface charge. This is because at higher temperatures, in the time allowed, a greater proportion of K^+ ions are able to overcome the barrier to enter the SiO_2. This is particularly evident during the short anneal time, when the system is far from reaching equilibrium. Despite the transposed error bars for interface charge (from Figure 44) being relatively large after an anneal length of 120 seconds, there is a clear relationship between temperature and interface charge for the two-second anneals.

The effective lifetimes of the samples, shown in Figure 47 (a), increase with anneal temperature, indicating that the surface passivation is increasing in this range of interface charge concentration. The temperatures investigated here are all appropriate for oxidised silicon processing under typical laboratory conditions and do not require special cleanroom conditions.

Figure 47 (b) shows that ions are introduced in under two seconds on the hotplate. At 450 ˚C, a migration anneal of two-seconds is seen to be sufficient to introduce an interface charge concentration comparable to a migration anneal of 120 seconds. This two-second anneal at 450 ˚C provides the highest effective lifetime in Figure 47 (a), indicating that it provides the best quality surface passivation. Although this effective lifetime is only marginally superior to those achieved after a 120 second anneal at 350 °C and 450 °C, as under these three conditions a similar concentration of interface charge was achieved.

A two-second anneal is extremely quick, and very promising in developing a rapid process for industrially introducing ionic FEP. It is possible that the ionic introduction occurred in an even shorter anneal time than two seconds as lower anneal times were not investigated.

6.4 SIMS Evidence for Potassium Introduction

In order to verify the presence of potassium at the SiO_2-Si interface, samples were processed and sent to Aystorm Scientific for SIMS analysis. The specimens were spin coated with KCl precursor, cleaved into 1 cm x 1 cm squares, deposited with corona charge to give a surface charge concentration of 1.8×10^{12} q/cm^2 and annealed at 450 °C for 2 seconds or 60 seconds. The SIMS profiles for K and Na are shown in Figure 48 with respect to depth from the oxide surface.

The concentration profile can be integrated using the trapezoidal numerical method with respect to depth across the interface to give the interfacial concentration of the atomic species. The calculated concentrations are shown in Table VII along with the interfacial change concentration from CV. Again, the depth resolution of the SIMS results is relatively large with respect to the depth of interest; there are few measurements taken around the peak in the species of interest. Therefore, the trapezoidal integral to calculate concentration is likely to be an overestimate.

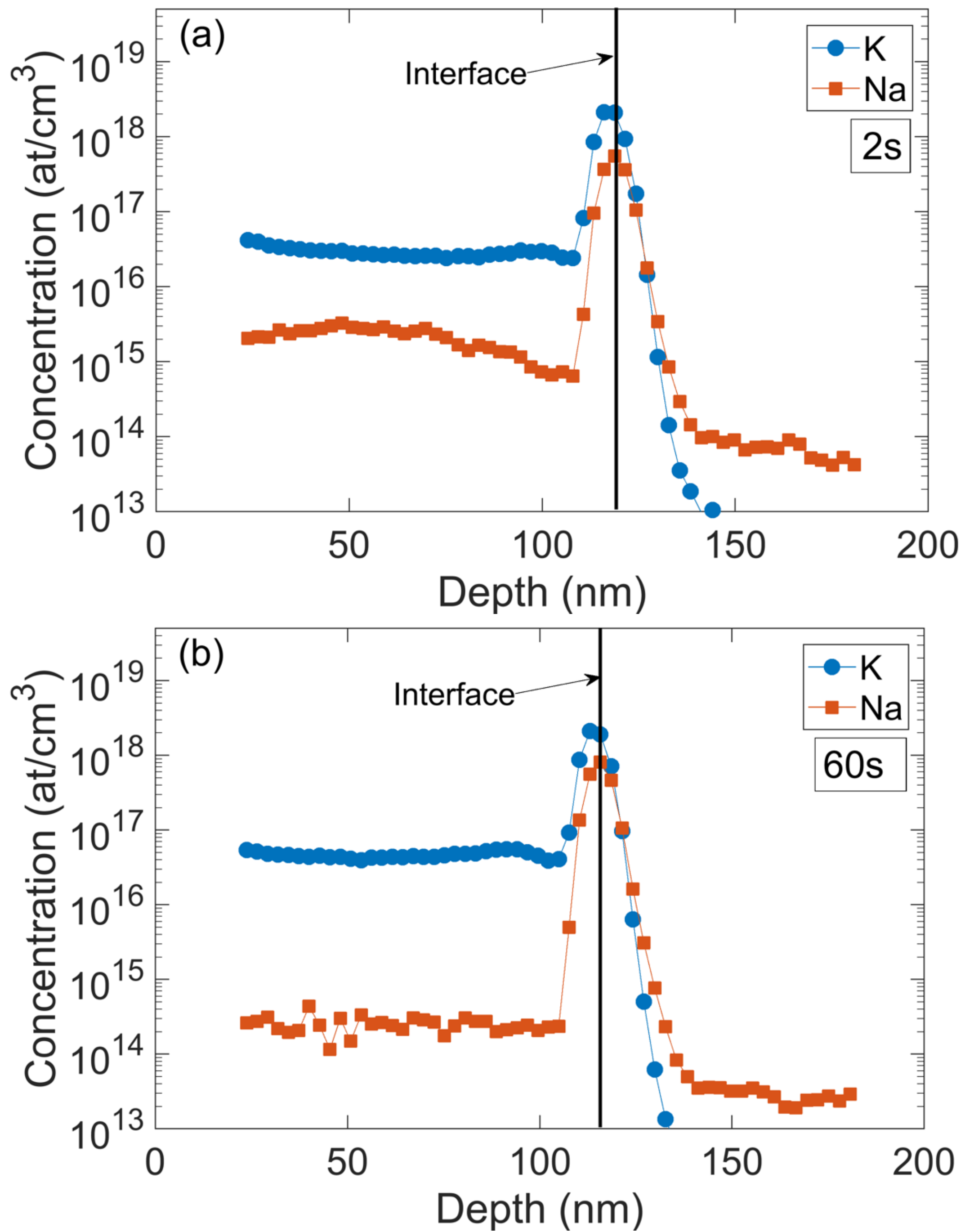

Figure 48. SIMS results showing concentration of potassium and sodium against distance into SiO_2 dielectric after field assisted ionic migration using a surface corona charge concentration of 1.8 x 10^{12} q/cm^2 at 450 °C for anneal lengths of (a) 2 seconds and (b) 60 seconds.

Table VII Interface charge from CV and K and Na concentrations from SIMS for samples spin coated with K followed by field-assisted ionic migration for different anneal times

Anneal time (s)	Interface charge from CV (10^{12} q/cm^2)	Interface K concentration from SIMS (10^{12} at/cm^2)	Interface Na concentration from SIMS (10^{12} at/cm^2)	Depth limits for SIMS integration (nm)
2	1.8	1.7	0.4	105 to 144
60	1.7	1.6	0.6	102 to 141

The correlation between interface charge concentrations from CV and the atomic concentration of K at the interface, as calculated from SIMS, strongly support that the interfacial charge is predominantly caused by the purposefully deposited ionic precursor. The concentration of Na at the interface is low, which shows that there is limited contamination caused by spin coating.

6.5 CONCLUSIONS

This chapter presents results using fast, scalable and effective methods to improve the field effect passivation of a SiO_2-Si interface by the introduction of ions to the dielectric. Ions are deposited by spin or spray coating and transported in seconds using field-assisted ionic migration. The results show that both spin and spray coating allow the precursor to be deposited on the oxide in a suitable manner, such that ions can be introduced into the dielectric. This process has been seen to reduce the SRV of 1 Ωcm Si, from 100 cm/s to 3.3 cm/s, equivalent to a J_{0s} of 8.4 fA/cm^2, using scalable, industrially appropriate techniques. It is clear that field-assisted ionic migration using corona discharge is a rapid, effective technique to enhance FEP, requiring a migration anneal of under 2 seconds at 450 °C. If exploited, this technique has the potential to improve current methods of surface passivation of silicon, allowing tailored, extrinsic field effect passivation to be applied in a matter of seconds, and at a very low cost. In comparison, and on the same material, the

enhanced alneal was able to achieve a minimum SRV of 0.15 cm/s at an interface charge concentration of 1.3 – 1.8 x 10^{12} q/cm^2. This charge concentration is the same as the charge concentrations investigated in this chapter, which indicates there is still room for improvement for the field-assisted ionic migration process as the SRV is not as low as it was for the enhanced alneal. This is considered in the next chapter.

CHAPTER 7
OPTIMISING ION-INDUCED FEP

In the previous chapter, a promising commercial technique for introducing ionic species for field effect surface passivation was presented. In this chapter, in an attempt to match the surface passivation achieved by the enhanced alneal, shielded hydrogen passivation was employed along with ionic FEP through field-assisted ionic migration. Up until this point, only one ionic species has been intentionally used - potassium. Although potassium is a promising element for ionic FEP, it is possible that the stability of the surface passivation could be improved by the use of alternative ionic species. Several alternative ions were trialled; these were rubidium, magnesium, calcium, and strontium. The ion precursors were deposited using spin coating, and injection was by field-assisted ionic migration. This chapter aims to identify ionic species and investigate hydrogenation processing which could improve industrially achievable surface passivation further.

7.1 SUPPLEMENTING IONIC FEP WITH HYDROGEN

It is well known that hydrogenation increases the chemical passivation of the SiO_2-Si interface [17]. The reason why the alneal is so effective is thought to be due to the presence of hydrogen released during processing. The enhanced alneal was found, in Chapter 4, to be significantly more effective than the standard alneal, due to the presence of Na and K ionic

species that provide FEP. However, the alneal is not industrially compatible. Chapter 6 lays out a scalable technique for ion introduction and presents data using K as the ionic species of interest. However, the effective lifetimes achieved by K ionic FEP are not comparable to that of the enhanced alneal, despite the ionic species being the same, and of a similar concentration. For this reason, it is assumed that the superior surface passivation of the enhanced alneal is due to the hydrogen released during the alneal process, as discussed in Chapter 4. In an attempt to increase the surface passivation of the industrial ionic introduction process of Chapter 6, these samples underwent Shielded Hydrogen Passivation (SHP) [39, 40]. SHP, at present, is conducted in a PECVD under a vacuum and takes a substantial length of time. However, the process has the potential to be industrially compatible by reducing the vacuum and time necessary and converting the process to be an in-line process. For the purpose of this work, SHP was used as it is the most affective hydrogenation process available in the laboratory.

It is possible to introduce the hydrogen by SHP, either before or after ion introduction. However, it was unclear, if the hydrogenation process was first, whether the hydrogen would diffuse away from the sites it was passivating during the anneal for field-assisted ionic migration. To test this, SHP was tested both before and after ionic migration. Oxidised 1 Ωcm n-type Si, cleaved into quarters of a 4” wafer was used for these experiments to reduce edge-effect limitations [148]. Ionic FEP was introduced using spin coating as the ionic precursor deposition technique followed by deposition of a surface corona charge concentration of 1.9×10^{12} q/cm^2. The specimens were then annealed at 450 °C for 5 seconds. This anneal length was used because, from Chapter 5, it was known that at this temperature the length of anneal, above two-seconds, seemed to have little effect on the interface charge. The SHP was conducted at 350 °C for 40 minutes on each side using a pre-treated palladium foil. Details can be found in references [39, 40]. The effective lifetimes of

the samples were recorded after each processing step, and the interface charge measurement was made at the end of the processing sequence using the Hg-CV probe.

In the first case, the hydrogen was introduced prior to the ionic species for FEP. Figure 49 (a) shows the effective lifetime at the standard injection level of 10^{15} cm^{-3} for different processing stages and the interface charge concentration after the processing was complete. The injection level dependent lifetime curves are shown in Figure 49 (b).

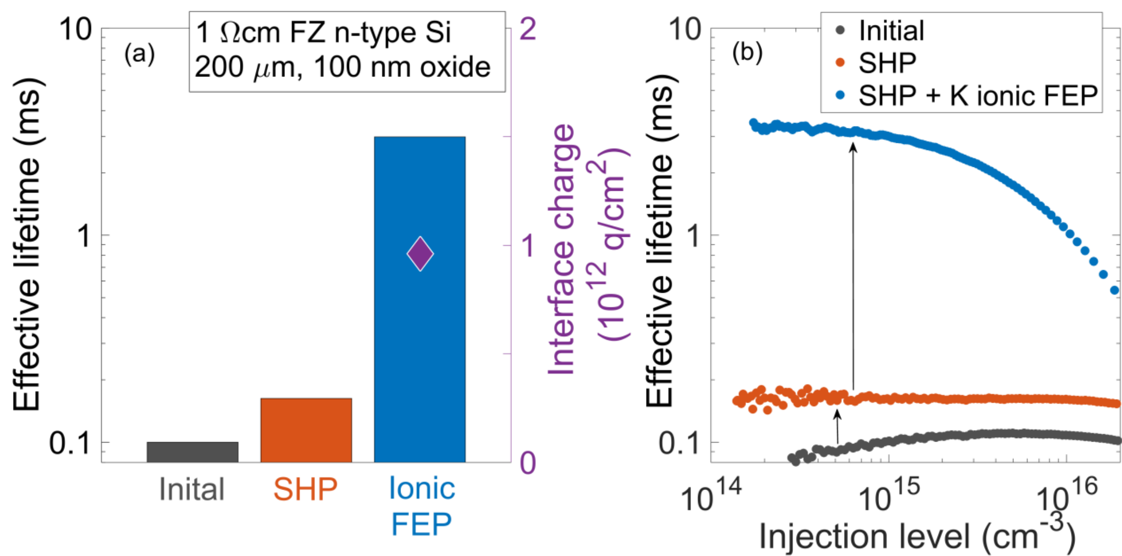

Figure 49. Shielded hydrogen passivation followed by ionic FEP showing (a) the effective lifetimes at an injection level of 10^{15} cm^{-3} after each processing step along with the final interface charge concentration and (b) the injection dependent effective lifetime curves after each step.

In Chapter 6, K ions were introduced to samples that had not undergone SHP, using the same technique as shown here. The effective lifetime of a sample with a comparable interface charge concentration can be found Figure 42 of Chapter 6. The effective lifetime was ~ 1800 µs for an interface charge concentration of 0.8 x 10^{12} q/cm^2. In Figure 49, the effective lifetime of the hydrogenated sample with the addition of ionic FEP at a concentration of 0.9 x 10^{12} q/cm^2 is almost 3000 µs, a significant improvement. This indicates that some hydrogen passivation of the interface states remains despite the subsequent anneal used to introduce FEP. The effective lifetime is not as high as that of the

enhanced alneal, where it was seen to be more than double this at 6750 μs in the best instance. However, the enhanced alneal samples contain a greater concentration of interface charge ($1.3 – 2 \times 10^{12}$ q/cm^2), which could partly account for this increased effective lifetime.

For the sample shown in Figure 49 of this chapter, the deposition parameters were selected using Figure 46 in Chapter 6 to provide an interface charge concentration of 1.7×10^{12} q/cm^2, comparable to that of the enhanced alneal. Despite this, the interface charge measured after hydrogenation and ion introduction is significantly lower than this at 0.9×10^{12} q/cm^2.

Although the sequence of SHP followed by ionic FEP was successful at increasing the chemical passivation of the sample, introducing the hydrogen after the ionic species may have a twofold benefit. Firstly, it may prevent the opportunity for the movement of hydrogen by introducing the hydrogen after the anneal needed for ionic migration. This may allow the chemical passivation to improve even further. Secondly, the desired concentration of interface charge may be introduced without the complexity of hydrogen present at the interface during migration. With this in mind, the introduction of ions before SHP was tested. The effective lifetimes of the samples were recorded after each processing step, and the interface charge measurement was calculated at the end of the processing sequence using the Hg-CV probe. As before, Figure 50 (a) shows the effective lifetime at the standard injection level of 10^{15} cm^{-3} for different processing stages and the interface charge concentration. The injection dependent lifetime curves are shown in Figure 50 (b).

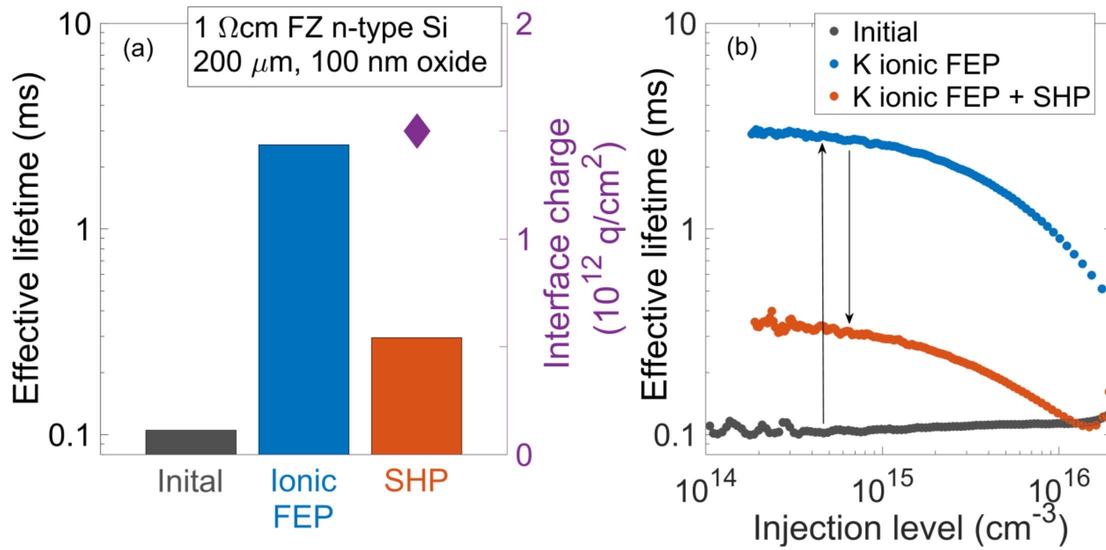

Figure 50. Ionic FEP introduction followed by shielded hydrogen passivation showing (a) the effective lifetimes at an injection level of 10^{15} cm^{-3} after each processing step along with the final interface charge concentration and (b) the injection dependent effective lifetime curves after each step.

In contrast to the success of SHP followed by introduction of ionic FEP, the reverse order of processing reduces the effective lifetime of the specimen. Initially, the effective lifetime is significantly improved by the presence of ionic FEP, and a charge concentration closer to that expected is introduced by the field-assisted ionic migration, as shown in Figure 50 (a). However, when SHP is conducted, the effective lifetime drops by an order of magnitude. This result was unexpected but has led to a better understanding of the mechanisms of hydrogen introduction and will be further investigated by Gabrielle Bourret-Sicotte in her doctoral research. At present, it is postulated that the presence of the K ions at the SiO_2-Si creates a dipole at the interface that encourages the introduction of the charged hydrogen to the silicon bulk. High concentrations of hydrogen in the silicon bulk have been shown to cause damage [165–167], resulting in a reduction in effective lifetime. Such high quantities of hydrogen may be prevented from entering the silicon of as-received oxidised samples due to the lack of the ion-induced dipole, which may present a larger barrier to hydrogen migration across the SiO_2-Si interface.

From this, it can be concluded that hydrogenation is successful at improving the effective lifetime of an ionic field-effect passivated sample by increasing the chemical passivation. If hydrogen is to be used in conjunction with ionic FEP, the hydrogen passivation should occur first. The rest of this chapter studies the introduction of alternative passivating ions with the view to improving the stability of the ionic FEP.

7.2 Preliminary Investigation of Different Ionic Species

From the research presented in this thesis and throughout the literature, it is evident that potassium and sodium are both able to migrate through an SiO_2 layer and reside at the SiO_2-Si interface as a charged species. It is paramount that, once the ions are situated at the interface, they are stable for over 30 years, which is the expected use life of a commercial solar cell. Potassium has been shown to exhibit good stability under room temperature conditions, with a decay time constant of over 40 years [62]. However, in use, solar panels do not operate under dry, room temperature conditions.

To test the stability of Na and K under more extreme conditions, samples were thermally evaporated with the respective ionic precursor and fabricated into MOS structures using evaporated aluminium as the front and back contact. This was done in the contaminated thermal evaporator. The samples were then processed using TSIC (thermally stimulated ionic conduction) to introduce the ions to the SiO_2-Si interface. Once the ions were present, the specimens were then exposed to a reverse bias of – 10 V at an elevated temperature of 100 °C and measurements of the interface charge concentration were taken after varying lengths of time. These are shown for Na in Figure 51 (a) and for K in Figure 51 (b).

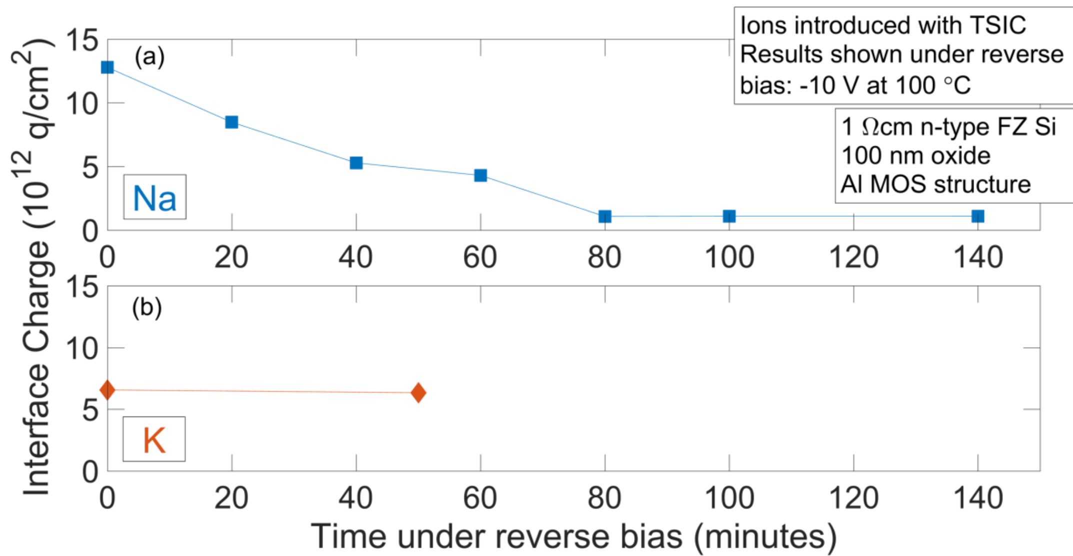

Figure 51. Interface charge concentration of (a) Na and (b) K introduced by TSIC followed by exposure to a reverse bias of -10 V at a temperature of 100 °C for various lengths of time.

It is clear from Figure 51 (a) that Na is not stable under these conditions and will readily migrate away from the SiO_2-Si interface. Whereas, K ions are shown in Figure 51 (b) to be relatively stable under these reverse bias conditions, indicating that this ionic species is far more suitable for surface passivation of solar cells. The length of anneal for the K is shorter, at 50 minutes, because after this time period no difference in interface charge was recorded. Whereas, for the Na sample, once a reduction in interface charge was measured, the experiments were continued until there was no further reduction in interface charge. These measurements were simply indicative. Further studies on K stability were published by Bonilla in reference [62].

Although K is a promising ionic species for solar cell FEP, which is why it has been the focus of the experimental results shown so far, there may exist ionic species that would exhibit even greater stability at the SiO_2-Si interface. The challenge is that the species must be able to be injected into, and migrate through, the SiO_2 layer under suitable processing conditions and then reside at the SiO_2-Si interface as a charged species. Because potassium

is more stable than sodium, as shown in Figure 51, rubidium (Rb), the next largest group 1 element, was tested. This was accompanied by several group 2 elements: magnesium (Mg), calcium (Ca), and strontium (Sr). Results using caesium (Cs) are not included here because the experiments were conducted by another member of the group.

Ionisation energy decreases with increasing period, and therefore is larger for Na than for K or Rb. Ionisation energy also increases with group number and the second ionisation energy is always greater than the first. For this reason, it is unclear if Mg, Ca or Sr would be fully ionised to 2+, or partially ionised to 1+, or ionised at all. If fully ionised, the ionic radius for elements increases with increasing period and decreases with increasing element group. When fully ionised, ionic radii of Mg2+ < Ca2+ < Sr2+ < Na+ < K+ < Rb+. However, if Mg, Ca and Sr are atoms, Mg < K+, but Ca and Sr are larger than all of the group 1 ions. These patterns may offer an explanation to why some ions successfully reach the Si-SiO_2 interface as charged ions and some do not.

It is expected that ions with a lower rate of injection will be more stable at the SiO_2-Si interface. This is because a lower rate of injection implies a larger energy barrier and from the work by Nauta and Hillen [151], there appears to be a correlation between energy for injection from the Al-SiO_2 interface and trap energy level at the SiO_2-Si interface for Na and K.

The chloride salt of the species was dissolved in an 25 % H_2O, 75% IPA solvent and spin coated on to the oxide surface of a 3 x 3 cm^2 sample. The solubility of each salt is important in determining whether the solvent water:IPA ratio needs to be adapted, and also in recognising if salt crystals are more likely to form on the sample surface. If a salt has a particularly low solubility, it is possible that crystals will precipitate on the oxide surface

while the solvent is evaporating during the spinning process. The solubility of each salt is given in Table VIII.

Table VIII Solubility of various salts in water at 20 °C and 1 atmosphere pressure [168]

Salt	KCl	RbCl	$CaCl_2$	$MgCl_2$	$SrCl_2$
Solubility (g/100 mL)	34.2	91	52.9	54.6	74.5

It is clear that for all of the salts used, they are all more soluble in water than KCl. As KCl is known not to precipitate and form salt crystals at these concentrations, the same is assumed to be the case for these salts.

The purity of the salt is also important in ensuring that any interface charge measured is not from Na and K contamination of the salt itself. The purity of the salts is summarised in Table IX.

Table IX Salt supplier and chemical specification, for details on contamination

<table>
<tr><td>Salt</td><td>RbCl (99.8% purity)</td><td>$CaCl_2$</td><td>$MgCl_2$</td><td>$SrCl_2$</td></tr>
<tr><td>Supplier and
Product No.</td><td>Sigma Aldrich
215260</td><td>Fisher Scientific
C/1500/53</td><td>Fisher Scientific
M/0600/53</td><td>Fisher Scientific
S/8280/50</td></tr>
<tr><td>Na (ppm)</td><td rowspan="2">Total trace metal content < 2500 ppm</td><td>100</td><td>10</td><td>500</td></tr>
<tr><td>K (ppm)</td><td>50</td><td>10</td><td>200</td></tr>
</table>

The trace concentration of Na and K in all of the salts make it highly unlikely that contamination from the salt itself would be responsible for any measured charge concentrations. In the worst instance, if a concentration of 10^{14} ions/cm^2 was deposited of Rb, only 10^{11} q/cm^2 could possibly exist from Na and K contamination. This calculation assumes both an over-deposition of the Rb salt and that all of the metal trace contamination is Na and K, which is highly unlikely. Therefore, trace metals are disregarded.

To investigate whether it was possible to introduce each ionic species, samples were cleaved into < 1 x 1 cm^2 samples and field-assisted ionic migration using various concentrations of surface corona charge were tested. Anneal temperatures were between 450 – 500 °C, and the anneal time was adapted for each species to allow the corona-induced electric field to reduce significantly, which was found to take a different length of time for each species.

7.2.1 RUBIDIUM

Spin coating was carried out using a concentration of 9 x 10^{-5} mol/L of RbCl in a solvent of 25% H_2O, 75% IPA. The initial surface species concentration was calculated to be 2.4 x 10^{13} ions/cm^2, based on work by Du [107]. Field-assisted ionic migration was conducted using an anneal temperature of 450 °C and a time of 4 minutes. Anneals of 1, 2 and 3 minutes were deemed too short to reduce the surface charge significantly; however, four minutes was sufficient to allow surface corona charge to reduce to less than 1.3 x 10^{11} q/cm^2. The interface charge concentrations against initial surface corona charge are shown in Figure 52.

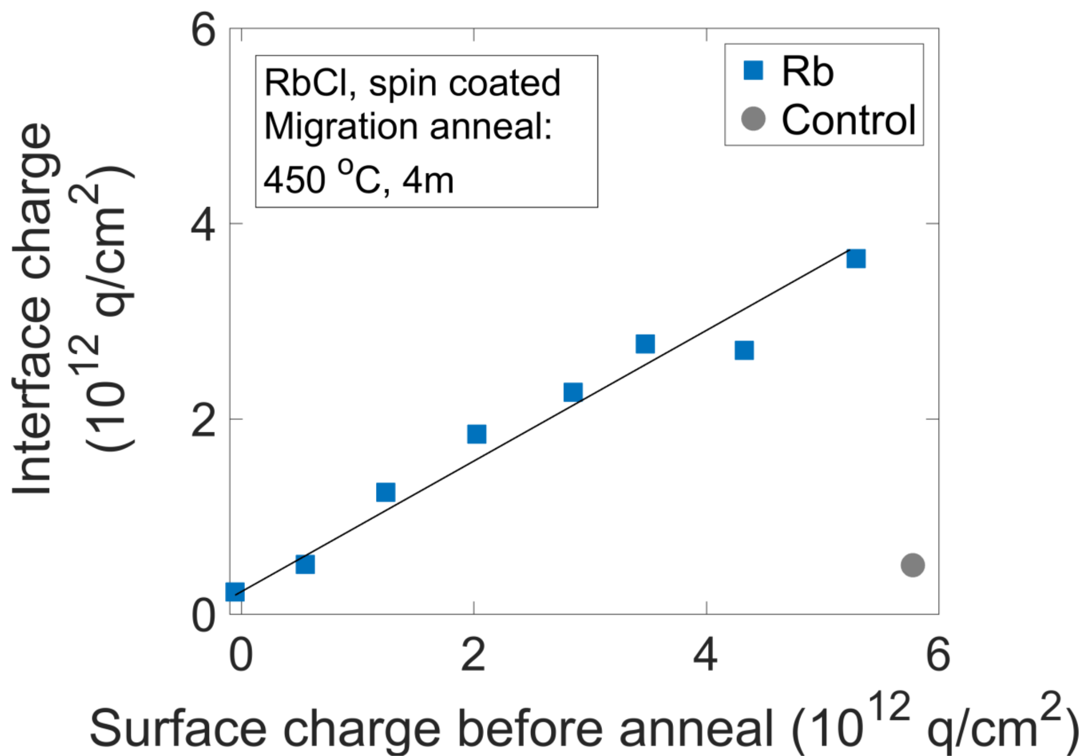

Figure 52. Interface charge concnetration after spin coating with RbCl and field-assisted migartion at 450 °C for 4 minutes, using different concnetrations of surface corona charge before migration anneal.

Figure 52 shows that it is possible to introduce Rb to the SiO_2-Si interface, where it resides as a charged ion. However, the time necessary for migration of Rb at 450 °C is at least two orders of magnitude larger than for K. Interestingly, the relationship between interface charge concentration and surface corona charge concentration is different to that for K, shown in Figure 46 of Chapter 6. In the case of Rb, for every three surface corona charges deposited, two interface charges are measured after field assisted ionic migration, whereas for K this relationship is very close to one-to-one. This is believed to be because of the length of the anneal required for the Rb to be injected into and migrate across the oxide layer. The length of anneal may allow for the surface corona charge to decay by other mechanisms. The apparently lower rate of injection is a promising indication that the ion may be more stable at the SiO_2-Si interface.

Due to the encouraging results for Rb, shown in Figure 52, a 3 x 3 cm^2 specimen was produced for effective lifetime measurements, to determine the quality of the overall surface passivation achieved by the presence of the Rb ions. The injection dependent effective lifetime curve, for a specimen with an interface charge of 1.5 x 10^{12} q/cm^2, is shown in Figure 53 (a). As a comparison, Figure 53 (b) shows the effective lifetime curve of a sample with ionic FEP caused by potassium at a concentration of 1.5 x 10^{12} q/cm^2.

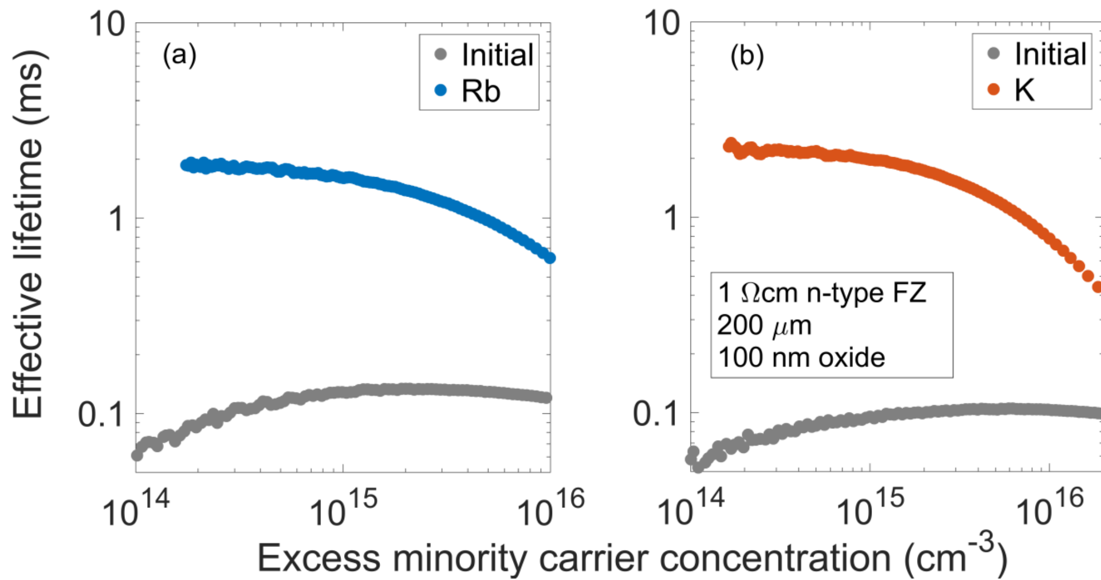

Figure 53. Injection dependent effective lifetime curves for samples deposited with (a) Rb and (b) K precursor and treated with field-assisted ionic migration to result in an interface charge concentration of 1.5 x 10^{12} q/cm^2.

It is clear from the increase in effective lifetime shown in Figure 53 (a) that Rb at the SiO_2-Si interface is providing FEP and not introducing significant interface trap levels. The effective lifetime achieved by Rb is similar to that of a sample passivated with K at the same interface charge concentration, as shown in Figure 53 (b). At the standard injection concentration of 10^{15} cm^{-3}, the effective lifetime of the Rb sample is 1600 μs and the K sample is 1970 μs. This is promising as Rb is expected to be more stable at the SiO_2-Si interface than K. However, an industrial challenge at present is the time necessary for field-assisted ionic migration of Rb at 450 °C, which is longer than is preferable. At higher

temperatures, it is likely that the time needed would reduce. To test this, samples spin coated with RbCl solution were annealed at 500 °C using a surface corona charge concentration of 2.0 x 10^{12} q/cm^2, for various lengths of time. The residual surface corona charge after the migration anneal and the interface charge concentrations are shown in Figure 54 against anneal time.

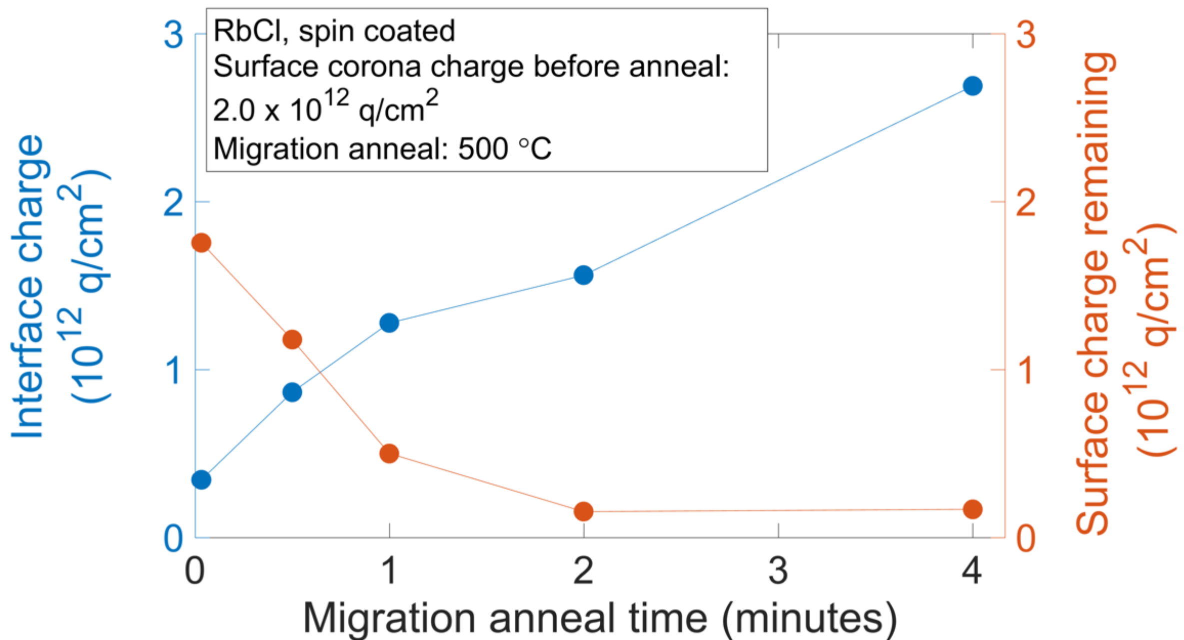

Figure 54. Resulting interface charge concnetration (left) and remaining surface charge concentration (right) for samples spin coated with RbCl and treated with field-assisted ionic migration at 500 °C, for different lengths of time, using an initial surface charge of 2 x 10^{12} q/cm^2.

It is clear from Figure 54 that even at a temperature of 500 °C, an anneal time of several minutes is necessary to introduce the required concentration of Rb. This is not ideal for industrial processing, but it is probably not prohibitive. Furthermore, the process is believed to slow as the concentration of corona charge on the oxide surface reduces. In order to avoid this, it may be possible to supplement the corona charge as the sample is annealed, making the process more likely to be able to meet the 1 wafer/second throughput target.

7.2.2 MAGNESIUM

The remaining ionic species tested are group 2 elements, meaning that it is possible that they may reside at the SiO_2-Si interface with a charge of 2+. This could offer a potential advantage because only half the quantity of ions would be needed to provide the same quantity of FEP. Therefore, if it is concluded that the presence of ions at the SiO_2-Si interface is damaging the chemical passivation, fewer ions may result in less damage. However, this would depend on the properties of the interface trap levels that are introduced, and would need to be investigated for each ionic species.

7.2.2.1 MAGNESIUM-ALUMINIUM ALLOY

Initially, an enhanced alneal using magnesium-aluminium alloy was tested. This was not done with industrial application in mind, but instead it was considered as a laboratory scale technique. If the use of this alloy was successful in providing carrier lifetimes similar to that of the enhanced alneal, then researchers could easily achieve record breaking surface passivation, simply by changing the evaporation source. Due to the contamination of the thermal evaporator in the Oxford cleanroom at Begbroke, the samples were prepared using the e-beam evaporator at Southampton University. In order to confirm the cleanliness of this evaporator an alneal with pure aluminium was also conducted. 3 x 3 cm^2 samples were evaporated with 100 nm of either Al or AlMg. The AlMg alloy was 5% Mg; therefore, in a 100 nm layer, the concentration of Mg was 3 x 10^{16} atoms/cm^2. The samples were then annealed under standard laboratory conditions at 400 ˚C for 30 minutes in the large tube furnace. After this, the metals were etched using commercial aluminium etchant, the effective lifetimes were measured, and the samples were then incrementally corona charged to maximise the FEP. Sections of the samples were cleaved off and fabricated into structures suitable for CV measurements. This was achieved by removing the back oxide with HF and

using InGa and silver dag to contact the samples, which were then measured in the Hg-CV probe. The injection dependent lifetime curves for a corona charged control, an Al alnealed sample and an AlMg alnealed sample are shown in Figure 55. The interface charge concentration is shown in an inset and the surface charge concentration is also given.

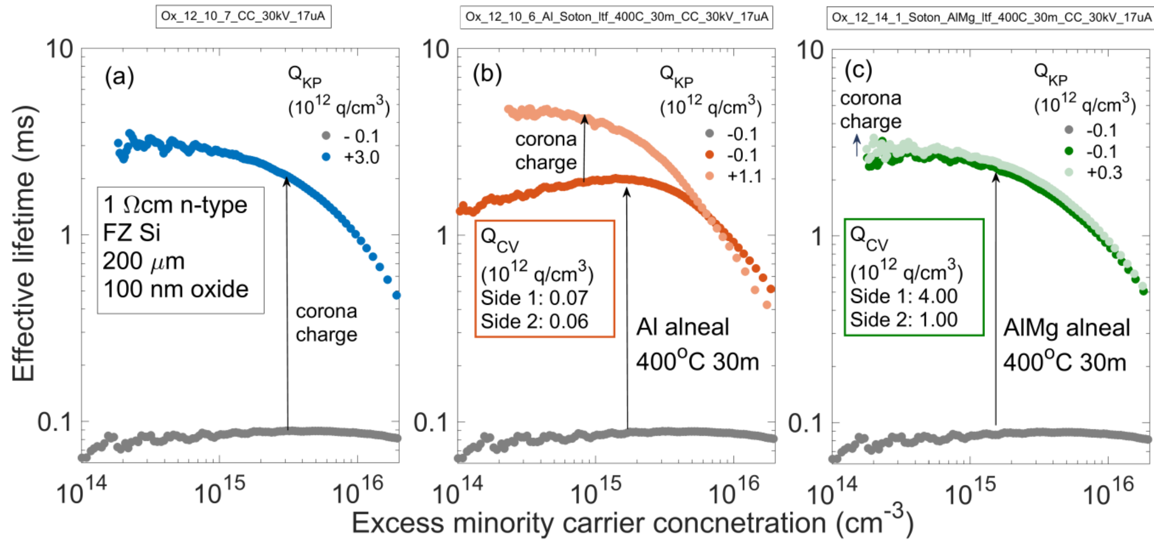

Figure 55. Injection dependent effective lifetime curves for (a) an as-received sample and with the addition of corona charge, (b) an Al alneal sample before and after processing and with the addition of corona charge for maximum FEP and (c) an AlMg alneal sample before and after processing and with the addition of corona charge for maximum FEP. Surface charge concentrations Q_{KP} and interface charge concentrations Q_{CV} given. Sample size: 3 x 3 cm^2.

It is clear from Figure 55 (b) that the effective lifetime was improved by the Al alneal sample to a value expected of a standard alneal (1970 μs). As an e-beam evaporator was used, it was possible that there may have been some damage to the SiO_2-Si interface. However, this damage is known to be improved by an anneal at 260 °C for 17 minutes [37], which reduces the D_{it} by an order of magnitude. Therefore, it is likely that after 30 minutes at 400 ˚C the majority of introduced damage would have annealed out, which appears to be the case from the high effective lifetime shown in Figure 55 (b). In this figure, after corona charging, the effective lifetime reaches a much greater value (3980 μs) than that of the corona charged control (2770 μs), shown in Figure 55 (a). This confirms that there has been an improvement to the chemical passivation. The interface charge concentration is measured as negligible,

showing that the e-beam evaporator at Southampton University is uncontaminated and that any interface charge found after the AlMg experiment will not be due to contamination of the evaporator.

The effective lifetime of the AlMg alnealed sample (2490 μs), shown in Figure 55 (c), is higher than that of the Al alneal sample. The CV measurements of interface charge concentration indicate that some charge is introduced during this process, which was not the case for the Al alnealed sample. Therefore, this charge concentration is likely to be due to the presence of Mg. When corona charge is added to the sample, in order to increase the FEP, the effective lifetime of the sample improves only slightly (2630 μs) and does not reach that of the corona charged Al alnealed sample. It is possible that this is due to the ionic species responsible for the measured interface charge reducing the chemical passivation. An alternative is that, due to the size of these samples (3 x 3 cm^2), the effective lifetimes could have been limited by edge recombination. Although the samples were approximately the same size, there is the possibility of a small variation in size which could have led to this <10% difference in effective lifetime.

To ascertain whether the interface charge was due to Mg at the SiO_2-Si interface, a second sample was prepared for SIMS analysis. The SIMS analysis showed that at the SiO_2-Si interface, negligible Mg was present. However, concentrations of K and Na were recorded. When the Na and K concentrations of the SIMS profile were integrated over the interface, the concentrations were calculated to be 1.4 x 10^{12} q/cm^2 and 0.5 x 10^{12} q/cm^2 respectively, giving a total charge due to K and Na of 1.9 x 10^{12} q/cm^2. As the interface charge of the sample, as measured by CV, was 2.3 x 10^{12} q/cm^2, it appears that the majority of the charge is due to the contamination of K and Na. As no interface charge was measured by CV for the Al alneal sample, which had been evaporated in the same evaporator, it is likely that

either the K and/or Na is contamination from trace metals in the AlMg alloy or the annealing process, as the sample prepared for SIMS was annealed using a borosilicate glass petri dish on a hot plate instead of the tube furnace.

7.2.2.2 MGCL SPIN COATING

Spin coating was carried out using a concentration of 9 x 10^{-5} mol/L of $MgCl_2$ in a solvent of 25% H_2O, 75% IPA. The initial surface species concentration was calculated to be 2.4 x 10^{13} ions/cm^2, based on work by Du [107]. Field-assisted ionic migration was tested under varying surface corona charge concentrations at two different temperatures. The anneal times were selected according to how long it took for the maximum deposited surface corona charge to reduce to below 10^{11} q/cm^2. At 450 °C this was found to take only 1 minute. For the anneals at 500 °C, the anneal time was increased to 4 minutes, to investigate if the residual surface charge could decrease even further and to ensure the migration process had time for completion. Interface charge concentrations against initial surface charge concentrations are shown in Figure 56.

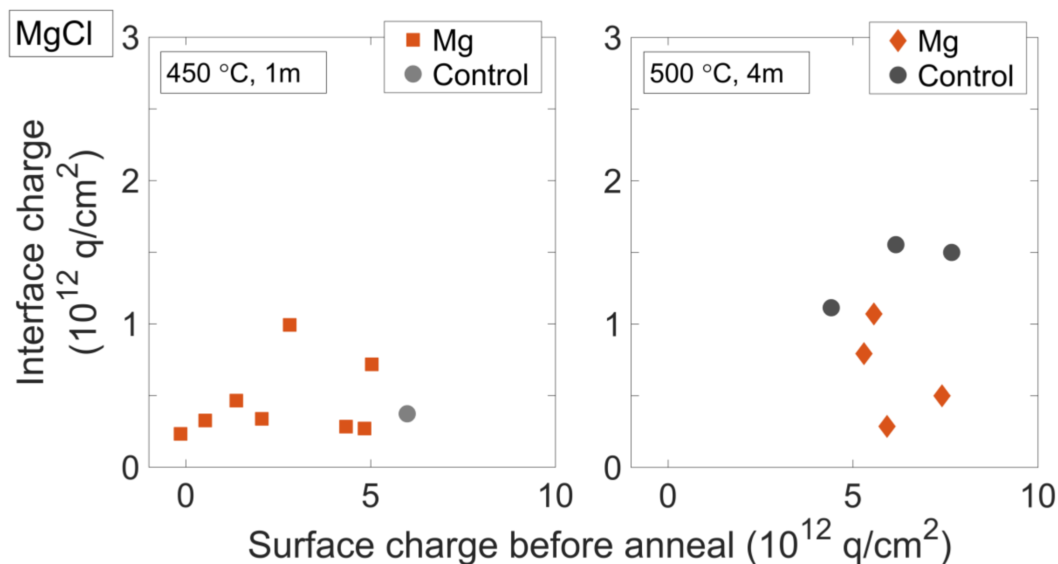

Figure 56. Interface charge concentrations for field-assisted ionic migration of MgCl spin coated samples deposited with varying concentrations of surface corona charge before annealing at a temperature of (a) 450 °C for 1 minute or (b) 500 °C for 4 minutes.

It appears that, if Mg does reach the SiO_2-Si interface, it does not reside there as a charged species. In Figure 56 (a) the majority of interface charge measurements are comparable to that of the control. One or two points show a greater interface charge concentration, but it is concluded that these apparent shifts in flatband voltage are due to the introduction of interface traps which are visible from the shape of the CV curves shown in Figure 57. The inset shows the surface corona charge before anneal and the time for which the sample was annealed.

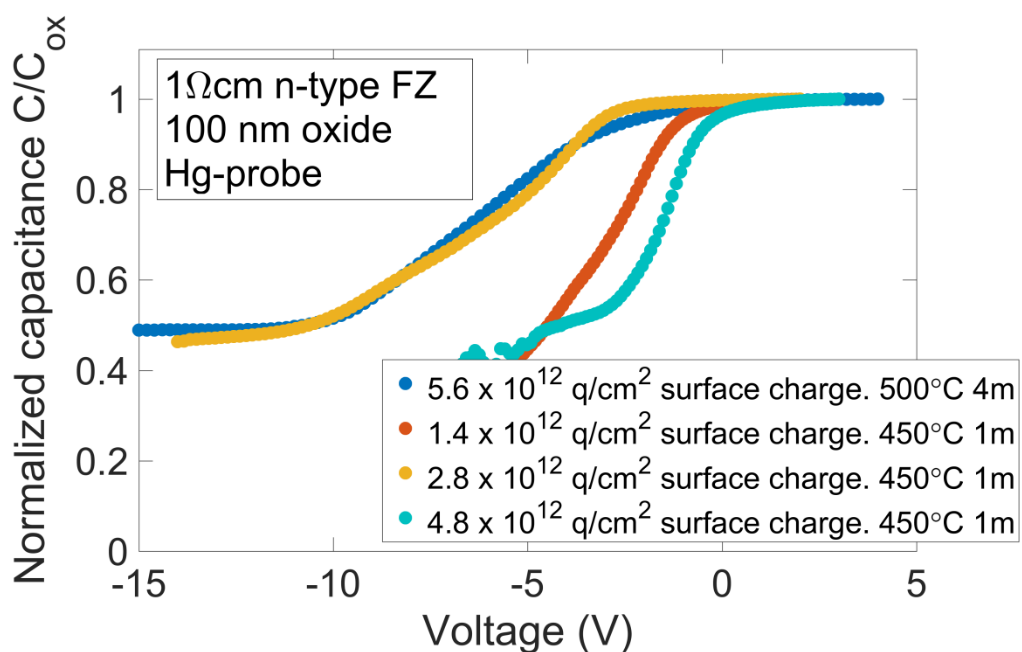

Figure 57. Capacitance-voltage curves for samples spin-coated with MgCl and treated with field-assisted ionic migration at 450 °C or 500 °C using several surface charge concentrations and an anneal of 1 or 4 minutes.

The horizontally-stretched nature of the blue and yellow CV curves shown in Figure 57 are characteristic of an interface with high trap density (see Chapter 3). The interface traps could indicate that on the occasions when Mg does migrate to the SiO_2-Si interface, it does not reside there as a charged species, instead it may be introducing interface traps.

Returning to Figure 56 (b), it is shown that when the anneal temperature is increased to 500 °C, the interface charge concentration exhibited by the control is increased. This implies that there may be a source of contamination at this temperature. As the anneals were not carried out in a cleanroom, but instead used the salt-specific (RCA 1 & 2 cleaned) borosilicate glass petri-dish on top of a hotplate, contamination is a possibility. Therefore, the results at 500 °C should only be considered to be caused by the intentionally deposited salts if the interface charge is consistently and significantly above that of the controls. The interface charge concentrations measured on the Mg spin coated samples are similar to that of the control and are therefore inconclusive.

7.2.3 CALCIUM

The sample was spin coated using a solution with a concentration of 9×10^{-5} mol/L of $CaCl_2$ in a solvent of 25% H_2O, 75% IPA. The initial surface species concentration was calculated to be 2.4×10^{13} ions/cm^2. Field-assisted ionic migration was conducted using an anneal temperature of either 450 °C or 500 °C, and a time of 6 minutes. This was found to reduce the surface charge concentration to under 3×10^{11} q/cm^2 for an anneal at 450 ˚C, and to below 2×10^{10} q/cm^2 at 500 ˚C. The interface charge concentrations after migration against surface corona charge before migration are shown in Figure 58.

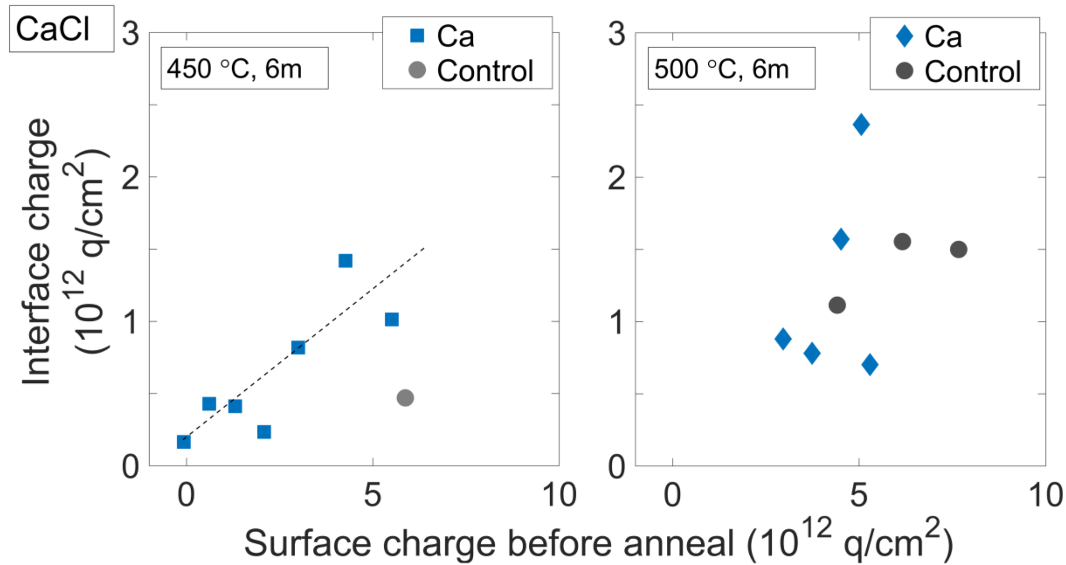

Figure 58. Interface charge concnetration for field-assisted ionic migration of CaCl spin coated samples deposited with varying concentrations of surface corona charge before annealing for 6 minutes at a temperature of (a) 450 °C or (b) 500 °C.

From Figure 58 (a), using an anneal of 450 °C, it appears that Ca may be injected and reach the SiO_2-Si interface as a charged species. However, less interface charge is introduced for a given surface corona charge compared to K or Rb. It could be that the rate of injection is significantly slower for Ca into SiO_2 than for these other species. From the KP measurements of surface charge after annealing, the residual surface charge concentrations were seen to be twice as large as that for Rb. This could indicate that the anneal length was not sufficient to allow the migration process to be completed. A longer anneal time may have been necessary to produce the linear relationship between interface and surface charge seen for K and Rb.

In an attempt to allow the migration process to reach completion, an anneal temperature of 500 °C was tested, and results presented in Figure 58 (b). The increase in the interface charge of the controls must be noted, as discussed previously. Therefore, only the limited number of results that exceed the controls should be considered. These indicate that the increase in anneal temperature results in an increase in interface charge. This is presumed to be due to

a larger injection rate, meaning that the same anneal time of 6 minutes allows the migration process to reach a stage nearer completion. This is supported by the residual surface charge reducing by an order of magnitude.

The relationship between interface charge concentration to surface corona charge before annealing, from the results at 450 °C, suggests that there is a larger energy barrier for injection for Ca than for either K or Rb. This may indicate that Ca would be even more stable at the SiO_2 interface than Rb.

7.2.4 STRONTIUM

A solution with a concentration of 9 x 10^{-5} mol/L of $SrCl_2$ in a solvent of 25% H_2O, 75% IPA was used to spin coat the samples. The initial surface species concentration was calculated to be 2.4 x 10^{13} ions/cm^2. Field-assisted ionic migration was conducted using anneal temperatures of either 450 °C or 500 °C, and a time of 7 minutes. At 450 °C, an anneal of this duration enabled the surface charge to reduce to less than 2 x 10^{11} q/cm^2, and at 500 °C, the surface charge was below 9 x 10^{10} q/cm^2. The interface charge concentrations against surface corona charge before migration are shown in Figure 59.

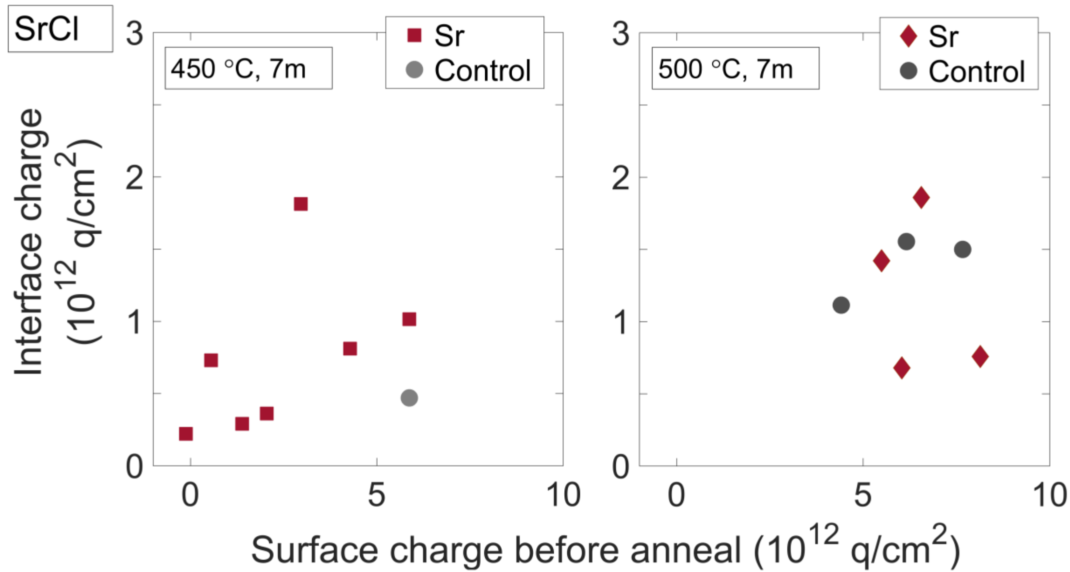

Figure 59. Interface charge concnetration after field-assisted ionic migration of SrCl spin coated samples deposited with varying concentrations of surface corona charge before annealing for 7 minutes at a temperature of (a) 450 °C or (b) 500 °C.

The results shown for Sr in Figure 59 (a) and (b) are less conclusive than those for Mg and Ca. It is unclear whether Sr is producing charge at the SiO_2-Si interface or whether the interface charge seen in these figures is due to contamination. The ambiguity originates from the fact that the interface charge concentrations do not indicate any clear correlation and do not far exceed that of the controls. Further experiments are required to conclude whether the interface charge seen under certain conditions in Figure 59 is due to Sr or to contamination.

7.2.5 SURFACE CORONA CHARGE DECAY TIME AT ELEVATED TEMPERATURES

For the above spin coating results, the decay of surface corona charge with time at elevated temperature must be considered. This decay will affect the quantity of time for which a field exists and is able to assist ionic migration.

A control sample that was spin coated using only the water-IPA solvent, and no salts, showed that within a one minute anneal at 450 °C the surface corona charge concentration decayed from 6 x 10^{12} q/cm^2 to 0.02 x 10^{12} q/cm^2. Therefore, the driving force for migration no longer exists after 1 minute. During the above experiments, the length of anneal for each ionic species was defined by depositing the highest concentration of surface corona charge and annealing for one-minute increments, measuring the surface charge concentration with KP after each anneal, until the surface corona charge had reduced to be so small that is no longer provided significant assistance to ionic migration.

This control sample provides evidence that there are mechanisms by which the surface corona charge can decay within the time scales used. Therefore, it is possible that the decay in surface corona charge may be affecting the concentration of the ionic species reaching the SiO_2-Si interface. For those species that have a low injection rate (and presumably high energy barrier to injection), part of the corona charge may be decaying during the anneal and therefore unable to assist with ion migration. In order to try and increase the interface charge concentration, it may be advantageous to re-deposit the corona charge during the anneal.

7.3 CONCLUSIONS

In this chapter, steps towards improving the industrial relevance of ionic passivation have been explored. Hydrogenation of the SiO_2-Si interface was found to improve the surface passivation, if carried out before the introduction of ionic species. However, the presence of hydrogen at the interface appeared to interfere with the charge introduction dynamics and may therefore require new characterisation of ion introduction parameters for a hydrogenated interface. If the hydrogenation was conducted after the ionic introduction, the

effective lifetime of the sample was seen to be compromised, something which is under further investigation and could prove a very interesting and useful finding for the scientific understanding of hydrogen dynamics.

Further to this, different ionic species were investigated in an attempt to identify elements that may be more stable at the SiO_2-Si interface than K – and which are able to be injected into the SiO_2 layer and reside at the SiO_2-Si interface as positively charged ions. Rb, Mg, Ca, and Sr were tested. Rb was a success, residing at the SiO_2 interface as a charged species and improving the effective lifetime of a sample to a value comparable to that of a similar K ion passivated sample. The injection rate of Rb was inferred to be lower than that of K, indicating that it may have a larger energy barrier of injection and is therefore likely to be more stable at the SiO_2-Si interface. Of the other ions, these initial experiments indicated that Ca may be injected into the SiO_2 layer under the correct conditions. However, at 450 °C, the injection process is slow, and the experimental parameters adopted may not have been sufficient to allow the injection to reach completion. The injection process being slow is a good indication that the ion may be more stable at the SiO_2-Si interface, which is the target characteristic. It is possible that Mg is injected, but that it does not passivate the SiO_2-Si interface, but instead introduces interface traps. These initial experiments did not provide conclusive evidence that Sr is injected into the SiO_2 layer. It is possible that by testing a wider range of parameters, such as longer anneal times and higher temperatures, or by adding subsequent surface corona charge during the anneal, ion injection of these two ions may be successful. Whether or not these parameters would be suitable for industrial application is likely to be an important question. Therefore, further investigation is needed to draw firm conclusions regarding the injection and subsequent suitability of Mg and Sr as passivating ions. The stability of the ions could be tested by attempting to remove the successful ionic species from the Si-SiO_2 interface using reverse bias TSIC as in Figure 50.

CHAPTER 8
SUMMARY AND FURTHER WORK

The work in this thesis has focused on developing and understanding better the mechanisms present in achieving high quality field-effect passivation using ionic species.

Field-effect passivation (FEP) of solar cells has, for decades, simply been provided by the charge intrinsic to the deposited anti-reflection coating - in most instances, a silicon nitride layer. However, the concentration of charge is defined by the parameters of deposition. These parameters are optimised for anti-reflection properties rather than passivation, meaning that traditionally both the chemical and field-effect passivation have been sub-optimal. In the move towards high efficiency solar cells, the need for improved surface passivation is pressing. This has resulted in high-efficiency cell manufacturers moving towards a double layer system, using a thin layer of silicon dioxide underneath the silicon nitride layer, which provides superior chemical passivation to a single nitride layer. This has opened up the opportunity to de-couple FEP from the nitride deposition and allow the FEP to be optimised for the first time.

In order to introduce FEP into silicon dioxide layers and create a charged dielectric, initially corona charge was tested. Corona charge was found to be extremely effective, but unstable. The addition of a thin hydrophobic layer was found to improve stability. However, it was unclear how the hydrophobic layer would behave once encapsulated, and therefore alternative techniques for FEP were explored. This led to investigating the introduction of ionic species into the SiO_2 layer.

The aims of this thesis, set out in Chapter 1, were:

1. To understand the mechanism behind the success of the alneal process which provides such excellent passivation,
2. To propose an industrially suitable ion introduction technique,
3. Quantify the concentration of potassium ions at the oxide-silicon interface that gives the best carrier lifetime,
4. Investigate ionic species other than sodium and potassium suitable for ionic FEP.

In accord with these aims, the work in this thesis can be split into two broad categories. These are: the work on the alneal, a laboratory-scale technique capable of providing the highest quality silicon dioxide surface passivation recorded, covered in Chapters 4 and 5; and the introduction and optimisation of ionic species for large-scale industrial use, discussed in Chapters 6 and 7. The summary of these findings and areas for further work are reviewed below.

8.1 Alneal Passivation: Standard and Enhanced

For decades, the alneal was considered the most effective surface passivation technique. This thesis has presented a more complete understanding of the alneal process and identified the reasons for it being highly effective. Until this work, alneal passivation was believed to be a solely chemical phenomena, due to hydrogen. However, the effective lifetimes from certain alneal samples were so high that they would have required physically-improbable chemical passivation, indicating that an aspect of FEP is likely to be present.

The presence of FEP in alnealed samples was investigated as part of this work, and the findings presented in Chapter 4 show that, for the instances of the best effective lifetimes, the SiO_2 layers display concentrations of interface charge, providing excellent FEP. There was a significant enhancement to the effective lifetimes of the samples where interface charge was present compared to those without interface charge; this brought about the differentiation between "standard" and ionic-FEP "enhanced" alneal specimens. Where a standard alneal is one where the improvement to the surface is due solely to the hydrogen passivation of the alneal, and an enhanced alneal is where the surface passivation is due to the combination of both chemical passivation and ionic-FEP. Having established that ionic FEP, the focus of this thesis, played a role in achieving world-record-breaking passivation of SiO_2 layers, the cause of the charge was investigated.

The charge was found, using SIMS profiles, to be due to the presence of sodium and potassium ions at the SiO_2-Si interface. It was concluded that the presence of sodium and potassium was due to contamination of the thermal evaporator used for the deposition of the aluminium, since when other thermal evaporators were used no charge was present. The presence of these ions at the interface of samples achieving high effective lifetimes implies that the ions do not introduce affective recombination centres, perhaps because any trap states introduced do not reside within the bandgap.

This work identified the importance of ionic-FEP in improving the effective lifetime of already highly-passivated alneal samples, showing how the effective lifetime could be significantly improved through the marriage of both the hydrogen passivation of the standard alneal and the field effect passivation from the enhanced process. From this knowledge, it was possible to achieve the best-ever passivation of a SiO_2-Si interface recorded, which at certain injection levels exceeded the Richter limit. To develop an industrially appropriate

process, by which this same ionic FEP could be introduced to samples, it was important to consider in detail the mechanism of ion introduction during the enhanced alneal.

8.2 Migration Mechanism of Ions for FEP During the Enhanced Alneal

When investigated, it became apparent that ionic species would only migrate across the SiO_2 layer to the SiO_2-Si interface when there was an electrical connection between the silicon substrate and the aluminium on top of the oxide. This led to the development of the migration model, as described in Chapter 5. The model proposes that when no electrical connection exists, as the cations leave the SiO_2-Al interface, a negative charge builds up on the aluminium layer until migration of the cations across the SiO_2 is prohibited by an opposing electric field. If an electrical connection is present, this negative charge does not build up and the ions are able to migrate to the SiO_2-Si interface where they provided the desired FEP.

The process of migration was found to be significantly faster in the presence of aluminium compared to diffusion without the metal top layer. This was found to be due to the electrical connection between the Al and Si. As explained in Chapter 5, it is proposed that during the alneal due to this electrical connection, ions are able to migrate from the Al-SiO_2 interface far more easily than from an air-SiO_2 or electrically isolated Al-SiO_2 interface because of charge exchange between the Al and Si. This is assisted by the presence of a work function difference between the silicon and aluminium that produced an electric field to encourage the migration of positive ions from the SiO_2 surface to the SiO_2-Si interface. This was verified by using a metal of a different work function.

The next focus was to harness this understanding in order to develop a process compatible with high efficiency industrial devices through the controlled introduction of ions rapidly and in a cost-effective manner.

8.3 Developing an Industrial Ion Migration Process

From investigating the alneal, it was clear that ionic FEP was a vital component in achieving high quality surface passivation. It was then necessary to develop a technique to migrate these ionic species in an industrially-compatible manner, requiring high throughput and low cost.

This work presents commercially viable deposition techniques, spin and spray coating, and characterises field-assisted ionic migration, which is a scalable process. Spin and spray coating were found to be as effective as ionic precursor techniques as thermal evaporation. They provided good uniformity and avoided crystal formation, which is believed to inhibit ion injection into the oxide layer.

When characterising the field-assisted ionic migration, potassium was used, which is more stable at the SiO_2-Si interface than sodium. Corona discharge was used to provide the field, which is industrially favourable as it does not require the deposition or removal of a metal contact in order to apply a field. Using a surface corona charge appropriate for introducing the concentration of interface charge seen during the enhanced alneal, field-assisted ionic migration was seen to occur in under 2 seconds at 450 °C. This finding is promising for industrial application as the time scale is acceptable and the process is low-cost.

The deposition and migration process described resulted in effective lifetimes compatible with high-efficiency devices, however, in order to improve them further, they should be combined with hydrogen passivation.

8.4 Improving Ionic FEP with Hydrogen

With the aim of increasing the surface passivation of samples with ionic FEP, hydrogen was introduced. Shielded Hydrogen Passivation (SHP) was used for this purpose and hydrogenation was tested both before and after ionic FEP was performed.

It was found that when hydrogen was introduced before the ionic FEP, the effective lifetime was improved above that without hydrogen present. Although, the interface charge concentration introduced was lower than expected. Despite the hydrogenation, the effective lifetime was not comparable to those of the enhanced alneal samples. However, the interface charge of the hydrogenated samples was below the concentration seen to provide high effective lifetimes for enhanced alneal samples and ionic field-effect passivated samples. Therefore, should the charge concentration have been optimal, the hydrogenation process may have produced effective lifetimes comparable to that of the enhanced alneal.

If hydrogen was introduced after the ions for FEP were present at the SiO_2-Si interface, the effective lifetime of the sample was seen to decrease significantly. This is an interesting finding which may indicate that the presence of ions facilitates the injection of hydrogen from the SiO_2-Si interface into the Si. Recent work in the literature has suggested that an abundance of hydrogen in the silicon bulk can have a dramatic negative impact on the bulk lifetime. It is possible that the presence of a dipole at the SiO_2-Si interface, due to the presence of ionic charge, may encourage the injection of hydrogen into the silicon.

Most importantly, when hydrogen was introduced before the ionic species, a clear improvement in effective lifetime was noted. The significance of this finding is that the hydrogen does not fully prevent ionic introduction or neutralise ions on reaching the SiO_2-Si interface. This implies that there is no obvious reason that the record-breaking passivation achieved by the enhanced alneal couldn't be achieved using industrial FEP and hydrogenation. Industrially, it may even be possible that the hydrogen is provided by the deposition of a nitride layer on top of the thin oxide layer, creating a double-stack structure that is frequently used in high-efficiency cells. Thin oxide layers were not studied in this work due to difficulties with characterisation.

8.5 Ionic FEP with Different Ions to Improve Stability

The majority of work throughout this thesis was conducted using potassium as the ionic species for FEP. This was because K was found to be more stable than Na at the SiO_2-Si interface, which is vital for commercial solar cells. Identifying ionic species that demonstrate industrial compatibility was one of the aims of this thesis. To do this they need to provide superior stability, high effective lifetimes and be introduced in an appropriate time-scale.

In this thesis, two further ions were found to migrate successfully and reside at the interface as charged species, both with the potential to provide greater stability. These were rubidium and calcium. The results for magnesium and strontium showed that the ionic species were not easily injected under the conditions tested, or, if they did migrate, that the ionic species did not reside at the SiO_2-Si interface as charged species. This does not mean that under more extreme processing conditions the ions would not be injected, and this could be the focus of further investigation.

It was found that the presence of rubidium at the interface provided excellent FEP, comparable to that of potassium. This is extremely promising, as it was concluded that the energy barrier for injection was most likely larger for rubidium than for potassium. The larger energy barrier is concluded from the slower rate of injection. It was beyond the scope of the work to measure the activation energy of injection. This process would not be straight forward as energies for both activation and migration need to be overcome in order for ions to reach the SiO_2-Si interface and would need to be separated. The initial distribution of energy levels would also be required and this is not well defined. Under the assumption that a larger energy barrier for injection is associated with a larger energy well at the SiO_2-Si interface, rubidium may be more strongly bound to the SiO_2-Si interface and thus exhibit better stability than potassium.

Calcium also appeared to migrate across the oxide layer and reside at the SiO_2-Si interface as a charge species. However, the process of migration took significantly longer at 450 °C. This means that to be commercially viable higher temperatures would be necessary, likely in the range of 500 – 600 °C.

8.6 Further Work & Towards Industrialisation

This thesis has shown that the highest quality alneal passivation is only possible with the enhancement of ionic FEP. The thesis presents an industrially appropriate technique for achieving ionic FEP and identified species which may be capable of providing more stable ionic FEP. On the path to achieving industrialisation, the stability of the ions requires further investigation, as outlined below.

It is speculated that, during processing, the ionic deposition will occur after oxide growth, and prior to SiN_x deposition. Once the ions are deposited, and the SiN_x is in place, the drive-in process may occur at a later stage. It is possible that the firing process could be used as the temperature elevation if the corona charge was deposited either before, during the temperature ramp, or at the desired temperature. As the firing profile is flexible, it would be possible to modify the pre-peak plateau to be appropriate for the drive in. However, after the pre-firing peak, the sample will undergo the contact firing peak temperature. This involves a short, ~two second, anneal at 750 °C in order for the silver paste to contact the silicon through the oxide and nitride layers. It is vital that the ionic species remain at the interface during this short, high temperature anneal. Tests must be done on the samples to validate this, which were not possible in the laboratories available due to high risk of contamination. This further emphasises the need for ionic species that are highly stable at the SiO_2-Si interface.

New ionic species that are able to provide FEP were identified in this work, with the hope that they would be more stable at the SiO_2-Si interface. As the next step, it would be useful to perform thermally stimulated ionic conduction experiments under reverse bias in an attempt to drive them off the SiO_2-Si interface, as was done for both sodium and potassium in this thesis. This will give an indication of the ionic stability at the interface and how likely the ions are to remain in position during the fast firing process mentioned above.

For industrial application, the new process must be tested on thin ~7 nm oxide films that are used commercially in stacks. Although only certain characterisation methods will be possible on these samples, it is vital in the transition to an industrial process to know that the suggested methodology is effective of oxide layers the same thickness as those used in industry. The 100 nm SiO_2 layers used throughout this thesis should reflect well the results

that will be seen on a thinner oxide layer. However, a thinner oxide layer is likely to have differing interface properties due to the growth process. It is possible that introducing the ionic species from an SiO_2-SiN_x interface instead of from an SiO_2-air interface may require differing introduction parameters, or, in the worst instance, not be possible. Fortunately, preliminary experiments conducted by another member of the group, have shown introduction of ionic species from an SiO_2-SiN_x interface to be promising.

REFERENCES

[1] Stocker TF, Qin D, Plattner G-K, et al. *IPCC, 2013: Summary for Policymakers. In: Climate Change 2013: The Physical Science Basis. Contribution of Working Group I to the Fifth Assessment Report of the Intergovernmental Panel on Climate Change*. 2013. Epub ahead of print 2013. DOI: 10.1017/CBO9781107415324.004.

[2] International Energy Agengy. *IEA: Key World Energy Statistics 2014*. Epub ahead of print 2014. DOI: www.iea.org.

[3] Helm D. *The Carbon Crunch*. Yale University Press, 2013.

[4] IRENA - International Renewable Energy Agency. *IRENA REmap - A Renewable Energy Roadmap*. 2016.

[5] IRENA - International Renewable Energy Agency. IRENA Renewable Power Generation Costs in 2017. Executive Summary.

[6] Fraunhofer ISE. *Fraunhofer ISE: Photovoltaics Report*. Epub ahead of print 2017. DOI: 26.05.2014.

[7] Global Solar Market Installed 98.9 Gigawatts In 2017 | CleanTechnica, https://cleantechnica.com/2018/03/19/global-solar-market-installed-98-9-gigawatts-in-2017/ (accessed 25 June 2018).

[8] International Renewable Energy Agency (IRENA). *Renewable Capacity Highlights*. 2018.

[9] Global Solar Capacity Set to Surpass Nuclear for the First Time | Greentech Media, https://www.greentechmedia.com/articles/read/global-solar-capacity-set-to-surpass-global-nuclear-capacity#gs.PLvDNqY (accessed 25 June 2018).

[10] Bloomberg New Energy Finance. *Bloomberg: New Energy Outlook*. 2017.

[11] IRENA. *The Power to Change: Solar and Wind Cost Reduction Potential to 2025*. 2016.

[12] Green MA. Commercial progress and challenges for photovoltaics. *Nat Energy* 2016; 1: 1–4.

[13] Green MA, Bremner SP. Energy Conversion Approaches and Materials for High Efficiency Photovoltaics. *Nat Mater* 2017; 16: 23–34.

[14] McEvoy A, Markvart T, Castaner L (eds). *Practical Handbook of Photovoltaics: Fundamentals and Applications*. 2nd Editio. Elsevier Science & Technology, 2011.

[15] PVEducation | Silicon Solar Cell Parameters, http://www.pveducation.org/pvcdrom/design/solar-cell-parameters (accessed 28 March 2018).

[16] PVEducation | Collection Probability, http://pveducation.org/pvcdrom/solar-cell-

operation/collection-probability (accessed 28 March 2018).

[17] Aberle AG. *Crystalline Silicon Solar Cells: Advanced Surface Passivation and Analysis*. Sydney: Centre for Photovoltaic Engineering, University of New South Wales, 1999.

[18] Swanson RM, Beckwith SK, Crane R a., et al. Point-Contact Silicon Solar Cells. *IEEE Trans Electron Devices* 1984; 661–664.

[19] Cotter JE, Guo JH, Cousins PJ, et al. P-type versus n-type silicon wafers: Prospects for high-efficiency commercial silicon solar cells. *IEEE Trans Electron Devices* 2006; 53: 1893–1901.

[20] Aberle AG. Surface passivation of crystalline silicon solar cells: a review. *Prog Photovoltaics Res Appl* 2000; 8: 473–487.

[21] Pukhrem S. Concepts In Photovoltaic Technology. *Solar Love*, http://solarlove.org/concepts-photovoltaic-technology/ (2014, accessed 8 April 2015).

[22] SunPower Sets Solar Cell Efficiency Record at 24.2% - Renewable Energy World, http://www.renewableenergyworld.com/articles/2010/06/sunpower-sets-solar-cell-efficiency-record-at-24-2.html (accessed 10 September 2015).

[23] Green MA. The Passivated Emitter and Rear Cell (PERC): From conception to mass production. *Sol Energy Mater Sol Cells* 2015; 143: 190–197.

[24] Kopfer JM, Keipert-Colberg S, Borchert D. Capacitance-voltage characterization of silicon oxide and silicon nitride coatings as passivation layers for crystalline silicon solar cells and investigation of their stability against x-radiation. *Thin Solid Films* 2011; 519: 6525–6529.

[25] Kho TC, Baker-Finch SC, McIntosh KR. The study of thermal silicon dioxide electrets formed by corona discharge and rapid-thermal annealing. *J Appl Phys*; 109. Epub ahead of print 2011. DOI: 10.1063/1.3559260.

[26] Eades WD, Swanson RM. Calculation of surface generation and recombination velocities at the Si-SiO2 interface. *J Appl Phys* 1985; 58: 4267–4276.

[27] Thermal Silicon Oxide Growth Time Calculator, http://www.cleanroom.byu.edu/OxideTimeCalc.phtml (accessed 7 September 2015).

[28] Sahouane N, Zerga A. Optimization of antireflection multilayer for industrial crystalline silicon solar cells. *Energy Procedia* 2014; 44: 118–125.

[29] Rohatgi A, Doshi P, Moschner J, et al. Comprehensive study of rapid, low-cost silicon surface passivation technologies. *IEEE Trans Electron Devices* 2000; 47: 987–993.

[30] Weber KJ, Jin H. Improved silicon surface passivation achieved by negatively charged silicon nitride films. *Appl Phys Lett* 2009; 94: 1–4.

[31] Dingemans G, Einsele F, Beyer W, et al. Influence of annealing and Al2O3 properties

on the hydrogen-induced passivation of the Si/SiO2 interface. *J Appl Phys* 2012; 111: 93713.

[32] Dingemans G, Kessels WMM. Status and prospects of Al2O3-based surface passivation schemes for silicon solar cells. *J Vac Sci Technol A* 2012; 30: 1–27.

[33] Dingemans G, Beyer W, van de Sanden MCM, et al. Hydrogen induced passivation of Si interfaces by Al2O3 films and SiO2/Al2O3 stacks. *Appl Phys Lett* 2010; 97: 152106.

[34] Bordihn S, Kiesow I, Mertens V, et al. Impact of the Deposition and Annealing Temperature on the Silicon Surface Passivation of ALD Al2O3 Films. *Energy Procedia* 2012; 27: 396–401.

[35] Suh D, Liang W, Weber K. The study of Al2O3 Passivation by corona charge. *27th Eur Photovolt Sol Energy Conf Exhib* 2012; 896–899.

[36] Schmidt M, Lemme MC, Kurz H, et al. Impact of H2/N2 annealing on interface defect densities in Si(100)/SiO2/HfO2/TiN gate stacks. *Microelectron Eng* 2005; 80: 70–73.

[37] Reed ML, Plummer JD. Chemistry of Si-SiO2 interface trap annealing. *J Appl Phys* 1988; 63: 5776–5793.

[38] Sopori B, Deng X, Benner J, et al. Hydrogen in silicon: A discussion of diffusion and passivation mechanisms. *Sol Energy Mater Sol Cells* 1996; 41–42: 159–169.

[39] Bourret-Sicotte G, Hamer P, Bonilla RS, et al. Shielded hydrogen passivation – a novel method for introducing hydrogen into silicon. *Energy Procedia* 2017; 124: 267–274.

[40] Bourret-Sicotte G, Hamer P, Bonilla RS, et al. Shielded hydrogen passivation − A potential in-line passivation process. *Phys Status Solidi Appl Mater Sci*; 214. Epub ahead of print 2017. DOI: 10.1002/pssa.201700383.

[41] Mandelkorn J, Lamneck JH. Simplified fabrication of back surface electric field silicon cells and novel characteristics of such cells. 1972; 29: 121–130.

[42] Sze SM, Ng KK. *Physics of Semiconductor Devices*. Hoboken, New Jersey: Wiley, 2007.

[43] Xiao S, Xu S. High-Efficiency Silicon Solar Cells—Materials and Devices Physics. *Crit Rev Solid State Mater Sci* 2014; 39: 277–317.

[44] Iftiquar SM, Lee Y, Ju M, et al. Fabrication of Crystalline Silicon Solar Cell with Emitter Diffusion , SiNx Surface Passivation and Screen Printing of Electrode.

[45] Granek F, Reichel C, Hermle M, et al. Front Surface Passivation of n-type High Efficiency Back-junction Silicon Solar Cells Using Front Surface Field. In: *Presented at the 22nd European Photovoltaic Solar Energy Conference and Exhibition*. Milan, 2007, pp. 3–6.

[46] Aberle AG, Glunz S, Warta W. Impact of illumination level and oxide parameters on Shockley-Read-Hall recombination at the Si-SiO2 interface. *J Appl Phys* 1992; 71: 4422–4431.

[47] Dauwe S, Schmidt J, Metz a., et al. Fixed charge density in silicon nitride films on crystalline silicon surfaces under illumination. *Conf Rec Twenty-Ninth IEEE Photovolt Spec Conf* 2002; 162–165.

[48] Schmidt J, Werner F, Veith B, et al. Advances in the Surface Passivation of Silicon Solar Cells. *Energy Procedia* 2012; 15: 30–39.

[49] Hoex B, Gielis JJH, Van De Sanden MCM, et al. On the c-Si surface passivation mechanism by the negative-charge-dielectric Al2 O3. *J Appl Phys*; 104. Epub ahead of print 2008. DOI: 10.1063/1.3021091.

[50] Glunz SW, Sproul AB, Warta W, et al. Injection - level - dependent recombination velocities at the Si - SiO2 interface for various dopant concentrations Injection-fievel-dependent recombination for various dopant concentrations velocities at the Si-SQ interface. 1611. Epub ahead of print 2016. DOI: 10.1063/1.356399.

[51] Richter A, Glunz SW, Werner F, et al. Improved quantitative description of Auger recombination in crystalline silicon. *Phys Rev B - Condens Matter Mater Phys* 2012; 86: 1–14.

[52] Bonilla RS, Woodcock F, Wilshaw PR. Very low surface recombination velocity in n-type c-Si using extrinsic field effect passivation. *J Appl Phys* 2014; 116: 054102.

[53] Werner F, Veith B, Tiba V, et al. Very low surface recombination velocities on p- and n-type c-Si by ultrafast spatial atomic layer deposition of aluminum oxide. *Appl Phys Lett* 2010; 97: 162103.

[54] Goldman M, Goldman a., Sigmond RS. The corona discharge, its properties and specific uses. *Pure Appl Chem* 1985; 57: 1353–1362.

[55] Schroder DK, Fung MS, Verkuil RL, et al. Corona-oxide-semiconductor device characterization. *Solid State Electron* 1998; 42: 505–512.

[56] Bonilla RS, Reichel C, Hermle M, et al. Long term stability of c-Si surface passivation using corona charged SiO2. *Appl Surf Sci* 2017; 412: 657–667.

[57] Bonilla RS, Wilshaw PR. Stable Field Effect Surface Passivation of n-type Cz Silicon. *Energy Procedia* 2013; 38: 816–822.

[58] Huamao L, Zhongfu X, Shaoqun S, et al. The Charge Dynamics of Thermally Wet Grown SiO2 Electret by Corona Charging Method with Constant Grid Current. In: *9th International Symposium on Electrets, 1996.* 1996, pp. 133–138.

[59] Amjadi H. Investigations on charge storage and transport in plasma-deposited inorganic electrets. *IEEE Trans Dielectr Electr Insul* 1999; 6: 236–241.

[60] Bonilla RS, Reichel C, Hermle M, et al. Electric Field Effect Surface Passivation for Silicon Solar Cells. *Solid State Phenom* 2013; 205–206: 346–351.

[61] Bonilla RS, Wilshaw PR. A technique for field effect surface passivation for silicon solar cells. *Appl Phys Lett*; 104. Epub ahead of print 2014. DOI: 10.1063/1.4882161.

[62] Bonilla RS, Wilshaw PR. Potassium ions in SiO2: Electrets for silicon surface passivation. *J Phys D Appl Phys*; 51. Epub ahead of print 2018. DOI: 10.1088/1361-6463/aa9b1b.

[63] Eades WD. *PhD Thesis*. Stanford University, 1985.

[64] Kerr MJ, Cuevas A. Very low bulk and surface recombination in oxidized silicon wafers. *Semicond Sci Technol* 2002; 17: 35–38.

[65] Zhao J, Wang A, Altermatt PP, et al. 24% Efficient Silicon Solar Cells. In: *IEEE First World Conference on Photovoltaic Energy Conversion*. 1994, pp. 1477–1480.

[66] Bonilla RS, Hoex B, Hamer P, et al. Dielectric surface passivation for silicon solar cells: A review. *Phys Status Solidi (a)*; 214.

[67] Bonilla RS, Reichel C, Hermle M, et al. Extremely low surface recombination in 1 Ω cm n-type monocrystalline silicon. *Phys status solidi - Rapid Res Lett* 2016; 1: 1–5.

[68] Rein S. *Lifetime Spectroscopy: A Method of Defect Characterization in Silicon for Photovoltaic Applications*. Berlin: Springer, 2005.

[69] Chelikowsky JR, Cohen ML. Electronic structure of silicon. *Phys Rev B* 1974; 10: 5095–5107.

[70] Nelson J. *The Physics of Solar Cells*. London: Imperial College Press, 2004.

[71] Sze SM. *Semiconductor Devices Physics and Technology*. 2nd ed. Wiley, 2002.

[72] Altermatt PP, Geelhaar F, Trupke T, et al. Injection dependence of spontaneous radiative recombination in crystalline silicon: Experimental verification and theoretical analysis. *Appl Phys Lett*; 88. Epub ahead of print 2006. DOI: 10.1063/1.2218041.

[73] Gerlach W, Schlangenotto H, Maeder H. On the radiative recombination rate in silicon. *Phys Status Solidi* 1972; 13: 277–283.

[74] Altermatt PP, Geelhaar F, Trupke T, et al. Injection dependence of spontaneous radiative recombination in c-Si: Experiment, theoretical analysis, and simulation. *NUSOD '05 - Proc 5th Int Conf Numer Simul Optoelectron Devices* 2005; 2005: 47–48.

[75] Huldt L. Band-to-band auger recombination in indirect gap semiconductors. *Phys Status Solidi* 1971; 8: 173–187.

[76] Sinton RA, Swanson RM. Recombination in highly injected silicon. *IEEE Trans Electron Devices* 1987; 34: 1380–1389.

[77] Yablonovitch E, Gmitter T. Auger recombination in silicon at low carrier densities. *Appl Phys Lett* 1986; 49: 587–589.

[78] Hangleiter A, Hacker R. Enhancement of Band-to-Band Auger Recombination by Electron-Hole Correlations. *Phys Rev Lett* 1990; 65: 215–218.

[79] Kerr MJ, Cuevas A. General parameterization of Auger recombination in crystalline silicon. *J Appl Phys* 2002; 91: 2473–2480.

[80] Shockley W, Read WT. Statistics of the Recombination of Holes and Electrons. *Phys Rev* 1952; 87: 835–842.

[81] Hall RN. Electron-hole recombination in Geranium. *Phys Rev* 1968; 175: 823–840.

[82] Grant NE, Rougieux FE, MacDonald D, et al. Grown-in defects limiting the bulk lifetime of p -type float-zone silicon wafers. *J Appl Phys*; 117. Epub ahead of print 2015. DOI: 10.1063/1.4907804.

[83] Grant NE, Rougieux FE, MacDonald D. Low Temperature Activation of Grown-In Defects Limiting the Lifetime of High Purity n-Type Float-Zone Silicon Wafers. *Solic State Phenom* 2016; 242: 120–125.

[84] Grant NE, Markevich VP, Mullins J, et al. Permanent annihilation of thermally activated defects which limit the lifetime of float-zone silicon. *Phys Status Solidi Appl Mater Sci* 2016; 213: 2844–2849.

[85] Grant NE, Markevich VP, Mullins J, et al. Thermal activation and deactivation of grown-in defects limiting the lifetime of float-zone silicon. *Phys Status Solidi - Rapid Res Lett* 2016; 10: 443–447.

[86] McIntosh KR, Black LE. On effective surface recombination parameters. *J Appl Phys*; 116. Epub ahead of print 2014. DOI: 10.1063/1.4886595.

[87] Neamen D. *Semiconductor Physics and Devices*. McGraw-Hil. University of New Mexico, 2012.

[88] Girisch RBM, Mertens RP, De Keersmaecker RF. Determination of Si-SiO2 Interface Recombination Parameters Using a Gate-Controlled Point-Junction Diode Under Illumination. *IEEE Trans Electron Devices* 1988; 35: 203–222.

[89] Luke KL, Cheng LJ. Analysis of the interaction of a laser pulse with a silicon wafer: Determination of bulk lifetime and surface recombination velocity. *J Appl Phys* 1987; 61: 2282–2293.

[90] Kimmerle A, Greulich J, Wolf A. Carrier-diffusion corrected J0-analysis of charge carrier lifetime measurements for increased consistency. *Sol Energy Mater Sol Cells* 2015; 142: 116–122.

[91] Klaassen DBM. A unified mobility model for device simulation-II. Temperature dependence of carrier mobility and lifetime. *Solid State Electron* 1992; 35: 961–967.

[92] PV Lighthouse, https://www.pvlighthouse.com.au/.

[93] Sproul AB. Dimensionless solution of the equation describing the effect of surface recombination on carrier decay in semiconductors. *J Appl Phys* 1994; 76: 2851–2854.

[94] Mäckel H, Varner K. On the determination of the emitter saturation current density from lifetime measurements of silicon devices. *Prog Photovolt Res Appl* 2013; 21: 850–866.

[95] Pässler R. Dispersion-related descriptoon of temperature dependancies of band gaps in semiconductors. *Phys Rev B* 2002; 66: 1–18.

[96] Altermatt P. Private Communications.

[97] Bonilla RS, Wilshaw PR. On the c-Si/SiO2interface recombination parameters from photo-conductance decay measurements. *J Appl Phys*; 121. Epub ahead of print 2017. DOI: 10.1063/1.4979722.

[98] Bonilla RS. *DPhil thesis: Surface passivation for silicon solar cells*. University of Oxford, 2015.

[99] Film Sense Elipsometer Applications, http://www.film-sense.com/applications/.

[100] Kerr MJ, Cuevas A. Recombination at the interface between silicon and stoichiometric plasma silicon nitride. *Semicond Sci Technol* 2002; 17: 166–172.

[101] Baker-finch SC, Mcintosh KR. Characterisation of corona-charged oxide-passivated silicon.

[102] Glunz SW, Biro D, Rein S, et al. Field-effect passivation of the SiO2-Si interface. *J Appl Phys* 1999; 86: 683.

[103] Schroder DK. Contactless surface charge semiconductor characterization. *Mater Sci Eng B Solid-State Mater Adv Technol* 2002; 91–92: 196–210.

[104] Woodcock F. *Part II Thesis: Passivation of Semiconductor Surfaces for High-Efficiency Solar Cells*. University of Oxford, 2014.

[105] Bonilla RS, Collett K, Rands L, et al. Stable, Extrinsic, Field Effect Passivation for Back Contact Silicon Solar Cells. *Solid State Phenom* 2015; 242: 67–72.

[106] Eldridge JM, Kerr DR. Sodium Ion Drift through Phosphosilicate Glass-SiO2 Films. *J Electrochem Soc* 1971; 118: 986.

[107] Du S. *Part II Thesis: Ionic Field Effect Surface Passivation of Silicon Solar Celss*. University of Oxford, 2018.

[108] Collett KA, Bonilla RS, Hamer P, et al. An enhanced alneal process to produce SRV under 1 cm/s in 1 Ω cm n-type Si. *Sol Energy Mater Sol Cells*; 173. Epub ahead of print 2017. DOI: 10.1016/j.solmat.2017.06.022.

[109] Liu S. *Part II thesis: An investigation of the effect of charge at the silicon/silicon dioxide interface*. University of Oxford, 2017.

[110] Blum AL, Swirhun JS, Sinton RA, et al. Inter - laboratory Study of Eddy - Current Measurement of Excess - Carrier Recombination Lifetime.

[111] Nicollian EH, Brews JR. *Metal Oxide Semiconductor — Physics and Technology*. New York: Wiley, 1982.

[112] Schroder DK. *Semiconductor material and device characterisation*. John Wiley & Sons, Inc., 2006.

[113] Rands L. *Masters Thesis: Passivation of silicon surfaces through the introduction of charge into insulating layers*. University of Oxford, 2015.

[114] Baikie ID, Mackenzie S, Estrup PJZ, et al. Noise and the Kelvin method. *Rev Sci Instrum* 1991; 62: 1326–1332.

[115] Mönch W. *Semiconductor Surfaces and Interfaces*. 3rd Editio. Springer, 2001.

[116] Grove AS, Fitzgerald DJ. Characteristics of surface space-charge regions under non-equilibrium conditions. *IEEE Trans Electron Devices* 1966; 13: 783–806.

[117] Terman LM. An investigation of surface states at a silicon/silicon oxide interface employing metal-oxide-silicon diodes. *Solid State Electron* 1962; 5: 285–299.

[118] Nicollian EH, Goetzberger A. The Si-Si02 Interface -Electrical Properties as Determined by the Metal-Insulator- Silicon Conductance Technique. *Bell Syst Tech J* 1967; XLVI: 1055.

[119] Nicollian EH, Goetzberger A. MOS conductance technique for measuring surface state parameters. *Appl Phys Lett* 1965; 7: 216–219.

[120] DeClerck G. Characterisation of Surface States at the Si-SiO2 Interface. In: *Nondestructive Evaluation of Semiconductor Materials and Devices*. 1979, pp. 105–148.

[121] Zaininger KH, Warfield G. Limitations of the MOS Capacitance Method for the Determination of Semiconductor Surface Properties. *IEEE Trans Electron Devices* 1965; ED-12: 179–193.

[122] Schmidt J, Merkle A, Brendel R, et al. Surface Passivation of High-efficiency Silicon Solar Cells by Atomic-layer-deposited Al2O3. *Prog Photovoltaics Res Appl* 2008; 16: 461–466.

[123] Zhao J. Recent advances of high-efficiency single crystalline silicon solar cells in processing technologies and substrate materials. *Sol Energy Mater Sol Cells* 2004; 82: 53–64.

[124] Benick J, Hoex B, Dingemans G, et al. High-efficiency n-type silicon solar cells with front boron emitter. In: *24th European Photovoltaic Solar Energy Conference*. Hamburg, Germany, 2009, pp. 863–870.

[125] Kho TC, Baker-Finch SC, McIntosh KR. The study of thermal silicon dioxide electrets formed by corona discharge and rapid-thermal annealing. *J Appl Phys*; 109. Epub ahead of print 2011. DOI: 10.1063/1.3559260.

[126] Thomson AF, McIntosh KR. Light-enhanced surface passivation of TiO2-coated

silicon. *Prog Photovolt Res Appl* 2012; 20: 343–349.

[127] Lobo R. *Part II Thesis: The Effect of Aluminium on the Passivation of Silicon Surfaces using Dielectrics*. University of Oxford, 2015.

[128] Grant NE, Murphy JD. Temporary Surface Passivation for Characterisation of Bulk Defects in Silicon: A Review. *Phys Status Solidi - Rapid Res Lett*; 1700243. Epub ahead of print 2017. DOI: 10.1002/pssr.201700243.

[129] Deal BE. Measurement and Control of Dielectric Film Properties During Semiconductor Device Processing. In: *Silicon Device Processing, Proceedings, Volume 13*. 1970, pp. 36–50.

[130] Kerr MJ. *PhD: Surface, Emitter and Bulk Recombination in Silicon and Development of Silicon Nitride Passivated Solar Cells*. The Australian National University, http://ssc.cecs.anu.edu.au/files/mark_kerr_thesis.pdf (2002).

[131] Cuevas A, Basore PA, Giroult-Matlakowski G, et al. Surface recombination velocity of highly doped n-type silicon. *J Appl Phys* 1996; 80: 3370–3375.

[132] Larionova Y, Mertens V, Harder N-P, et al. Surface passivation of n-type Czochralski silicon substrates by thermal-SiO2/plasma-enhanced chemical vapor deposition SiN stacks. *Appl Phys Lett* 2010; 96: 032105.

[133] Zhao J, Wang A, Altermatt PP, et al. High efficiency PERT cells on n-type silicon substrates. *29th IEEE Photovolt Spec Conf* 2002; 218–221.

[134] Reed ML, Plummer JD. Si-SiO2 interface trap production by low-temperature thermal processing. *Appl Phys Lett* 1987; 51: 514.

[135] Deal BE, MacKenna EL, Castro PL. Characteristics of Fast Surface States Associated with SiO2-Si and Si3N4-SiO2-Si Structures. *J Electrochem Soc* 1969; 116: 997.

[136] Reed M. Models of Si-SiO2 interface reactions. *Semicond Sci Technol* 1989; 4: 980.

[137] Balk P. Effects of hydrogen annealing on silicon surfaces. In: *Proceedings of the Electrochemical Society Fall Meeting*. Buffalo, 1965, p. 29.

[138] Richards BS. Comparison of TiO2 and other dielectric coatings for buried-contact solar cells: A review. *Prog Photovoltaics Res Appl* 2004; 12: 253–281.

[139] Castro PL, Deal BE. Low-temperature reduction of fast surface states associated with thermally oxidized silicon. *J Electrochem Soc* 1971; 118: 280.

[140] Fishbein BJ, Watt JT, Plummer JD. Time Resolved Annealing of Interface Traps in Polysilicon Gate Metal-Oxide-Silicon Capacitors. *J Electrochem Soc Solid-State Sci Technol* 1987; 134: 674–681.

[141] Yeow YT, Lamb DR, Brotherton SD. An investigation of the influence of low-temperature annealing treatments on the interface state density at the Si-Si02 interface. *J Phys D Appl Phys*; 8.

[142] Kooi E. Influence of Heat Treatments and Ionizing Irradiations on the Charge Distribution and the Number of Surface States in the Si-Si02 System. *IEEE Trans Electron Devices* 1966; 13: 238–245.

[143] Beckmann KH. Hydrides and Hydroxyls in Thin Silicon Dioxide Films. 1–6.

[144] Swaroop B. Hydrogen annealing effect on silicon-insulator(s) interface states. *J Phys D Appl Phys* 1973; 6: 1090–1092.

[145] Afanas'ev V V., de Nijs JMM, Balk P, et al. Degradation of the thermal oxide of the Si/SiO2/Al system due to vacuum ultraviolet irradiation. *J Appl Phys* 1995; 78: 6481–6490.

[146] Hallam B, Sugianto A, Mai L, et al. Hydrogen Passivation of Laser-Induced Defects for Silicon Solar Cells. 2476–2480.

[147] Zhao J, Wang A, Green MA. 23.5% Eficient Silicon Solar Cell. *Prog Photovoltaics Res Appl* 1994; 2: 227–230.

[148] Bonilla RS, Martins G, Wilshaw PR. Investigation of Parasitic Edge Recombination in High-Lifetime Oxidized n-Si. *Solid State Phenom* 2015; 242: 73–79.

[149] Veith-Wolf BA, Schäfer S, Brendel R, et al. Reassessment of intrinsic lifetime limit in n-type crystalline silicon and implication on maximum solar cell efficiency. *Sol Energy Mater Sol Cells* 2018; 186: 194–199.

[150] Hickmott TW. Thermally stimulated ionic conductivity of sodium in thermal SiO 2. *J Appl Phys* 1975; 46: 2583–2598.

[151] Nauta PK, Hillen MW. Investigation of mobile ions in MOS structures using the TSIC method. *J Appl Phys* 1978; 49: 2862–2865.

[152] Boudry MR, Stagg JP. The kinetic behavior of mobile ions in the Al-SiO2-Si system. *J Appl Phys* 1979; 50: 942–950.

[153] Snow EH, Grove AS, Deal BE, et al. Ion transport phenomena in insulating films. *J Appl Phys* 1965; 36: 1664–1673.

[154] Hofstein SR. An investigation of instability and charge motion in metal-silicon oxide-silicon structures. *IEEE Trans Electron Devices* 1966; 13: 222–237.

[155] Hickmott TW. Dipole layers at the metal-SiO2 interface. *J Appl Phys* 1980; 51: 4269–4281.

[156] Stagg JP. Drift mobilities of Na+ and K+ ions in SiO2 films. *Appl Phys Lett* 1977; 31: 532.

[157] Kerr DR. A Review of Instability Mechanisms in Passivation Films. In: *8th Reliability Physics Symposium*. IEEE, 1970, pp. 1–8.

[158] Hofstein SR. Proton and sodium transport in SiO2 films. *IEEE Trans Electron Devices* 1967; 14: 749–759.

[159] Deal BE, Snow EH, Mead CA. Barrier energies in metal-silicon dioxide-silicon structures. *J Phys Chem Solids* 1966; 27: 1873–1879.

[160] Choquet C, Balland B. New accurate exploitation of thermally stimulated ionic current curves for alkali contaminated metal-oxide-silicon structures. *Appl Phys Lett* 1988; 52: 1791.

[161] Eastment RM, Mee CHB. Work function measurements on (100), (110) and (111) surfaces of aluminium. *J Phys F Met Phys* 1973; 3: 1738–1745.

[162] Rivière JC. The work function of gold. *Appl Phys Lett* 1966; 8: 172.

[163] Yamin M. Charge Storage Effects in Silicon Dioxide Films. *IEEE Trans Electron Devices* 1965; 88–96.

[164] Chang JS, Lawless PA, Yamamoto T. Corona Discharge Processes. *IEEE Trans Plasma Sci* 1991; 19: 1152–1166.

[165] Chan C, Fung TH, Abbott M, et al. Modulation of Carrier-Induced Defect Kinetics in Multi-Crystalline Silicon PERC Cells Through Dark Annealing. *Sol RRL* 2017; 1: 1600028.

[166] Ciesla A. *PhD Thesis: Advanced laser processing for next-generation silicon wafer solar cells*. UNSW, 2017.

[167] Wenham S. Hydrogen Induced Recombination. In: *Presented at UNSW Hydrogen Workshop*. 2016.

[168] Solubility table - Wikipedia, https://en.wikipedia.org/wiki/Solubility_table#P (accessed 26 June 2018).

APPENDIX

OXIDE SURFACE

Firstly, the oxide surface was investigated. If contamination was present on the oxide surface, cleaning the surface should remove this.

RCA CLEAN OF OXIDE SURFACE

The oxide surface was cleaned with the industry standard clean RCA 1 and RCA 2. These remove metals and organics from the surface. Everything else in the process remained the same. The samples were deposited with 99.999 % Al in the thermal evaporator, alnealed in the tube furnace under an argon atmosphere, for 60 minutes instead of 30 minutes, and the aluminium was removed using warm aluminium etchant. The effective lifetimes after alneal for both the RCA cleaned and the as-received samples are shown in Figure 60.

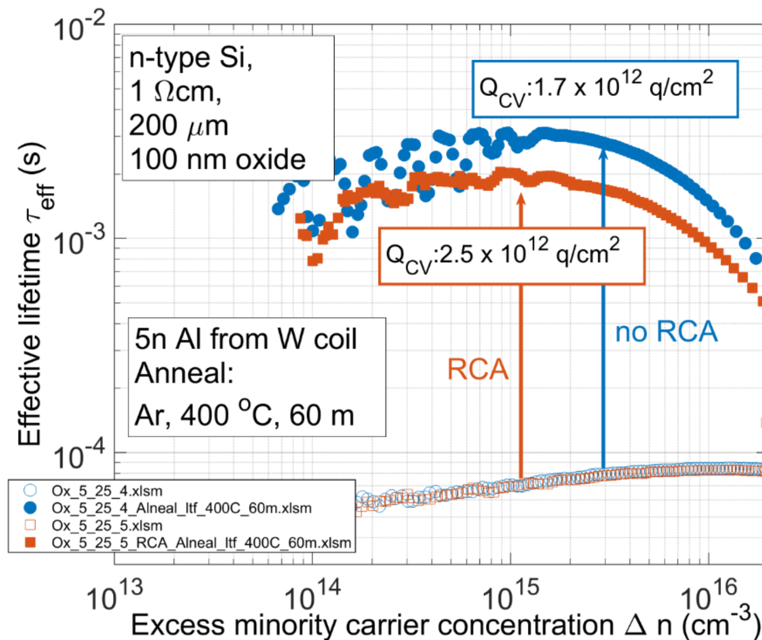

Figure 60 Injection dependent effective lifetimes for alnealed samples with and without RCA oxide surface clean before aluminium deposition.

From Figure 60 it is evident that the RCA clean did not remove the source of ionic contamination. The effective lifetime increased for both the alneal of the as-received oxide sample and the RCA cleaned oxide sample. The interface charge concentrations from CV measurements are included in Figure 60. The RCA cleaned sample presents a greater concentration of interface charge than the as-oxidised sample. This could either be due to a variation in the contamination during processing, or it could indicate that further contamination is introduced during the RCA cleaning process, meaning that the experiment was not conclusive.

In order to assess the surface in an alternative manner, e-beam evaporation of aluminium was tested.

E-BEAM EVAPORATION OF ALUMINIUM

An as-received oxide sample was prepared for TSIC treatment in the e-beam evaporator. Both the front and back metal contacts were deposited in the e-beam chamber to avoid exposure to the thermal evaporator. The TSIC data is shown in Figure 61.

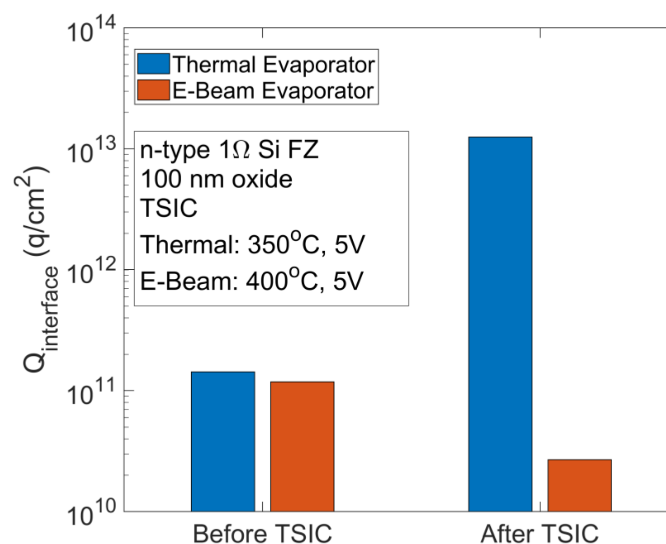

Figure 61 Interface charge before and after TSIC processing for e-beam and thermally evaporated aluminium front and back contact. Log y-axis.

The e-beam interface charge appears to decrease slightly during processing, this is due to interface traps that distort the CV curve before TSIC, which anneal out during processing. Negligible interface charge is seen for the e-beam evaporated aluminium, whereas for the thermally evaporated aluminium, there is a significant interface charge seen after TSIC processing. If there had been contamination present on the oxide surface, this would have been visible after TSIC processing regardless of aluminium deposition technique. Thus, it is possible to conclude that the oxide surface is not the source of contamination.

FURNACE

Thermally evaporated samples processed using TSIC were not exposed to the tube furnace because they were heated on a hot plate in air. However, these samples still presented ionic contamination. Therefore, it was highly unlikely that the tube furnace would be the source of the contamination. However, to test this, an as-oxidised sample, with no aluminium present, was annealed in the tube furnace for 60 minutes at 400 °C. Work by Bonilla et al [61] demonstrated that Na and K purposefully deposited on the oxide surface diffuse into the oxide after 30 minutes. The effective lifetime curves before and after the anneal are shown in Figure 62. The interface charge calculated from a CV measurement after the anneal is included.

Figure 62 shows that the effective lifetime does not increase, and the charge concentration measured is negligible. This suggests that the tube furnace is not the source of contamination.

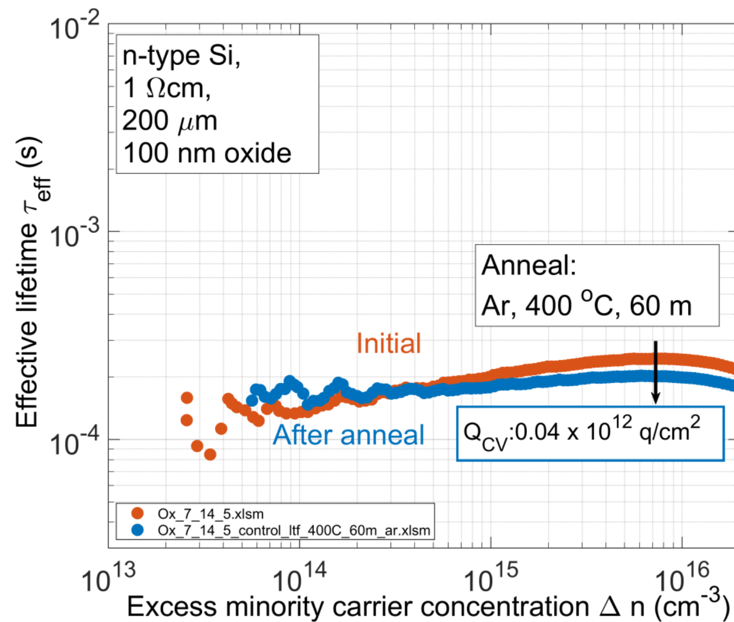

Figure 62 Injection dependent effective lifetime curves before and after anneal in tube furnace for one hour at 400 °C with no aluminium present.

THERMAL EVAPORATOR

The thermal evaporator had been used frequently by the research group to evaporate Na and K salts. It is thus unsurprising that the evaporator would be the source of contamination. There are several aspects of thermal evaporation that could introduce the salts. Firstly, the vacuum at which the aluminium is deposited may influence the concentration of ions in the chamber, there is also the potential for reflux from the diffusion pump. Secondly, the tungsten coil from which the aluminium is evaporated may contain a concentration of Na and K. Thirdly, the aluminium itself. Finally, the surfaces of the evaporation chamber.

HIGH VACUUM VS LOW VACUUM

As-received oxidised samples were deposited with 99.999% aluminium at two vacuum pressures. One under a higher vacuum of ~1 x10^{-6} kPa and the second under a lower vacuum of ~4 x 10^{-6} kPa. Samples were to be characterised only by interface charge and therefore samples of < 1 cm^2 were used. These were fully covered with aluminium on one oxide

surface. They were annealed on a hot plate at 400 °C. Aluminium was etched in ~ 50 °C commercial etchant. The back oxide was removed using HF and the samples back contacted with InGa and silver dag to fabricate a MOS structure suitable for Hg-CV measurements. Interface charge concentrations are shown in Figure 63.

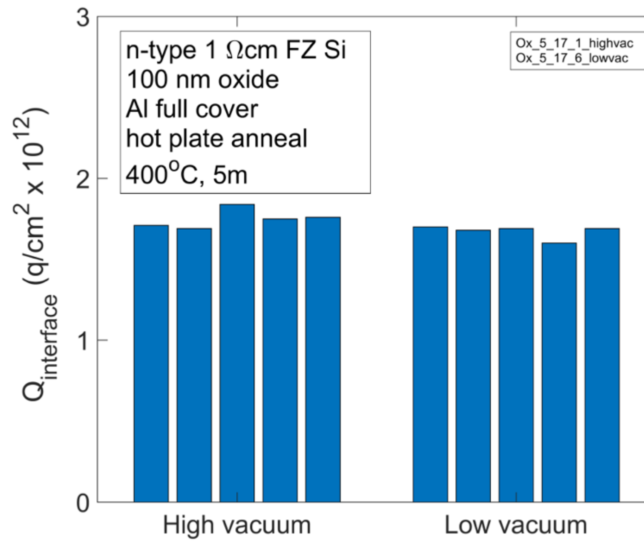

Figure 63 Interface charge concentrations of alnealed samples with aluminium thermally evaporated under different vacuum pressures.

The concentration of charge at the interface after an alneal was unaffected by the vacuum pressure at which the aluminium was evaporated. There was significant contamination present for both deposition regimes, therefore the vacuum cannot be considered a means to eliminate contamination.

BARE TUNGSTEN COIL

To test whether the tungsten coil was the contamination source, a bare coil, with no aluminium, was heated under vacuum in the line of sight of a sample. The coil was exposed to the same current and time profile as it would have been had there been aluminium present to evaporate. The sample was then deposited with a thermally evaporated gold contact from a tungsten boat, to avoid the deposition of aluminium. The back oxide was removed using

HF and an aluminium back contact thermally evaporated. The MOS structure underwent TSIC and after processing the interface charge was measured using the Au dot and probe station CV as in Figure 64.

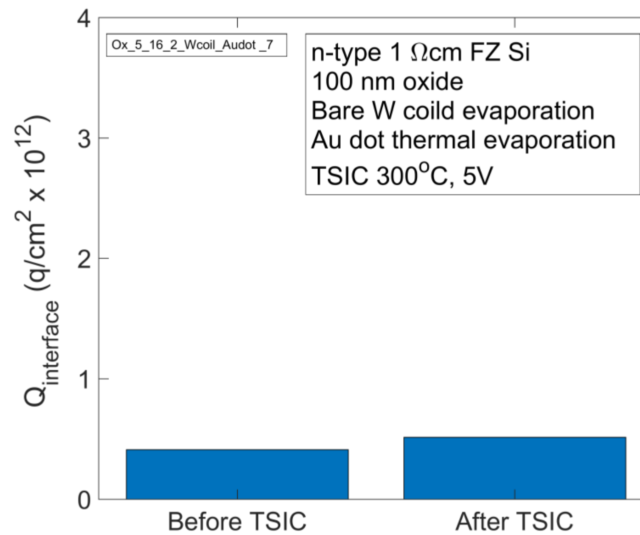

Figure 64 Interface charge from CV data before and after TSIC processing for sample exposed to bare tungsten coil under high current with no Al. Thermally evaporated Au for front contact.

The interface charge concentration after processing is negligible, indicating the tungsten coil was not responsible for the contamination. However, this test was not ideal. During thermal evaporation, as the aluminium melts it etches into the tungsten and wets the surface. It is possible that this mechanism is key to releasing any contamination within the tungsten coil and this aspect of processing is inevitably lacking during the bare tungsten coil test. Attempts were made to evaporate aluminium from an aluminium oxide crucible and avoid the use of a tungsten coil. Unfortunately, this proved to be challenging as the maximum current of the thermal evaporator equipment was unable to heat the aluminium within the crucible to the point of evaporation.

HIGH PURITY AL

As the aluminium itself could have been the source of contamination, high purity aluminium of 99.9999% (6n) was trialled. The aluminium was wrapped around the tungsten coil and evaporated as usual. Samples were cleaved to be < 1cm^2 and one oxide surface was covered in thermally evaporated 6n Al. These were then annealed on a hot plate at 400 °C before the back oxide was removed and an ohmic contact to the silicon fabricated for Hg-CV measurements. The interface charge concentrations after alnealing are shown in Figure 65.

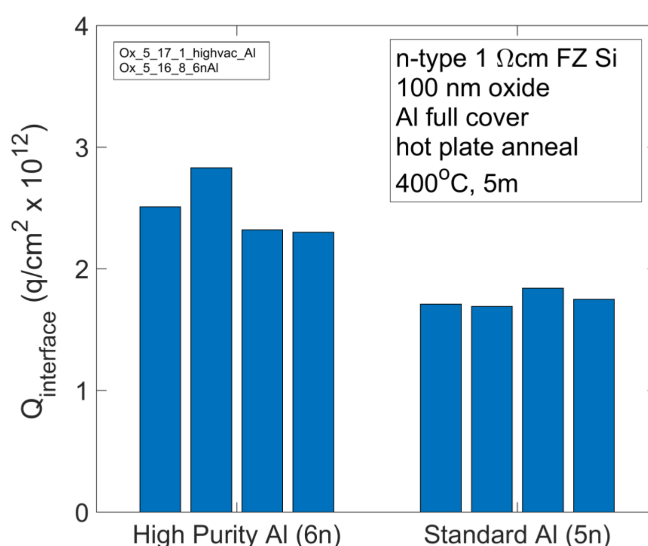

Figure 65 Interface charge concentration after alnealing using 5n Al and 6n Al both thermally evaporated from a tungsten coil.

The high purity, 6n, aluminium appears to introduce a greater concentration of interface charge than the lower purity, 5n, aluminium, indicating that the aluminium itself is not the source of the contamination.

CLEAN THERMAL EVAPORATOR COMPONENTS

Having assessed the sample surface, the furnace, vacuum pressure during evaporation, aluminium purity and having found that when the aluminium is e-beam evaporated there is

no contamination, the most likely source of contamination was either the tungsten coil, or the evaporation chamber itself.

In an attempt to clean the components of the thermal evaporator, new copper arms for the electrode and a new sample holder was made and the removable panels of the thermal evaporator were chemically cleaned. These were soaked in weak NaOH, rinsed in DI water followed by dilute HCl and then DI water again. The HCl rinse was to react with any remaining NaOH and avoid further contamination of the chamber with Na. Unfortunately, the contamination remained, as shown in Figure 66.

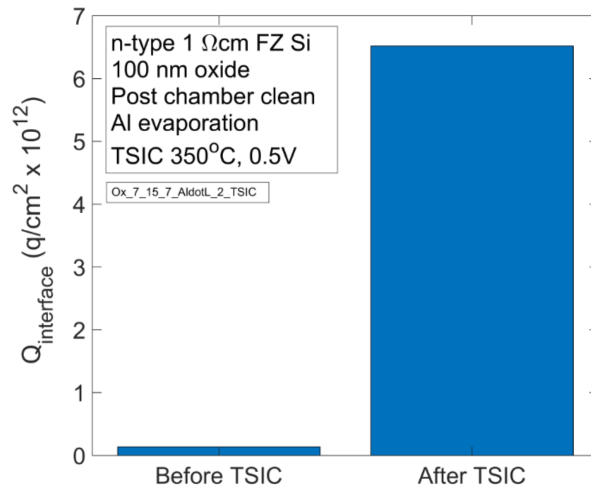

Figure 66 Interface charge concentration after TSIC processing of 5n Al thermally evaporated from a tungsten coil using new copper arms, cleaned chamber walls and new pyrex sample holder.